Modeling and Optimal Control of Magnetic Micro-Swimmers

Yacine El Alaoui-Faris

UNIVERSITÉ CÔTE D'AZUR

ÉCOLE DOCTORALE
SCIENCES FONDAMENTALES ET APPLIQUÉES

— Version de soutenance —

PROVISOIRE

Modélisation et Contrôle Optimal de Micro-Nageurs Magnétiques

présentée et soutenue publiquement par

Yacine El Alaoui-Faris

En vue d'obtenir le grade de

Docteur en Sciences

de l'Université Côte d'Azur

Discipline : Mathématique

Equipe MCTAO - Inria Sophia Antipolis-Méditerranée

Thèse co-dirigée par

Jean-Baptiste POMET, Stéphane RÉGNIER, et Laetitia GIRALDI

soutenue le 21 décembre 2020

Devant le jury composé de:

Madalena Chaves	Directrice de recherche	Inria Sophia Antipolis-Méditerranée	Présidente du jury
Nicolas Andreff	Professeur	Université de Franche-Comté	Rapporteur
Alain Rapaport	Directeur de Recherche	Université de Montpellier	Rapporteur
Eric C. Kerrigan	Professeur	Imperial College London	Examinateur
Laetitia Giraldi	Chargée de recherche	Inria Sophia Antipolis-Méditerranée	Encadrante
Stéphane Régnier	Professeur	Sorbonne Université	Co-directeur
Jean-Baptiste Pomet	Directeur de Recherche	Inria Sophia Antipolis-Méditerranée	Co-directeur

Modélisation et Contrôle Optimal de Micro-Nageurs Magnétiques

Résumé:
Les micro-nageurs robotiques permettent d'effectuer des opérations à petite échelle telles que l'administration ciblée de médicaments et la chirurgie peu invasive. En raison de la difficulté de miniaturiser des sources d'énergie internes, les méthodes d'actionnement externes sont préférables aux sources intégrées, une stratégie populaire étant l'aimantation du nageur ou d'une de ses parties et son actionnement avec des champs magnétiques externes. L'étude qui suit se concentre sur les micro-nageurs magnétiques flexibles qui imitent les cellules flagellées comme les spermatozoïdes dans leur conception et leur mode de locomotion. Le but de cette thèse est d'appliquer des outils numériques de modélisation et de contrôle optimal aux nageurs expérimentaux de l'Institut des Systèmes Intelligents et de Robotique (ISIR) afin d'ameliorer leur contrôle et de fournir une méthode numérique pour la conception de commandes pour les micro-nageurs flexibles. La première étape de cette thèse a été le développement d'un modèle dynamique simplifié d'un nageur magnétique flexible en trois dimensions, basé sur une approximation des forces hydrodynamiques et sur la discrétisation de la courbure et de l'élasticité du flagelle. Une identification des paramètres hydrodynamiques et élastiques du modèle permet d'avoir un nageur simulé qui présente les mêmes caractéristiques de propulsion (notamment la réponse fréquentielle du nageur) que celles mesurées expérimentalement. La seconde étape a été d'utiliser le modèle développé pour la résolution numérique du problème de contrôle optimal consistant à de trouver le champ magnétique qui maximise la vitesse de propulsion du nageur sous des contraintes sur la commande reflétant les contraintes physiquement imposées au champ magnétique. La dernière étape a été l'implémentation des champ magnétiques calculés dans le dispositif expérimental de l'ISIR et l'étude de leur performances expérimentales ainsi que de la capacité du modèle à prédire la trajectoire du nageur.

Mots-clés: Micro-nageurs magnétiques, Natation à faible nombre de Reynolds, Interactions Fluide-Structure, Contrôle Optimal.

Modeling and Optimal Control of Magnetic Micro-Swimmers

Abstract:

Robotic micro-swimmers are able to perform small-scale operations such as targeted drug delivery, and minimally invasive medical diagnosis and surgery. However, efficient actuation of these robots becomes more challenging as their size decreases. Hence, wireless actuation is preferable over built-in actuation sources, one of the most popular strategies being the magnetization of parts of the swimmer and its actuation with an external magnetic field. In this thesis, we focus on flexible magnetic micro-swimmers that are similar to flagellated cells in their design and flagellar propulsion. Our goal is to use numerical modeling and optimal control tools to improve the performance of existing swimmers made at the ISIR laboratory (Institut des Systèmes Intelligents et de Robotique) and to propose a numerical control design method for experimental flexible micro-swimmers. Firstly, a simplified 3D dynamic model of a flexible swimmer has been developed, based on the approximation of hydrodynamic forces and the discretization of the curvature and elasticity of the tail of the swimmer. By fitting the hydrodynamic and elastic parameters of our model accordingly, we are able to obtain propulsion characteristics (mainly the frequency response of the swimmer) close to those experimentally measured. Secondly, we numerically solve the optimal control problem of finding the actuating magnetic fields that maximize the propulsion speed of the experimental swimmer under constraints on the control that reflect the constraints physically imposed on the magnetic field. The optimal magnetic fields found via numerical optimization are then implemented in the ISIR experimental setup in order to benchmark the experimental performance of the computed controls and the ability of the model to predict the trajectories of the experimental swimmer.

Keywords: Magnetic micro-swimmers, Low Reynolds number locomotion, Fluid-structure interactions, Optimal Control.

Contents

List of Figures

Chapter 1

Introduction

Contents

Microrobotics is a rapidly growing discipline that has a wide array of potential application areas such as environmental monitoring and remediation, minimally invasive medicine, and micro-assembly. These applications often require that microrobots swim in a fluid. This is no easy task, as the physics governing swimming at the micro-scale significantly differs from the physics of swimming at the macroscopic scale. At very small scales, swimming occurs at low Reynolds number, which means that viscosity prevails over inertia. This entails that swimming at the microscale is remote from common intuition because of the absence of inertia. In order to design microrobots that could efficiently swim at the micro-scale, researchers took inspiration from biological microorganisms that have evolved various mechanisms to efficiently swim at the microscale such as bacteria and sperm cells.
Given that built-in energy sources are too difficult to implement at the micro-scale, most swimming micro-robots are actuated through remote power sources. Arguably, the most popular remote actuation strategy is the magnetization of parts of the swimmer and its actuation with external magnetic fields. In the last decade, numerous studies were devoted to the design, manufacturing, and motion control of

magnetic micro-swimmers, however, most if not all of these studies used empirically chosen time-varying fields to induce propulsion. For instance, nearly all magnetic helical swimmers are actuated by rotating magnetic field to induce their corkscrew-like propulsion, and most flexible magnetic swimmers are actuated by some sort of sinusoidal magnetic field to induce the deformations necessary for propulsion. Naturally, these commonly used magnetic actuation patterns are simple, effective, and popular methods to actuate magnetic swimmers, but this begs the question of whether they are optimal, and whether better performing time-varying magnetic fields could be found. This thesis aims at answering this question for flexible magnetic micro-swimmers by providing a computational framework for their optimal control and applying this control design method to an experimental swimmer.
The remainder of this introduction is organized as follows: Firstly, we give a general presentation of the physical context of the locomotion at the micro-scale. Secondly, we review the experimental design, actuation, and motion control of magnetic microswimmers as well as past theoretical and numerical studies that focused on swimming opimization at low Reynolds number. Lastly, we describe the objectives of this thesis and give its outline.

1.1 Swimming at the micro-scale

1.1.1 The Navier-Stokes Equations

The general governing equations in fluid dynamics are the Navier-Stokes equations, which, in the case of incompressible Newtonian fluids, take the form :

$$\begin{cases} \rho\dfrac{\partial \boldsymbol{u}}{\partial t} + \rho(\boldsymbol{u}.\nabla)\boldsymbol{u} = -\nabla \boldsymbol{p} + \mu\nabla^2\boldsymbol{u} + \rho\boldsymbol{g}\,, \\ \nabla.u = 0, \end{cases} \tag{1.1}$$

where $\boldsymbol{v}$ is the flow speed, $\boldsymbol{p}$ is the fluid-pressure field, $\boldsymbol{g}$ is the external force on the fluid per unit of mass, ρ is the fluid density and μ is the fluid viscosity. The Navier-Stokes equations can be non-dimensionalized in order to reduce the number of parameters and to gain insight into the relative magnitude of the terms present in the equation. Let us consider a characteristic velocity U, a characteristic length L, and a characteristic time T and introduce the following dimensionless variables :

$$\boldsymbol{u^*} = \frac{\boldsymbol{u}}{U}, \boldsymbol{x^*} = \frac{\boldsymbol{x}}{L} \quad \boldsymbol{t^*} = \frac{\boldsymbol{t}}{L} \quad p^* = \frac{pL}{\mu U}. \tag{1.2}$$

Scaling the terms in the Navier-Stokes equations using these characteristic scales leads to the dimensionless form [Pozrikidis & Jankowski 1997] :

$$\begin{cases} \beta\dfrac{\partial \boldsymbol{u}^*}{\partial t^*} + Re\ \boldsymbol{u}^*.\nabla\boldsymbol{u}^* = -\nabla p^* + \nabla^2\boldsymbol{u}^* + \dfrac{Re}{Fr^2}\dfrac{\boldsymbol{g}}{|\boldsymbol{g}|}, \\ \nabla p^* = 0, \end{cases} \tag{1.3}$$

where $\beta = \frac{\rho L^2}{\mu T}$ is a frequency parameter that expresses the relative magnitudes of the inertial acceleration force and the viscous force, $Re = \frac{\rho UL}{\mu}$ is the ratio of inertial forces to viscous forces, known as the *Reynolds number* of the fluid, and $Fr = \frac{U}{\sqrt{gL}}$ is the ratio of the flow inertia to the external field, known as the *Froude number*. The derivation of the Navier-Stokes equations and their non-dimensionalized form can be found in fluid mechanic texts such as [Pozrikidis & Jankowski 1997]. In the absence of external forcing, the time scale T is equal to $\frac{L}{U}$ and thus β reduces to Re. The Reynolds number describes the transport properties of a fluid or a particle moving in a fluid. At the macroscopic scale, the Reynolds number is high, which means that inertial forces are dominant over viscous forces. For example, larger organisms such as fish or humans swimming in water experience a Reynolds number in the range of 10^4 [Muller *et al.* 2000]. On the other hand, for micro-organisms, the Reynolds number is between 10^{-4} (for bacteria such as E.coli) and 10^{-2} (for sperm cells) [Brennen & Winet 1977]. In this case, the inertial terms in the Navier-Stokes equations can be omitted, leading to the Stokes equations :

$$\begin{cases} \mu\nabla^2 u - \nabla p = -\rho g, \\ \nabla . u = 0, \end{cases} \tag{1.4}$$

which provide a good approximation for the flow up to $Re = 0.1$ [Proudman & Pearson 1957]. When the force field g is conservative, such as gravity, it can be expressed as a gradient, which means that it can be lumped together with the pressure p, hence, the above equations are often written without the force term.
In addition to the Stokes equations, boundary conditions that depends on the physical setting must be met in order to solve the flow field. In particular, let us consider a body swimming at low Reynolds number in a fluid. In this context, swimming is broadly defined as the generation of a net displacement through periodic shape changes. In this case, the necessary boundary conditions stem from the coupling of the so-called no-slip condition, which states that the fluid has zero velocity relative to the surface of the swimmer at the interface, and Newton's law, i.e. the balance of forces and torques on the swimmer [Lauga & Powers 2009]. The full derivation of the equations of swimming at low Reynolds number is not in the scope of this thesis, and it can be found in [Lohéac & Munnier 2014].

1.1.2 General properties of Stokes flow

One important property of the Stokes flow is that it is instantaneous, meaning that it has no dependence on time other than through time-dependent boundary conditions, which entails that the response of the fluid to the motion of boundaries is instantaneous. As a consequence, in the limit of low Reynolds number, the rate at which the momentum of a swimmer is changing can be neglected in favor of the forces from the surrounding viscous fluid, and Newton's law applied to the swimmer simplify to a balance of forces and torques.
Another consequence of the time-independence of Stokes flow is that it is reversible

in time. This entails that a non-zero propulsion can be only achieved if the series of shape changes undergone by a deformable swimmer are non-reciprocal in time. This time-irreversibility condition is famously known as Purcell's "Scallop Theorem" [Purcell 1977], named after the fact that a scallop cannot generate a non zero net displacement at low Reynolds number by periodically opening up and closing its shell.
In [Purcell 1977], Purcell proposed a simple example of non-reciprocal motion by a theoretical two-hinged swimmer composed of three rigid links rotating out of phase with each other, which is depicted in Figure 1.1. The two hinges offer two degrees of freedom and the swimmer can go through a series of angle configurations. The reciprocal series of configurations ABCBA leads to a zero net displacement of the swimmer, whereas the non-reciprocal series of configurations ABCDA induces a net displacement after a cycle.

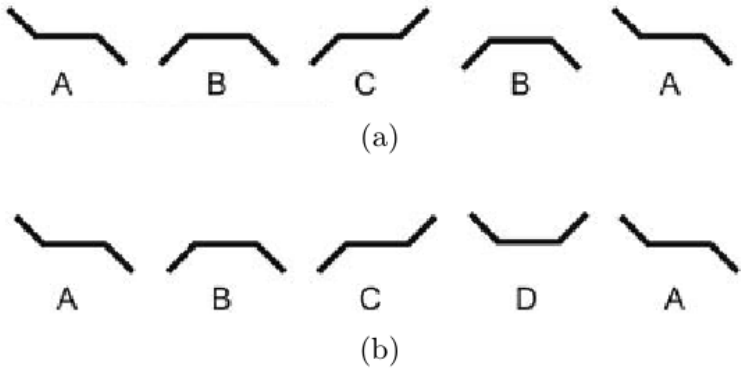

Figure 1.1: Reciprocal and non-reciprocal configurations of the Purcell swimmer.

In nature, this time-irreversibility condition is met by swimming micro-organisms in various ways : for example, bacteria such as *Escherichia coli* and *Salmonella typhimurimum* propel themselves by rotating bundle of flagella that, which creates travelling helical waves [Powers 2002], single flagellated eukaryotic cells such as spermatozoa swim by propagating a bending wave in their flagellum [Friedrich *et al.* 2010], and ciliates such as *Opalina* swim by non-reciprocal shape deformations resulting from the asymmetrical beating of their cilia [Mitchison & Mitchison 2010].

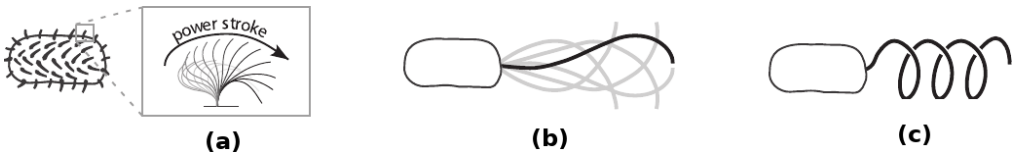

Figure 1.2: locomotion methods at the micro-scale [Abbott *et al.* 2009]: $(\boldsymbol{a})$: propulsion by cilliary beating,$(\boldsymbol{b})$:propulsion by flagellar beating, $(\boldsymbol{c})$: corkscrew-type rotating propulsion

Given the linearity of the Stokes' equations, the solutions to many complex flows can be constructed by the superposition of fundamental solutions of the Stoke's equations [Chwang & Wu 1975]. The most basic solution is the *stokeslet*, which is the solution of the Stokes' equations generated by a single point forcing $\boldsymbol{F}$ acting at the origin in an unbounded fluid. Hence, the stokeslet is the solution of :

$$\begin{cases} \mu\nabla^2 u - \nabla p = -\boldsymbol{F}.\delta(\boldsymbol{r})\,, \\ \qquad\qquad \nabla.u = 0, \\ \qquad\qquad |u|, p \to 0 \text{ as } \boldsymbol{r} \to \infty. \end{cases} \tag{1.5}$$

The solutions for the pressure p and the velocity u for u and p vanishing at infinity are [Chwang & Wu 1975, Hancock 1953]:

$$\begin{cases} u(r) = \boldsymbol{F}.\dfrac{1}{8\pi\mu}\left(\dfrac{\mathbb{I}}{|\boldsymbol{r}|} + \dfrac{\boldsymbol{r}\boldsymbol{r}}{|\boldsymbol{r}^3|}\right)\,, \\ p(r) = \dfrac{\boldsymbol{F}.\boldsymbol{r}}{4\pi|r|^3}. \end{cases} \tag{1.6}$$

Due to the linearity of the Stokes flow, it follows that a derivative on any order of the fundamental solution above is a solution of the Stokes equations. For example, one derivative leads to force dipoles, with flow fields decaying as $\frac{1}{r^2}$ and two derivatives lead to a source dipole (also known as a Stokes doublet), etc. Another application for these singularities is the construction of asymptotically accurate solutions of the Stokes flow using the matched asymptotic expansion method. In particular, this method was widely used in the early studies of slender filaments deforming at low Reynolds number, and lead to the development of the Slender Body Theory framework, which will be detailed in the next chapter.

1.1.3 Numerical methods for the resolution of the Stokes equations

Several theoretical and numerical frameworks of varying accuracy were developed for the resolution of the Stokes equations in the context of micro-swimmers. The most sophisticated models use PDE-based methods such as the regularized Stokeslet method [Rodenborn *et al.* 2013], which is a method based on the superposition of exacts solutions of the Stokes equations with forces given by regularized delta functions (hence the name "regularized Stokeslet", as these solutions can be seen as a modified

expression of the Stokeslet where the singularity has been removed). Another methods for the resolution of Stokes Flow are the Boundary Element Method [Ramia *et al.* 1993, Pozrikidis *et al.* 1992], which is a numerical approach for the resolution of linear partial differential equations that can be formulated as integral equations (i.e. when the governing equations have an associated Green function), and finite element methods [Tabak & Yesilyurt 2014]. These methods are too computationally expensive to be used in the context of our study, given the fact that the elasticity of the tail of the swimmer and the magnetic effect must be included along with the hydrodynamic effects, and given our goal to use a dynamical model to compute optimal magnetic fields. Therefore, in this thesis, we choose to use the Resistive Force Theory framework [Gray & Hancock 1955], detailed in chapter 2, which is an approximate method applicable to the motion of slender bodies at low-Reynolds number. The advantage of using this approximation is that it leads to an computationally cheap ODE-based model and that it lends itself well to the inclusion of elastic and magnetic effects.

1.2 Bioinspired Magnetic Microswimmers

The various locomotion methods that have been evolved by micro-organisms to swim at low Reynolds number inspired the design of biomimetic, micro-scale swimming robots that have the potential to perform a variety of small-scale operations such as the manipulation and assembly of microscopic components ,targeted drug delivery [Qiu *et al.* 2015, Patra *et al.* 2013], and minimally invasive medical diagnosis and surgery [Mack 2001, Fusco *et al.* 2014]. Given that powering these devices through built-in energy sources is a challenging task at their scale, most actuation methods for robotic micro-swimmers rely on wireless remote power sources, such as light-powered actuation [Dai *et al.* 2016] , acoustic actuation [Ahmed *et al.* 2016], or magnetic actuation [Dreyfus *et al.* 2005]. Of all wireless actuation methods, magnetic actuation is one of the most popular choices. This method of actuation has been prevalent in the literature for various types of micro-swimming robots, firstly because of its cost-effectiveness, given that relatively weak time-varying magnetic (1 mT) fields are sufficient to induce propulsion at Low Reynolds [Khalil *et al.* 2014], and secondly, because of its relative harmlessness to the human body which makes it suited for potential medical applications, and its capacity to control the direction of swimming direction by aligning the ferromagnetic parts of the swimmer to the external field. Most magnetic micro-swimmers are designed using either bacteria such as *E.coli* or flagellated cells such as sperm cells as a template. In the first case, the propulsion at the micro-scale is obtained by rotating an helical propeller in a corkscrew motion. In the second one, the propulsion is induced by propagating a traveling wave through the tail of the swimmer. In this thesis, we restrict our attention to this second type of micro-robots.

1.2.1 Flexible micro-swimmers

One of the simplest designs for swimming micro-swimmer is based on flagellated cells like spermatozoa. For this class of robots, locomotion is obtained by magnetizing parts of the micro-swimmer and inducing a non-reciprocal deformation of the tail by actuating the magnetized parts with an oscillating magnetic field. In this thesis, we will focus on the optimal control of these kind of magnetic swimmers. The study of flexible magnetic micro-swimmers was pioneered by the experimental work of [Dreyfus *et al.* 2005], where the first artificial micrometer-long magnetic swimmer was constructed. In this work, the swimmer, shown in Figure 1.3(a), was made of a tail consisting of a flexible chain of magnetized beads connected by DNA links which are attached to a red blood cell and actuated by an oscillating magnetic field. This attached red-blood cell is necessary for the locomotion of Dreyfus' swimmer because it breaks the symmetry of the travelling wave along the bead chain, which results in a non-reciprocal deformation. Another way of breaking this symmetry is to design an asymmetric or imperfect chain of magnetized beads like the nano-bead chain swimmer of [Benkoski *et al.* 2010]. Another approach is to design swimmers with a magnetized head attached to a flexible tail. For example, Khalil et al. [Khalil *et al.* 2014] presented a magnetic micro-swimmer which imitates the shape of a sperm-cell (Figure 1.3,(a)). It was composed of an ellipsoid head and a trapezoidal tail made of a polymer and a $200nm$ thick cobalt–nickel magnetic layer that was patterned on the head, with whole dimension of $5.2\mu m$ in thickness and $322\mu m$ in length, and head dimension of $42\mu m$ in length and 27 in width. When an alternating uniform magnetic field is applied, the head part will respond to the applied field to oscillate and then the tail part will generate propulsion. This swimmers attained a propulsion speed of $158\pm32\mu m.s^{-1}$ in water at a weak oscillating magnetic field (less than 5mT) at a $45Hz$ frequency. An alternative design for flexible micro-swimmers was proposed in [Pak *et al.* 2011], were the swimmer was a flexible nanowire comprised of a $1.5\mu m$ long nickel head and a $4\mu m$ long flexible silver tail bended into an unsymmetrical shape. It was manufactured using a common template directed electro-deposition protocol. When a weak rotating magnetic field is applied, the nickel head will start to rotate and then drive the tail to rotate at different amplitude, breaking the system symmetry and inducing propulsion at the speed of $21\mu ms^{-1}$ (about 4 body lengths per second). Multi-link nanowire-based swimmers were presented in [Jang *et al.* 2015] (1.3,(c)). These structures consisted of an elastic and rigid magnetic links joined by flexible polymer hinges. Nanoswimmers with one, two, and three links were magnetically propelled by oscillating magnetic fields and exhibited a non-reciprocating motion. While 1- and 2-link swimmers operated as flexible oars, the 3-link Purcell-like swimmer displayed an S-like motion with the occurrence of a propagating wave.

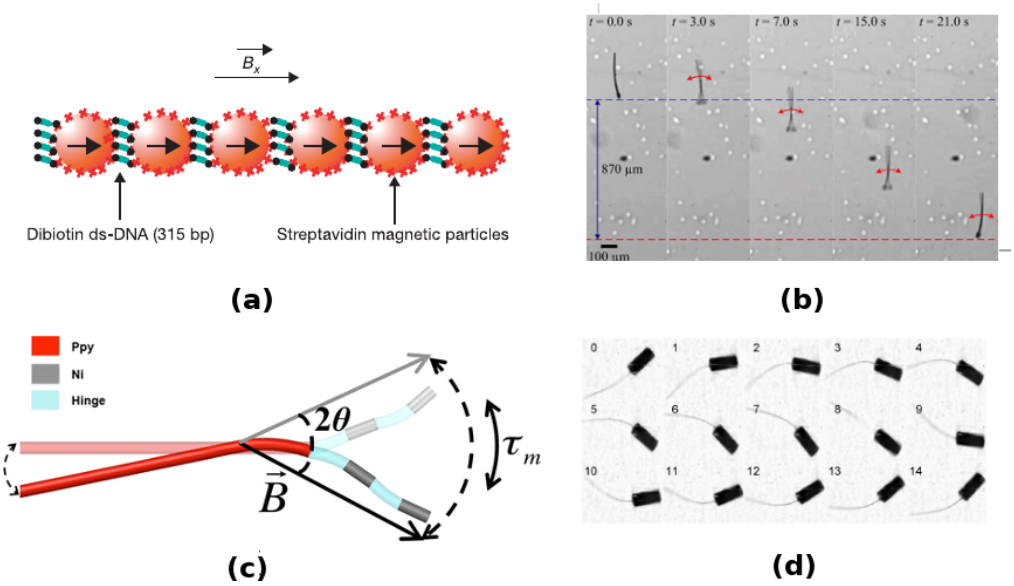

Figure 1.3: Some flexible micro-swimmers in the literature (***a***) : Design of the magnetic swimmer presented in [Dreyfus *et al.* 2005], consisting of magnetic nano-beads joined by DNA strands. (***b***): Sperm-like magnetic micro-swimmer [Khalil *et al.* 2014] , (***c***) : Flexible 2-linked magnetic nano-wire [Jang *et al.* 2015], (***d***) : millimeter-scale low Reynolds swimmer with a magnetic head and a flexible tail [Khalil *et al.* 2016].

1.2.2 Helical micro-swimmers

These types of microswimmers imitate the motion of several microorganisms such as bacteria by rotating a helical flagella to generate a corkscrew-like translational movement. The propulsion of these devices is obtained by applying a rotating magnetic field to a helical magnetic swimmer with a magnetized head [Zhang *et al.* 2009, Mahoney *et al.* 2011a, Hwang *et al.* 2010] or tail [Ghosh & Fischer 2009]. The fabrication of helical micro/nanostructures is more challenging that flexible tails, because of the complex three-dimensional geometry of the swimmer, which entails that traditional microfabrication techniques based on the deposition or removal of thin layers of material are not adapted. Helical structures have been manufactured by several methods. For instance self-scrolling [Zhang *et al.* 2009] consists in creating a planar bilayer pattern and removing layers while simultaneously applying an internal stress that makes the layers assemble in an helical structure. This method was used in [Zhang *et al.* 2009] to construct the first helical swimmers of a size comparable to E. coli, called "Artificial Bacterial Flagella (ABF)",seen in Figure 1.4 (*b*), with a length of approximately $38\mu m$ and a maximum swimming speed of $18\mu m.s^{-1}$ (equivalent to 0.5 body-length per second) under a rotating magnetic field at a $2mT$ frequency. Another method is direct laser writing (DLW), which is a 3D lithography method that can write polymer structures of arbitrary shapes. This method was

used in [Tottori *et al.* 2012] to design claw-shaped helical microswimmers (Figure 1.4,(a)) used to transport objects, with lengths varying from $4\mu m$ to $65\mu m$. Other fabrication methods include glancing angle deposition [Schamel *et al.* 2014], which uses spherical seeds on which helical pillars are grown through the rotation of a tilted stage during evaporation , template-assisted electrodeposition (TAE) [Zeeshan *et al.* 2014], which is a technique for synthesizing metallic nanomaterials with controlled shape and size, and biotemplating synthesis (BTS) [Schuerle *et al.* 2012], which relies on using large biomolecules as a sort of mold for the synthesis of metallic and inorganic compound nanostructures.

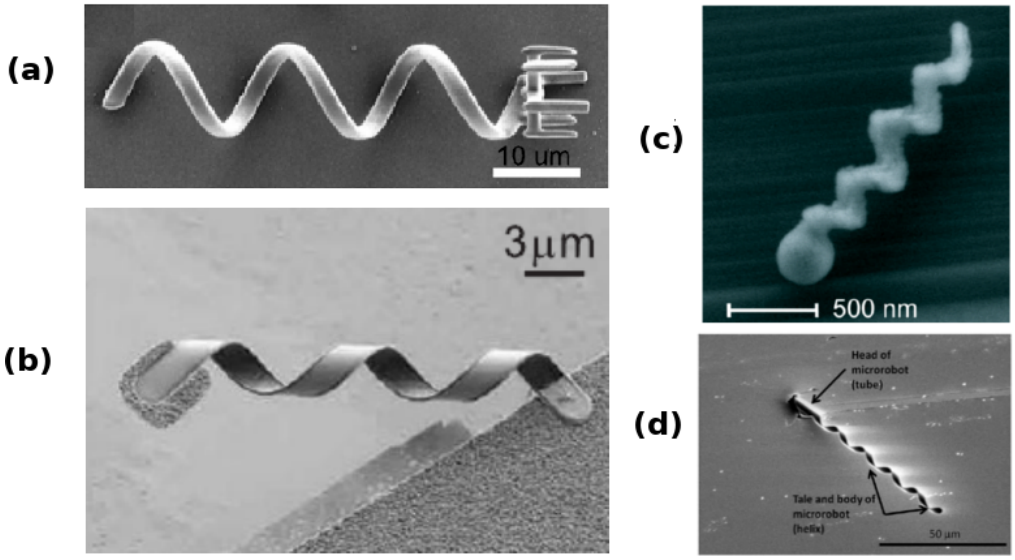

Figure 1.4: Some helical micro-swimmers in the literature $(\boldsymbol{a})$: Polymer helical swimmer with a claw shaped holder head [Tottori *et al.* 2012] ,$(\boldsymbol{b})$: Artificial bacterial flagella [Zhang *et al.* 2009] , $(\boldsymbol{c})$: Artificial magnetic glass nano-structured propellers [Ghosh & Fischer 2009], $(\boldsymbol{d})$: Helical nanobelt [Hwang *et al.* 2010].

1.2.2.1 Other designs

Other forms of microswimmers have been presented in the literature. For instance, the resonant magnetic micro-swimmer of [Frutiger *et al.* 2010] (seen in Figure 1.5(c)) consists of a spring-mass system of two soft-magnetic bodies joined by a spring and is actuated by magnetic fields and propelled by the impact between the two parts. Jellyfish-like micro-swimmers were constructed in [Ko *et al.* 2012] (Figure 1.5,(a)), consisting of a central body with four magnetic fins, actuated by time-varying periodic magnetic fields. Inspired by bacteria such as paramecia, cilliary microswimmers were constructed in [Kim *et al.* 2016](Figure 1.5,(b)) with a non-reciprocal movement induced by on-off magnetic fields. Achiral microswimmers consisting of a non-symmetric system of three balls actuated by rotating fields were presented in [Cheang *et al.* 2017] (Figure 1.5,(d)). In [Ye *et al.* 2014], flexible microswim-

mers with multiple flagella, actuated by rotating magnetic fields were constructed. Interestingly enough, it was also shown that a specific shape design might not be necessary for magnetic propellers, as the works of [Vach *et al.* 2013,Vach *et al.* 2015] demonstrated that structures with random shapes can also be propelled by rotating magnetic fields. The dimensionless speeds of these randomly shaped propellers were comparable to those of nanofabricated helical propellers. These results suggested that randomly shaped propellers may be a suitable choice for applications in which precise positioning and motion are not needed, and also the existence of alternative designs to helical swimmers.

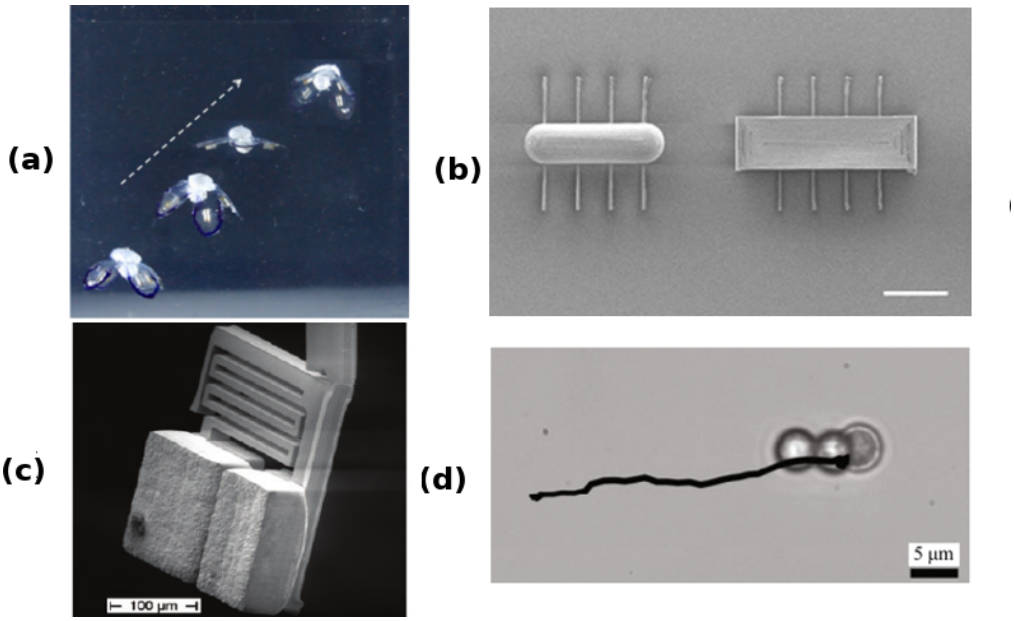

Figure 1.5: (a) : Jellyfish-like swimmer of [Ko *et al.* 2012] ,(b): Cilliary micro-swimmers [Kim *et al.* 2016] , (c) : Wireless resonant magnetic micro-swimmers [Frutiger *et al.* 2010], (d) : Achiral robotic micro-swimmer formed by an asymmetrical system of three-balls [Cheang *et al.* 2017].

1.3 Actuation and Control of magnetic micro-swimmers

1.3.1 Magnetic actuation methods

Several magnetic actuation systems were used in the literature. These systems differ by the size of the workspace and the degrees of freedom (DoF) that they provide. Let us consider an actuating magnetic field $\boldsymbol{B}$, and a magnetic swimmer with a total dipole moment $\boldsymbol{M}$. The magnetic force and torque on the swimmer are :

$$\begin{cases} \boldsymbol{F_m} = \boldsymbol{M}.(\nabla \boldsymbol{B})\,, \\ \boldsymbol{T_m} = \boldsymbol{M} \times \boldsymbol{B}. \end{cases} \tag{1.7}$$

The magnetic forces are proportional to the gradient of the magnetic field, and the magnetic torque is proportional to the magnetic field and acts to align the magnetization of an object with the direction of the magnetic field.
The simplest designs for the actuation systems of magnetic micro-swimmers rely on using Helmholtz coils pairs, which generate a homogeneous magnetic field, Maxwell coils pairs, which generate a magnetic field with a constant gradient or a combination of both types.
A Helmholtz coil pair consists of two identical circular coils aligned on the same axis and separated by a distance equal to the radius of the coils with the currents flowing through the coils that are equal and in the same direction. A Maxwell coil pair is similar to a Helmholtz coil with the coil distance increased from the coil radius R to $\sqrt{3}R$ and the currents are flowing in opposite directions through each coil. Given that one Helmholtz coil pair can generate a uniform magnetic field in one direction, three orthogonally arranged Helmholtz coil pairs can generate a uniform magnetic field in any direction of the space at the center of the setup (see Figure 1.6,(a)). This is arguably the most popular method to actuate magnetic swimmers with three degrees of freedom [Mahoney *et al.* 2011b, Zhang *et al.* 2009, Ko *et al.* 2012, Huang *et al.* 2014, Frutiger *et al.* 2010, Xu 2014]. It is difficult to produce "meaningful" forces with Maxwell coils alone, given that they require higher current intensities to have a force that's comparable with the torques generated by the Helmholtz coils. Accordingly, they are often used in setups that combine both types of coil pairs. For instance, in [Yesin *et al.* 2006], coaxial Helmholtz and Maxwell coils are mounted on a rotating platform to have a three degrees-of-freedom planar motion control of the microswimmer, whereas in [Jeong *et al.* 2011], a pair of Maxwell coils is added to a 3D Helmholtz coil system to add an uniform gradient to supply propulsion force for a screw-like microrobot to increase its velocity and give it the possibility to drill through soft tissue. In [Choi *et al.* 2009], the combination of two pairs of Maxwell coils and two pairs of Helmholtz coils (see Figure 1.6,(d)) enabled the planar motion control of micro-robots in three degrees of freedom. Stronger gradients can also be generated (at a bigger cost) by using gradient saddle coils, typically found in MRI systems, like [Mathieu *et al.* 2006] (Figure 1.6, (c)). More elaborate magnetic actuation systems rely on independently controlling the intensity flowing through individual coils instead of having the same current per coil, which allows for more liberty in the shape magnetic field generated, like the 8-Coil systems in [Kummer *et al.* 2010a] (Figure 1.6 (b)) and [Diller *et al.* 2013]. During this thesis, the experimental magnetic generation setup used consists of three orthogonal Helmholtz coil pairs and was designed and implemented in [Xu 2014].

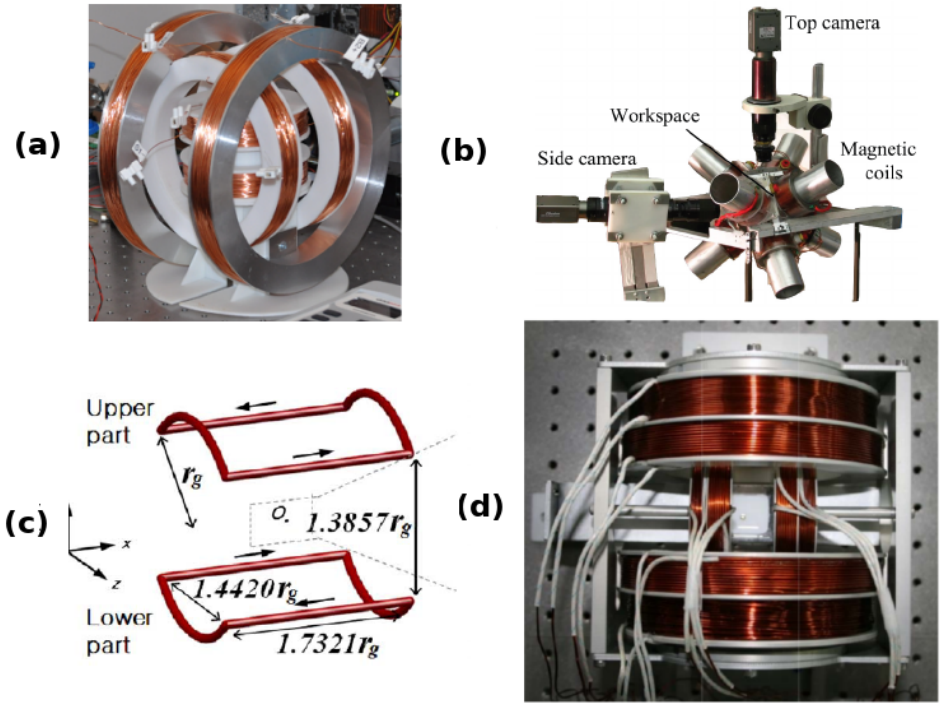

Figure 1.6: (a) : 3D orthogonal Helmholtz coil system used in this thesis [Xu 2014] ,(b): 8-coil magnetic generation system [Kummer *et al.* 2010a] , (c) : Gradient saddle coils [Mathieu *et al.* 2006], (d) : Electromagnetic actuation system consisting of two pairs of Maxwell coils and two pairs of Helmholtz coils [Choi *et al.* 2009]
.

1.3.2 Localization methods for swimming micro-robots

An important challenge for the control of swimming micro-robots is their localization. There are several methods that have been proposed to track these devices. The choice and effectiveness of the localization methods depend on several factors, like the spatial resolution that is provided, the frequency at which the position of the robot is updated (which is important for real-time control), the energetic efficiency, and the ability to locate the robot inside the body for potential in vivo applications. For instance, electromagnetic tracking can be used for micro-robots that are partly or entirely magnetic. This methods relies on a generator that emits a low frequency electromagnetic field that induces a voltage on the magnetic part of the swimmer which is picked up by a sensor [Hu *et al.* 2006]. Magnetic Resonance Imaging (MRI) systems can also be used for the localisation of micro-robots [Kósa *et al.* 2012,Pouponneau *et al.* 2014]. This method presents the advantage of serving the dual purpose of actuating magnetic swimmers with field gradients and tracking them but present some limitations as MRI systems provide images with a low spatial resolution, and are costly and not energy effective. A promising method for the

localization in soft tissues is the use of ultrasounds, which have the advantage to provide a good resolution, non invasiveness, and a high framerate (up to 100 frames per second) [Xu *et al.* 2005]. Ultrasounds are relatively low-cost but they are limited by their sensitivity to noise. Lastly, vision-based tracking relies on tracking micro-robots using cameras in combination with optical lenses. This method cannot be used for in vivo tracking but presents has several advantages compared with other imaging methods, as vision-based tracking can provide high spatial resolutions (up to 200nm) using microscopic lenses at a low energetic cost. Another advantage of vision-based tracking is that it does not interfere with magnetic actuation, unlike MRI and electromagnetic tracking systems. The experimental setup used in this thesis, detailed in Chapter 4, relies on vision-based localization.

1.3.3 Motion Control methods for micro-robots

1.3.3.1 Open loop control

Magnetic actuation has the advantage of allowing the steering of magnetic swimmers by applying an uniform field to the desired swimming direction. Hence, the magnetic control can be separated into two component, a static *orientating* field to steer the swimmer, and an actuating component that induces propulsion. The form of the actuating component of the magnetic control depends on the design of the swimmer and on the magnetic actuation system. For instance, as shown in the previous sections, rotating fields are used to generate a corkscrew-like propulsion for helical swimmers [Zhang *et al.* 2009,Mahoney *et al.* 2011a], and sinusoidal fields are used to induce propulsion for flexible swimmers [Gao *et al.* 2010a,Khalil *et al.* 2014,Dreyfus *et al.* 2005]. In these two cases, the velocity of the swimmer can be controlled by acting on the frequency of the actuating rotating or sinusoidal field. Magnetic field gradients can also be used to pull the swimmer along a given direction as done in [Yesin *et al.* 2006]. By controlling the steering magnetic field, it is possible to make micro-swimmers follow a predefined trajectory. For instance, helical micro-swimmers were navigated along arbitrary curved trajectories (for example in the shape of the characters "R" "@", or "H" [Ghosh & Fischer 2009] or a U-turn in [Mahoney *et al.* 2011b]) using a pre-programmed controller to actuate the magnetic field. Open-loop teleoperation, where the control is based on visual feedback, and where the offtrack is corrected manually, can also be used to control micro-robots. For example, in [Tottori *et al.* 2012] and [Qiu *et al.* 2015], targeted cargo transport was demonstrated by using helical micro-swimmers using open-loop teleoperation, and in [Khalil *et al.* 2016] (Figure 1.3,(*d*)), a sperm-like magnetic swimmer was steered towards a target while navigating obstacles using teleoperation.

The drawback of open-loop control is that the movement of a swimmer is sensible to many external factors that can make it stray off-path (thermal effects, non-uniformity of the magnetic field, boundary effects...), and especially its weight, given that man-made swimmers are usually heavier than their neutrally buoyant biological counterparts. Thus, gravity compensation is important for heavier swimmers, either

by taking the apparent weight of the robot into consideration when calculating the command [Mahoney *et al.* 2011b] or by generating external forces to counter the weight, as done in [Jeong *et al.* 2011] where an upward vertical magnetic force is generated by Maxwell coils to compensate the gravity.

1.3.3.2 Closed loop control

Closed-loop control of microrobots is a way to overcome the drawbacks of open-loop control, mainly their sensitivity to perturbations generated by thermal noise, boundary effects, or non-buoyancy. For holonomic microrobots driven by magnetic fields, which are generally designed to be pulled by magnetic gradients, a simple proportional-derivative (PD) or proportional-integral controller can be for the point-to-point control of their position [Kummer *et al.* 2010b, Pawashe *et al.* 2011]. However, most bimomimetic micro-swimmers are nonholonomic, which means that they are a mechanical system with constraints on the velocity that are not derivable for position constraints. This entails that simple controllers on the position of the microrobot such as a proportional-integral-derivative (PID) controller on their position cannot be used, thus, velocity-independent control is needed. For helical and flexible swimmers, a closed loop planar path-following algorithm, was introduced and implemented in the experimental setup used in the present work during the thesis of [Xu 2014] and was later generalized for 3D trajectories in [Oulmas *et al.* 2016].

1.4 Optimal swimming at Low Reynolds Number

A large part of the literature has been devoted to the swimming optimization at low Reynolds number. These works were in part motivated by the recent development of swimming micro-robots and the desire to optimize their design and actuation. Another motivation for the study of swimming optimality at low Reynolds is to provide insight into the evolutionary processes of biological micro-swimmers by showing that the locomotion strategies at low Reynolds observed in nature are optimal in the sense that they evolved in order to maximize a given energetic or efficiency-based cost.

1.4.1 Optimization of self-propelled micro-swimmers

As a consequence of the instantaneity of Stokes flow, the net distance traveled by a deforming swimmer does not depend on the rate at which it is being deformed, but only on the geometry of the shape change sequence undergone during its deformations. Hence, optimizing locomotion of swimmer at low Reynolds amounts to finding the optimal shape changes that it must undergo in order to propel.

The cost function traditionally used for characterizing and optimizing micro-swimmers is the *Lighthill efficiency* [Lighthill 1975], which is the ratio of the power required to drag the swimmer in its straightened configuration to the average power

exerted mechanically against viscosity. This is a quantitative measure of the "efficiency" at which the swimmer overcomes the drag of the surrounding fluid. In [Lighthill 1975], Lighthill characterized the optimal waveform of an infinitely long one-dimensional flagellum assuming that deformations were in the shape of a planar traveling wave using the resistive force theory framework. This work showed that the optimal flagellar wave form has a constant tangent angle to the swimming direction, which leads to a helical shaped wave in three dimensions and a smoothed saw-tooth traveling wave in two dimensions. Numerical experiments showed that the planar waves prescribed by Lighthill remained optimal in the case of finite flagella [Pironneau & Katz 1974, Tam 2008]. In [Spagnolie & Lauga 2010], The internal elacticity of flagella was taken into account in the energetic cost in order to similarly compute energy-optimal waveforms, which are found to be smooth regularizations of the classical sawtooth solutions of Lighthill. Another area of study is the optimization of the geometry of swimming flagellated micro-organisms, in particular the length of the flagellum and the dimensions of the head (often represented by a sphere or an oblate spheroid). In the case of a flagellated swimmer with a spherical head, assuming a planar sinusoidal deformation, the optimal ratio was between the length L of the flagellum and the ratio a of the body was determined to be $L/a \approx 25$ using slender-body theory [Higdon 1979b]. For helical waveforms, this ratio is closer to 10..12 [Higdon 1979c]. Other works devoted to the optimization of biological micro-swimmers include the optimization of feeding current for tethered cells [Higdon 1979a], and the influence of cell geometry on the optimal flagellar waveform [Tam 2008, Fujita & Kawai 2001]. Following these initial works, where the swimming optimization was mostly made under the assumption that the deformations were in the form of a travelling wave, the development of simple swimmer models lead to theoretical and numerical studies of the optimal deformation patterns without any presuppositions on the shape of the optimal deformations. For swimmers with a discrete shape (i.e. a shape that is described by a finite number of variable), a notable example is the numerical optimization of the actuation and design of the Purcell swimmer [Becker *et al.* 2003, Tam & Hosoi 2007], which is a simple, three-linked swimmer capable of motion by non-reciprocal motion introduced by Purcell in [Purcell 1977]. A general control-theoretical framework for the stroke optimization of axisymmetric swimmers with a discrete shape was introduced in [Alouges *et al.* 2009], with application to the optimization of the three-spheres swimmer model of [Najafi & Golestanian 2004]. For swimmers with continuous degrees of freedom, a geometrical approach was used to derive optimal swimming of deforming spheres and cylinders at low Reynolds number in [Shapere & Wilczek 1989] under the assumption of low-amplitude deformations, and [Avron *et al.* 2004] for large deformations.

1.4.2 Optimization of magnetic micro-swimmers

The initial experimental study of [Dreyfus *et al.* 2005] motivated a series of experimental and theoretical studies on the optimization of magnetic micro-robots but most of this body of work focused on the optimal design of these devices under a

presupposed magnetic actuation. For example, in [Walker & Keaveny 2013], the shape of the propeller of a rigid swimmer was optimized for energetic and velocity costs assuming a rotating magnetic field. In this work, a boundary integral formulation [Pozrikidis *et al.* 1992] was used for the modelisation of the Stokes flow around the swimmer. The infinite dimensional optimization problem was then discretized using a collocation method [Keaveny & Shelley 2011] and then solved using a variational gradient descent method. Similarly, in [Roper *et al.* 2008], the geometric parameters of a flexible magnetic filament based on the experimental swimmer of [Dreyfus *et al.* 2005] was optimized under a sinusoidal magnetic field, along with the actuating frequency and field strength. In [Gadêlha 2013], a simple model of a sperm-like swimmer consisting of an magnetized head attached to a flexible tail was used in order to study the influence of the geometry of the head and the compliance of the tail on the optimal amplitude and angular orientation of the applied oscillating field.

1.5 Thesis Objectives and Outline

In summary, there has been a substantial body of work on the design, fabrication,shape optimization, and motion control of magnetic micro-swimmers. However, most of the experimental studies on micro-swimmers still rely on on empirical choices of the magnetic actuation, using empirically chosen time-varying fields to induce propulsion. On the other hand, due to the fact that the locomotion at low-Reynolds number is inherently geometrical, there has been numerous control-theoretical studies on the optimal locomotion of self-propelled swimmers. Although these optimization studies are interesting in their own right, these results cannot be exploited in most experimental settings because the shape of magnetic swimmers cannot be controlled under the sole action of the actuating magnetic field.
This thesis aims to bridge the gap between the experimental studies on magnetic micro-swimmers and the optimal control studies that were focused on self-propelled swimmers by providing a framework for the numerical computation of optimal actuation for flexible magnetic micro-swimmers and experimentally validating the computed optimal fields on a flexible low Reynolds number swimmer. Our approach is based on the numerical resolution of optimal control problems under the constraints of an approximate dynamic model of the swimmer's displacement.
The first contribution of this work, detailed in **Chapter 2**, and a key part of our optimal control design method, was the development of an approximate 3D dynamic model that predicts the trajectory of a magnetic micro-swimmer under a given magnetic field. The model is based on the simplification of the low Reynolds number hydrodynamics using the Resistive Force Theory framework [Gray & Hancock 1955] and on the discretization of the shape of the swimmer. With this model, we aimed to achieve a trade-off between the accuracy of the simulated trajectories in predicting the horizontal displacement of an experimental swimmer and the numerical complexity of the model, as it needs to be computationally inexpensive enough to be

used to numerically solve optimal control problems. Due to the simplification of the hydrodynamic and elastic effects, and the discretization of the shape of the swimmer, the dynamics of the swimmer are a ODE controlled system that is affine in the components of the actuating magnetic field, and thus the optimization of the displacements of a flexible magnetic swimmer amounts to solving a finite-dimensional optimal control problem. By fitting the hydrodynamic and elastic parameters of our model accordingly, we are able to obtain propulsion characteristics (mainly the frequency response of the swimmer) close to those experimentally measured.

In **Chapter 3**, we address the optimal control problem of finding the actuating magnetic fields that maximize the propulsion speed of the experimental swimmer and solve it numerically, using the model developed in chapter 2 as a dynamic constraint. The goal of this chapter is to present better performing alternatives to the sinusoidal actuation that is prevalent in the literature. In particular, we solve the optimal control problem of maximizing the horizontal displacement of the swimmer under various constraints on the actuating magnetic field that mimic the degrees of freedoms provided by experimental magnetic field generation setups. Two classes of optimal control problem are solved. The first one consists in maximizing the displacement of the swimmer over a fixed time frame and their solutions gives a physical limit of the swimming speed that can be achieved with a magnetic field. The second class of optimal control problems is more application-orientated, and consists in maximizing the displacement of the swimmer under the constraint of a periodic deformation. The aim of this latter formulation is to obtain an optimal actuation pattern that can be indefinitely repeated over time in order to drive the swimmer in experiments. One of the main findings of this numerical study is the computation of non-planar actuation patterns that leads to novel 3D trajectories for flexible low-Reynolds swimmers.

Lastly, **Chapter 4** is devoted to the experimental implementation of the computed optimal actuation using the setup developed in the previous PHD theses of [Xu 2014] and [Oulmas 2018], showing that the dynamic model developed in chapter 2 can be used to design optimal controls that are usable in experiment, and that it can accurately predict the horizontal displacement of an experimental low-Reynolds swimmer.

Chapter 2

Dynamic Modeling of a Slender Low Reynolds Swimmer in 3D

Contents

2.1 Introduction

To reiterate the goal of this thesis, we aim to develop a computational framework for the optimal control of experimental flexible magnetic low-Reynolds swimmers. To achieve this, the first step in this study is to develop a computationally inexpensive dynamic model that is able to predict the displacements of the experimental ISIR swimmer in 3D under a given actuating magnetic field. Simulating the displacements of flexible magnetically driven low-Reynolds swimmers is a complex problem because of the coupling between the hydrodynamic effects, the elasticity of the tail, and the magnetic action, and thus a full description of the dynamics of the swimmer would require the resolution of a system of coupled partial differential equations that is too costly to be used in an optimization process. Hence, the main difficulty of

developing the model was the necessary trade-off between its accuracy, as it needs to reliably predict the displacements of the experimental swimmer, and its numerical complexity, as it needs to be computationally inexpensive enough to be used to numerically solve optimal control problems. To tackle this trade-off, a simplified approach to modeling the swimmer in 3D was used where the hydrodynamic effects are simplified by using a local drag approximation (Resistive Force Theory [Gray & Hancock 1955]) and where the shape of the tail is discretized into an articulated chain of N slender rods, generalizing the planar swimmer models of [Moreau *et al.* 2018, Alouges *et al.* 2013]. Using these simplifications, the dynamics of the swimming robot are written as a ODE control system that is affine in the components of the actuating magnetic field.
The dynamic modeling of a slender-self propelled swimmer, were it is assumed that there is no external forces and torques acting on the swimmer and that it propels by controlling its shape deformations, will also be presented in this chapter. Although this latter formulation is not the main object of study in this work, it shows that the model developed here is a useful and computationally inexpensive tool for the modelisation of biological flagellated micro-swimmers, and it will be used to benchmark the hydrodynamics of the model by simulating the 3D sperm cell trajectories of [Jikeli *et al.* 2015].
This chapter is organized as follows: First, we describe the Resitive Force Theory (RFT) framework, and its origins stemming from the study of biological microswimmers. Next, we give an overview of the RFT-based modelisations of flexible filaments at low Reynolds number. Following this,we present the dynamic model developed during this thesis and derive the equations of motion for a self-propelled low-Reynolds swimmer and for a magnetically actuated swimmer with a passive elastic tail. The self-propelled swimmer model is used to qualitatively validate the hydrodynamics of the model by reproducing the sperm cell trajectories observed in [Jikeli *et al.* 2015]. After this validation, we show that our magnetic micro-swimmer model can predict the horizontal displacements of experimental low Reynolds swimmers after fitting the elastic and hydrodynamic parameters to experimental data.

2.2 Resistive Force Theory approximation

2.2.1 Overview

Resistive force theory (RFT) was introduced by Gray and Hancock in [Gray & Hancock 1955], based on prior work by Hancock in [Hancock 1953] to approximate the hydrodynamic forces on a slender filament deforming at low Reynolds number by neglecting the interactions on the global scale in favor of the local anisotropic friction of the surface of the slender body with the nearby fluid. The gist of this theory is that, at low Reynolds number and for a very slender filament, one can establish a linear relationship between the viscous drag density on an infinitesimal section of the filament and its velocity relative to the surrounding fluid.From this, one is able to compute the viscous forces and torques on a moving and deforming

slender filament by summing the density over the filament. Neglecting the inertial effects due to the low Reynolds approximation, the equations of motion for the filament stems from the balance of the hydrodynamic forces and torques.

Let us consider a thin filament with a circular cross section immersed in a fluid, assuming Stokes flow and a point $\boldsymbol{x}(\boldsymbol{s})$ of arclength s, on the filament. We decompose its velocity $\dot{\boldsymbol{x}}(\boldsymbol{s})$ into tangential, normal, and binormal components :

$$\dot{\boldsymbol{x}}(\boldsymbol{s}) = \dot{\boldsymbol{x}}(\boldsymbol{s}).\boldsymbol{T} + \dot{\boldsymbol{x}}(\boldsymbol{s}).\boldsymbol{N} + \dot{\boldsymbol{x}}(\boldsymbol{s}).\boldsymbol{B}. \tag{2.1}$$

The RFT states that the hydrodynamic force density $f(s)$ can be approximated as :

$$\boldsymbol{f}(\boldsymbol{s}) = k_{\parallel}\dot{\boldsymbol{x}}(\boldsymbol{s}).\boldsymbol{T} + k_{\perp}\dot{\boldsymbol{x}}(\boldsymbol{s}).\boldsymbol{N} + k_{\perp}\dot{\boldsymbol{x}}(\boldsymbol{s}).\boldsymbol{B}\,, \tag{2.2}$$

Where $k_{\parallel}$ and $k_{\perp}$ are the RFT coefficients and depend only on the geometry of the swimmer. From this, the net hydrodynamic forces and torques (around an arbitrary point $\boldsymbol{x_0}$ on the filament are computed in this form :

$$\boldsymbol{F} = \int_0^L \boldsymbol{f}(s)ds\,, \tag{2.3}$$

and

$$\boldsymbol{T} = \int_0^L (\boldsymbol{x_i}(s) - \boldsymbol{x_0}) \times \boldsymbol{f}(s)ds. \tag{2.4}$$

In addition to the temporal symmetry breaking condition arising from the time reversibility of the Stokes equations, a non zero net displacement of the filament can only be attained if spatial symmetry is broken as well by having the tangential drag on the moving filament swimmer lower than the normal drag, or, in another words, by having the propelling tail present friction anisotropy with the surrounding fluid, [Gray & Hancock 1955, Alvarez *et al.* 2014], which entails $k_{\perp} > k_{\parallel}$ as a condition for propulsion. In the limit of an infinitely slender filament, the anisotropy ratio between the perpendicular and parallel drag coefficients for biological flagellated swimmer is equal to 2, as shown in [Gray & Hancock 1955]. In nature, this anisotropy ratio is closer to 1.7-1.8, as measured experimentally in studies such as [Brokaw 1965, Friedrich *et al.* 2010] .

The difficulty in using RFT lies in determining the values of the drag coefficients. Most theoretical studies derive these values from an approximate analysis of the flow around the slender body using slender-body theory, which consists in taking into account the slenderness of a body immersed in a low Reynolds number fluid in order to approximate the flow around it. The method to construct such approximate solutions of the Stokes flow is by distributing fundamental singularities of the Stokes flow along an axis of the body in order to satisfy the no-slip boundary condition. For example, in the work [Hancock 1953], which served as a basis for the development of Resistive Force Theory in [Gray & Hancock 1955], the asymptotic solution of the flow around an infinitely slender filament deformed by a travelling wave was constructed by placing two types of singularities of the Stokes equations along the line of the

centres of the cross-sections of the filament. The first singularity is the fundamental solution generated by a single point force, known as a Stokeslet. The second one is the fundamental solution generated by a point source dipole, also known as a "Stokes doublet". The asymptotic solution is then constructed by placing these two singularities along the centerline of the filament, choosing the weightings in order to satisfy the no-slip boundary condition. From this approximate solution, as shown in [Gray & Hancock 1955], a linear relationship between the drag forces and the velocities can be established by discarding the terms where the slenderness ratio appears. From this, Gray and Hancock proposed values for these coefficients under the assumptions that the filament is infinitely slender and that it is deformed by a sinusoidal wave :

$$\begin{cases} k_{\parallel} = \dfrac{2\pi\mu}{log(\frac{2\lambda}{a}) - \frac{1}{2}}, \\ k_{\perp} = 2k_{\parallel}, \end{cases} \tag{2.5}$$

,

where μ is the viscosity of the fluid, r is the cross-sectional radius of the filament and λ is the wavelength of the flagellar beat pattern. Here, the anisotropy ratio $\frac{k_{\perp}}{k_{\parallel}} = 2$ is a consequence of considering an infinitely slender filament. In nature, most flagellated swimmers have an anisotropy ratio closer to $1.6 - 1.8$ (as measured in experimental studies such as [Brokaw 1965, Friedrich *et al.* 2010]. These initial values have been improved upon in a variety of subsequent works. For example in [Lighthill 1976], the proposed values for the coefficients take the following form for a filament deforming by travelling helical wave or a planar bending wave of small amplitude are :

$$\begin{cases} k_{\parallel} = \dfrac{4\pi\mu}{\frac{log(0.18\lambda)}{a}} \\ k_{\perp} = \dfrac{2\pi\mu}{\frac{log(0.18\lambda)}{a} + \frac{1}{2}} \end{cases} \tag{2.6}$$

.

These "classical" analytical values for the drag coefficients allowed for an accurate analysis of the movement of some flagellated micro-swimmers, but were of limited use for other cases due to the underlying simplifying assumptions that they were derived from, mostly the flagellar waveform and its amplitude. Another point of inaccuracy is the fact that these coefficients stem from a first-order approximations where the errors terms are logarithmic with respect to the slenderness ratio ([Lighthill 1976, Cox 1970]), which are non negligible even in the case of flagella where the slenderness ratio is around 10^{-3}. However, with the advent of new technologies that allowed high-precision measurements of the kinematic data and/or the viscous forces of slender micro-swimming organisms, it is now possible to characterize the values of the RFT coefficients from experimental data. For example, they have been experiments where the RFT coefficients have been evaluated using kinematic data from high-speed imaging [Schulman *et al.* 2014, Friedrich *et al.* 2010].

Another method is to perform average force measurements in optical trap, as done in [McCord *et al.* 2005, Chattopadhyay *et al.* 2006].

2.2.2 Limitations of Resistive Force Theory

The main limitation of Resistive Force Theory based modelisations is that it neglects long-range hydrodynamic interactions. Hence, the RFT is inaccurate for geometries where these interactions are important, for example in the case of swimmers that propel by rotating an helical flagella, and for configurations where the flexible filament is curled up or where the filament must provide a substantial thrust to overcome the drag on an attached cell body, as with bacteria for instance [Rorai *et al.* 2019, Giuliani *et al.* 2018, Spagnolie & Lauga 2011].

2.2.3 Elastohydrodynamic Formulations and numerical methods

The usefulness of Resistive Force Theory resides in the fact that it's simple enough to be included in more complex models. In particular, it can be used in frameworks that take into account elastic deformation in order to model the fluid-structure interactions of inextensible elastic filaments at low Reynolds number. One of the main biological applications for these models is the study of the internal mechanics of flagellar bending in biological micro-swimmers, as it is done in [Fu *et al.* 2008, Spagnolie & Lauga 2010, Gadêlha *et al.* 2010]. The other application for these simplified elastohydrodynamic models is the modelisation of the passive tails of driven filaments and in particular, magnetic micro-swimmers [Wiggins *et al.* 1998, Lauga 2007, Roper *et al.* 2008, Gadêlha 2013].

Continuous, PDE-based models were used in numerous studies to describe the fluid structure interaction [Tornberg & Shelley 2004, Lowe 2003]. In these models, the force balance between the elastic force and the hydrodynamic drag leads to a hyperdiffusive fourth-order PDE subject to boundary conditions that ensure the inextensibility constraint. These models are more often than not numerically expensive and thus generally reduced to the planar case. A popular way to circumvent the numerical drawbacks of these continuum mechanics-based models is to use methods based on the shape discretization of the filament into a sequence of rigid parts. In these methods, the elasticity of the filament is approximated using various methods such as discrete Cosserat rod models [Gazzola *et al.* 2018], discrete bead models [Plouraboué *et al.* 2017], or simply by using elastic connectors at each junction between the rigid parts [Alouges *et al.* 2013, Moreau *et al.* 2018].

Let us consider a passive elastic filament of length L and bending stiffness A in a low Reynolds number flow and assume that it is deformed by a waveform of frequency f. The dynamics of the filaments can be shown to be fully characterized by the dimensionless number $S_p = \frac{L}{(k_\perp 2\pi f)^{\frac{1}{4}}}$, called the Sperm Number. S_p encodes the relative importance of the elastic forces compared to the viscous drag. In nature, spermatozoa operate roughly at $S_p = 7$, as measured in [Lowe 2003]. For driven flexible micro-swimmer, adimensional studies using the sperm number can be made

in order to optimize propulsion speed by finding its optimal value for an oscillating actuating, effectively finding the optimal balance between the bending and viscous forces in order to maximize propulsion speed [Lowe 2003, Dreyfus *et al.* 2005].

2.3 3D magnetic micro-swimmer model

2.3.1 Overview

The model swimmer, represented in figure 2.1, is comprised of a spherical head of radius r and a slender flexible tail of length L approximated by an articulated chain formed of N rigid slender rods of length l. Each link can freely rotate with respect to its neighboring links. The orientation of each link in the space relative to the head represents a discrete approximation of the shape of the flexible tail, as done in the planar swimmer models of [Moreau *et al.* 2018, Alouges *et al.* 2013].

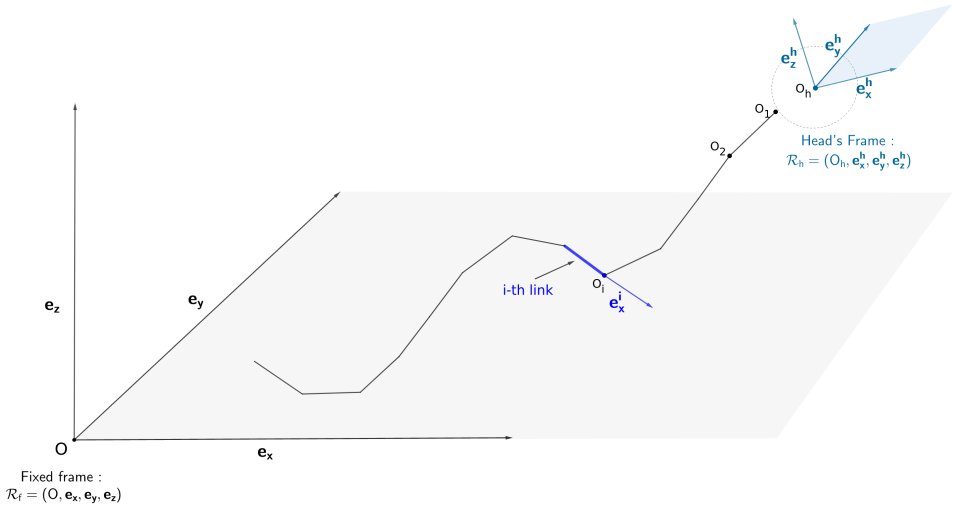

Figure 2.1: 3D swimmer model with N-linked discretization of the tail.The swimmer's head frame is oriented relative to fixed and galilean the reference frame. For each link i, the corresponding local frame $\mathcal{R}_i$ is oriented relative to $\mathcal{R}_h$.

2.3.2 Parametrization and Kinematics of the swimmer

2.3.2.1 Parametrization of the swimmer

We define O_h as the center of the head and O_1 as the point where the first link is attached to the head. We consider a moving frame $\mathcal{R}_{head} = (O_h, \boldsymbol{e_x^h}, \boldsymbol{e_y^h}, \boldsymbol{e_z^h})$ associated to the head of the swimmer, where e_x^h is the unit vector verifying

$$O_1 = O_h - r\, e_x^h\,, \tag{2.7}$$

and e_y^h, e_z^h are arbitrarily chosen to form an orthonormal basis. To this moving frame we associate the matrix $R_{head} \in SO(3)$ defined by

$$R_{head}\, \boldsymbol{e_x} = e_x^h\,, \quad R_{head}\, \boldsymbol{e_y} = e_y^h\,, \quad R_{head}\, \boldsymbol{e_z} = e_z^h. \tag{2.8}$$

This rotation matrix is parametrized by three angles $(\theta_x, \theta_y, \theta_z)$ resulting from a $Z-Y-X$ rotation sequence (Tait–Bryan angles) :

$$R_{head} = R_x(\theta_x) R_y(\theta_y) R_z(\theta_x), \tag{2.9}$$

where R_x, R_y, and R_z are the elementary rotation matrices around the x,y, and z axes, defined for all angle Ψ as :

$$R_x(\Psi) = \begin{pmatrix} 1 & 0 & 0 \\ 0 & \cos(\Psi) & -\sin(\Psi) \\ 0 & \sin(\Psi) & \cos(\Psi) \end{pmatrix},$$
$$R_y(\Psi) = \begin{pmatrix} \cos(\Psi) & 0 & \sin(\Psi) \\ 0 & 1 & 0 \\ -\sin(\Psi) & 0 & cos(\Psi) \end{pmatrix},$$
$$R_z(\Psi) = \begin{pmatrix} \cos(\Psi) & -\sin(\Psi) & 0 \\ \sin(\Psi) & cos(\Psi) & \\ 0 & 0 & 1 \end{pmatrix}.$$

.

This parameterization presents a singularity when $\theta_y = \pi/2$, but in the movements we examine the head does not rotate by more than $\pi/2$.

The orientation of the i^{th} link $(1 \le i \le N)$ is represented by a unit vector e_x^i, so that the i^{th} link is slender segment $[O_i, O_{i+1}]$, where the points $O_1, \ldots, O_{N+1}$, represented on figure 2.1 are defined by 2.7 and

$$O_j = O_h - r\, e_x^h - \ell \sum_{k=1}^{j-1} e_x^k\,, \quad j = 1, \ldots, N\,. \tag{2.10}$$

In order to parameterize these unit vectors by angles that will be "shape variables" (*i.e.* they are constant in a movement where the swimmer does not deform its tail, we need to choose coordinates with respect to the frame attached to the head. Our choice is as follows: $e_x^i = R_i e_x^h$ with R_i a rotation matrix defined by

$$R_i = R_{head} \tilde{R}_i R_{head}^T\,, \tag{2.11}$$

with $R_{head}(\theta_x, \theta_y, \theta_z)$ defined above and

$$\widetilde{R}_i = R_y(\phi_y^i) R_z(\phi_z^i). \tag{2.12}$$

This defines two angles ϕ_y^i, ϕ_z^i such that $(\phi_y^i, \frac{\pi}{2} - \phi_z^i)$ are the classical angles of spherical coordinates (longitude and co-latitude) with respect to the frame $(e_x^h, -e_z^h, e_y^h)$:

$$e_x^i = R_{head}(\theta_x, \theta_y, \theta_z)\, R_y(\phi_y^i)\, R_z(\phi_z^i)\, \boldsymbol{e_x}\,. \tag{2.13}$$

This parameterization is singular for $\phi_y^i = \pm\pi/2$.

With these notations, the swimmer is described by two sets of variables : The 6 *Position variables*: $(\boldsymbol{X}, \boldsymbol{\Theta})$ where

$$\begin{aligned} X &= (x_h, y_h, z_h) \in \mathbb{R}^3 \text{and} \\ \Theta &= (\theta_x, \theta_y, \theta_z) \in [0,\ 2\pi]^3, \end{aligned} \tag{2.14}$$

and the $2N$ *Shape variables*, denoted by

$$\boldsymbol{\Phi} = (\phi_y^1, \phi_z^1, \cdots, \phi_y^N, \phi_z^N). \tag{2.15}$$

2.3.2.2 Angular velocity vectors

For all skew-symmetric matrix $A \in \mathbb{R}^{3\times3}$, we can define a vector $\boldsymbol{\Omega}$ verifying :

$$\forall \boldsymbol{V} \in \mathbb{R}^3\ A\boldsymbol{V} = \boldsymbol{\Omega} \times \boldsymbol{V}. \tag{2.16}$$

Using this property, we define the following angular velocity vectors :

- $\boldsymbol{\Omega}_{head}$ is the vector defining the cross product associated with the skew-symmetric matrix $\dot{R}_{head}R_{head}^T$. $\boldsymbol{\Omega}_{head}$ depends linearly on $(\dot{\theta}_x, \dot{\theta}_y, \dot{\theta}_z)$ as follows:

$$\boldsymbol{\Omega_{head}} = L_{head} \begin{pmatrix} \dot{\theta}_x \\ \dot{\theta}_y \\ \dot{\theta}_z \end{pmatrix}, \tag{2.17}$$

where

$$L_{head} = \begin{pmatrix} 1 & 0 & \sin(\theta_y) \\ 0 & \cos(\theta_x) & -\cos(\theta_y)\sin(\theta_x) \\ 0 & \sin(\theta_x) & \cos(\theta_x)\cos(\theta_y) \end{pmatrix} \begin{pmatrix} \dot{\theta}_x \\ \dot{\theta}_y \\ \dot{\theta}_z \end{pmatrix}. \tag{2.18}$$

- $\boldsymbol{\Omega}_i$ is the vector defining the cross product associated with the skew-symmetric matrix $\dot{\tilde{R}}_i \tilde{R}_i^{\ T}$ for $i \in (1 \cdots N)$. $\boldsymbol{\Omega_i}$ depends linearly on $(\dot{\phi}_y^i, \dot{\phi}_z^i)$ as follows :

$$\boldsymbol{\Omega_i} = L_i \begin{pmatrix} dot\phi_y^i \\ \dot{\phi}_z^i \end{pmatrix}, \tag{2.19}$$

where

$$L_i = \begin{pmatrix} \sin(\phi_y^i) & 0 \\ \cos(\phi_y^i) & 0 \\ 0 & 1 \end{pmatrix} \begin{pmatrix} \dot{\phi}_y^i \\ \dot{\phi}_z^i \end{pmatrix}. \tag{2.20}$$

2.3.3 External Forces

2.3.3.1 Hydrodynamic force and torque on the head of the swimmer

We consider a drag force acting on the head of the swimmer that is proportional to its velocity in each direction of the head frame's $\mathcal{R}_{\text{head}}$ and a resistive torque proportional to the angular velocity of the head :

$$\begin{aligned} \boldsymbol{F}^h_{\text{head}} &= -R_{head} \begin{pmatrix} k_{H,\parallel} & 0 & 0 \\ 0 & k_{H,\perp} & 0 \\ 0 & 0 & k_{H,\perp} \end{pmatrix} R^T_{head} \dot{\boldsymbol{X}} \,, \\ \boldsymbol{T}^h_{\text{head}} &= -k_R \boldsymbol{\Omega}_{head} = -k_R L_{head} \dot{\boldsymbol{\Theta}}, \end{aligned} \tag{2.21}$$

where $k_{H,\parallel}$ and $k_{H,\perp}$ are the parallel and perpendicular hydrodynamic coefficients of the head and k_R is a rotational drag coefficient.

2.3.3.2 Expression of the hydrodynamic force density on a point of the tail of the swimmer

For $i = (1, \cdots, N)$, we consider a point $\boldsymbol{x_i}(s)$ on the i-th link of the tail parametrized by its arclength s such as

$$\boldsymbol{x_i}(s) = \boldsymbol{O_i} - s\boldsymbol{e^i_x}. \tag{2.22}$$

Using the rotation matrices defined in the previous paragraph, $\boldsymbol{x}_i(s)$ is written as :

$$\boldsymbol{x}_i(s) = \boldsymbol{O_H} - rR_{head}\boldsymbol{e_x} - l\sum_{k=1}^{i-1} R_{head}\tilde{R}_k\boldsymbol{e_x} - sR_{head}\tilde{R}_i\boldsymbol{e_x}\,, \tag{2.23}$$

where r is the distance between $\boldsymbol{O_H}$ and $\boldsymbol{O_i}$. We differentiate the previous equation to obtain the expression of the velocity of $\boldsymbol{x_i}(s)$:

$$\begin{aligned} \dot{\boldsymbol{x}}_i(s) =& \dot{\boldsymbol{X}} - r\dot{R}_{head}\boldsymbol{e_x} - l\sum_{k=1}^{i-1} \dot{R}_{head}\tilde{R}_k\boldsymbol{e_x} \\ & - l\sum_{k=1}^{i-1} R_{head}\dot{\tilde{R}}_k\boldsymbol{e_x} - s\dot{R}_{head}\tilde{R}_i\boldsymbol{e_x} - sR_{head}\dot{\tilde{R}}_i\boldsymbol{e_x}. \end{aligned} \tag{2.24}$$

Following Resistive Force Theory, the density of hydrodynamic force $\boldsymbol{f_i}$ is linear with respect to the components of $\dot{\boldsymbol{x}}_i(s)$:

$$\begin{aligned} \boldsymbol{f}_i(s) =& -k_\parallel(\dot{\boldsymbol{x}}_i(s).\boldsymbol{e^i_x})\boldsymbol{e^i_x} - k_\perp(\dot{\boldsymbol{x}}_i(s).\boldsymbol{e^i_y})\boldsymbol{e^i_y} \\ & - k_\perp(\dot{\boldsymbol{x}}_i(s).\boldsymbol{e^i_z})\boldsymbol{e^i_z} \\ =& S_i\dot{\boldsymbol{x}}_i(s)\,, \end{aligned} \tag{2.25}$$

where $k_\parallel$ and $k_\perp$ are respectively the parallel and perpendicular drag coefficients of the swimmer's tail and, for each link i :

$$S_i = (R_{head}\tilde{R}_i)D(R_{head}\tilde{R}_i)^T, \tag{2.26}$$

where

$$D = -\begin{pmatrix} k_{\parallel} & 0 & 0 \\ 0 & k_{\perp} & 0 \\ 0 & 0 & k_{\perp} \end{pmatrix} \tag{2.27}$$

Using the expression of $\dot{\boldsymbol{x}}_{\boldsymbol{i}}(s)$ (equation (2.24)) in equation (2.25), the hydrodynamic force density reads:

$$\begin{aligned} \boldsymbol{f_i}(s) =& S_i \dot{\boldsymbol{X}} - r(R_{head}\tilde{R}_i D \tilde{R}_i^T) R_{head}^T \dot{R}_{head} \boldsymbol{e_x} \\ & - l(R_{head}\tilde{R}_i D \tilde{R}_i^T) \sum_{k=1}^{i-1} R_{head}^T \dot{R}_{head} \tilde{R}_k \boldsymbol{e_x} \\ & - l(R_{head}\tilde{R}_i D \tilde{R}_i^T) \sum_{k=1}^{i-1} \tilde{R}_k \tilde{R}_k^T \dot{\tilde{R}}_k \boldsymbol{e_x} \\ & - s(R_{head}\tilde{R}_i D \tilde{R}_i^T) R_{head}^T \dot{R}_{head} \tilde{R}_i \boldsymbol{e_x} \\ & - s(R_{head}\tilde{R}_i D \tilde{R}_i^T) \dot{\tilde{R}}_i \boldsymbol{e_x}. \end{aligned} \tag{2.28}$$

Using the definition of the angular velocity vectors (equations 2.17 and 2.19), we rewrite the expression above as :

$$\begin{aligned} \boldsymbol{f_i}(s) =& S_i \dot{\boldsymbol{X}} - r(R_{head}\tilde{R}_i D \tilde{R}_i^T) \boldsymbol{\Omega_{head}} \times \boldsymbol{e_x} \\ & - l(R_{head}\tilde{R}_i D \tilde{R}_i^T) \sum_{k=1}^{i-1} \boldsymbol{\Omega_{head}} \times (\tilde{R}_k \boldsymbol{e_x}) \\ & - l(R_{head}\tilde{R}_i D \tilde{R}_i^T) \sum_{k=1}^{i-1} \tilde{R}_k \boldsymbol{\Omega_k} \times \boldsymbol{e_x} \\ & - s(R_{head}\tilde{R}_i D \tilde{R}_i^T) \boldsymbol{\Omega_{head}} \times (\tilde{R}_i \boldsymbol{e_x}) \\ & - s(R_{head}\tilde{R}_i D) \boldsymbol{\Omega_i} \times \boldsymbol{e_x}. \end{aligned} \tag{2.29}$$

In order to write cross products in matrix form, we introduce the following notation :

$$\forall \boldsymbol{V} = \begin{pmatrix} V_1 & V_2 & V_3 \end{pmatrix}^T \in \mathbb{R}^3 \quad [V]^{\times} = \begin{pmatrix} 0 & -V_3 & V_2 \\ V_3 & 0 & -V_1 \\ -V_2 & V_1 & 0 \end{pmatrix}. \tag{2.30}$$

Using this notation and the linear dependency of $\boldsymbol{\Omega_{head}}$ and $\boldsymbol{\Omega_i}$ on the angular velocities (equations 2.17 and 2.19), the hydrodynamic drag force density on link i is written as a linear function of $\dot{\boldsymbol{X}}$, $\dot{\boldsymbol{\Omega}}$, and $\dot{\boldsymbol{\Phi}}$:

$$\boldsymbol{f_i}(s) = A^i(s) \begin{pmatrix} \dot{\boldsymbol{X}} \\ \dot{\boldsymbol{\Theta}} \\ \dot{\boldsymbol{\Phi}} \end{pmatrix}, \tag{2.31}$$

where $A^i(s) \in \mathbb{R}^{3,2N+6}$ is defined block-wise as :

$$A^i(s) = \begin{pmatrix} A^i_{\boldsymbol{X}} \in \mathbb{R}^{3\times 3} \\ A^i_{\boldsymbol{\theta}} \in \mathbb{R}^{3\times 3} \\ A^i_1 \in \mathbb{R}^{2\times 3} \\ \vdots \\ A^i_N \in \mathbb{R}^{2\times 3} \end{pmatrix}, \tag{2.32}$$

where

$$\begin{cases} A^i_{\boldsymbol{X}}(s) = S_i\,, \\ A^i_{\boldsymbol{\theta}}(s) = (R_{head}\tilde{R}_i D\tilde{R}_i^T)[r\boldsymbol{e_x} + l\sum_{k=1}^{i-1}\tilde{R}_k\boldsymbol{e_x}]^\times L_{head} \\ \qquad\qquad + (R_{head}\tilde{R}_i D\tilde{R}_i^T)[s\tilde{R}_i\boldsymbol{e_x}]^\times L_{head}\,, \\ A^i_1(s) = l(R_{head}\tilde{R}_i D\tilde{R}_i^t)\tilde{R}_1[\boldsymbol{e_x}]^\times L_1\,, \\ \qquad\vdots \\ A^i_{i-1}(s) = l(R_{head}\tilde{R}_i D\tilde{R}_i^t)\tilde{R}_{i-1}[\boldsymbol{e_x}]^\times L_{i-1}\,, \\ A^i_i(s) = s(R_{head}\tilde{R}_i D)[\boldsymbol{e_x}]^\times L_i\,, \\ A^i_j = 0_3 \quad \forall j > i \quad . \end{cases} \tag{2.33}$$

2.3.3.3 Hydrodynamic forces and torques on each link

We define the two $3 \times (2N+6)$ matrices B^i and C^i as follows :

$$\begin{cases} B^i = \int_0^l A^i(s)ds\,, \\ C^i = \int_0^l sA^i(s)ds. \end{cases} \tag{2.34}$$

Using this notation, the hydrodynamic force on link i depends linearly on the position and shape velocities as follows :

$$\boldsymbol{F^h_i} = B^i \begin{pmatrix} \dot{\boldsymbol{X}} \\ \dot{\boldsymbol{\Theta}} \\ \dot{\boldsymbol{\Phi}} \end{pmatrix}. \tag{2.35}$$

The hydrodynamic torque on link i calculated about the point O_H is computed from the hydrodynamic force density as follows :

$$\boldsymbol{T^h_{i,H}} = \int_0^l (\boldsymbol{x_i(s)} - \boldsymbol{O_H}) \times \boldsymbol{f_i}(s)ds. \tag{2.36}$$

We rewrite $(\boldsymbol{x_i(s)} - \boldsymbol{O_H})$ as :

$$\begin{aligned} (\boldsymbol{x_i(s)} - \boldsymbol{O_H}) = &- rR_{head}\boldsymbol{e_x} - \sum_{k=1}^{i-1} lR_{head}\tilde{R}_k\boldsymbol{e_x} \\ &- sR_{head}\tilde{R}_i\boldsymbol{e_x}. \end{aligned} \tag{2.37}$$

$\boldsymbol{T^h_{i,H}}$ is then expressed as :

$$\begin{aligned}\boldsymbol{T^h_{i,H}} = &- [rR_{head}\boldsymbol{e_x} + \sum_{k=1}^{i-1} lR_{head}\tilde{R}_k\boldsymbol{e_x}]^\times \int_0^l \boldsymbol{f_i}(s)ds \\ &- [R_{head}\tilde{R}_i]^\times \int_0^l s\boldsymbol{f_i}(s)ds.\end{aligned} \tag{2.38}$$

Thus, the matricial form of $\boldsymbol{T^h_{i,H}}$ is :

$$\begin{aligned}\boldsymbol{T^h_{i,H}} = &- ([rR_{head}\boldsymbol{e_x} + \sum_{k=1}^{i-1} lR_{head}\tilde{R}_k\boldsymbol{e_x}]^\times B^i) \begin{pmatrix}\dot{\boldsymbol{X}}\\ \dot{\boldsymbol{\Theta}}\\ \dot{\boldsymbol{\Phi}}\end{pmatrix} \\ &- ([R_{head}\tilde{R}_i]^\times C^i) \begin{pmatrix}\dot{\boldsymbol{X}}\\ \dot{\boldsymbol{\Theta}}\\ \dot{\boldsymbol{\Phi}}\end{pmatrix}.\end{aligned} \tag{2.39}$$

Similarly, for $k = (i, \cdots, N)$, the hydrodynamic torque on link i about O_k reads:

$$\boldsymbol{T^h_{i,j}} = -(\sum_{k=j}^{i-1}[lR_{head}\tilde{R}_k\boldsymbol{e_x}]^\times B^i - [R_{head}\tilde{R}_i]^\times C^i) \begin{pmatrix}\dot{\boldsymbol{X}}\\ \dot{\boldsymbol{\Theta}}\\ \dot{\boldsymbol{\Phi}}\end{pmatrix}. \tag{2.40}$$

2.3.4 Equations of motion

2.3.4.1 Self-propelled filament

We first consider that there are no external effects on the swimmer. The balance of forces and torques applied on the swimmer gives the following system of 6 equations:

$$\begin{cases} \boldsymbol{F^h_{head}} + \sum_{i=1}^{N} \boldsymbol{F^h_i} = 0\,, \\ \boldsymbol{T^h_{head}} + \sum_{i=1}^{N} \boldsymbol{T^h_{i,H}} = 0. \end{cases} \tag{2.41}$$

Using equations 2.21,2.35, and 2.39, the previous system can be rewritten matricially as :

$$M_1^h \begin{pmatrix}\dot{\boldsymbol{X}}\\ \dot{\boldsymbol{\Theta}}\\ \dot{\boldsymbol{\Phi}}\end{pmatrix} = 0\,, \tag{2.42}$$

where $M_1^h \in \boldsymbol{R}^{6\times 2N+6}$ is defined as :

$$\begin{cases} M_1^h(1\cdots3, 1\cdots2N+6) = -\left(R_{head}D_H R_{head}^T\ O_3\ O_{3,2\times N}\right) + \sum_{i=1}^{N} B^i, \\ M_1^h(4\cdots6, 1\cdots2N+6) = -k_R\left(O_3\ L_{head}\ O_{3,3\times N}\right) - \sum_{i=1}^{N}([rR_{head}\boldsymbol{e_x} + \sum_{k=1}^{i-1} lR_{head}\tilde{R}_k\boldsymbol{e_x}]^{\times}B^i) \\ \qquad\qquad - \sum_{i=1}^{N}[R_{head}\tilde{R}_i]^{\times}C^i. \end{cases} \tag{2.43}$$

. The resolution of equation 2.42 is sufficient to describe the dynamics of a self-propelled swimmer when the deformations of its tail are prescribed as a function of the time. As a consequence, the swimmer's displacements are characterized by the deformations undergone by its tail. The matrix $M_1^h(\boldsymbol{\Theta}, \boldsymbol{\Phi}) \in \mathbb{R}^{6\times2N+6}$ can be subdivided into two sub-matrices $M_{\boldsymbol{X},\boldsymbol{\Theta}}(\boldsymbol{\Theta}, \boldsymbol{\Phi}) \in \mathbb{R}^{6\times6}$ and $M_{\boldsymbol{\Phi}}(\boldsymbol{\Theta}, \boldsymbol{\Phi}) \in \mathbb{R}^{6\times2N}$ such as

$$M_1^h(\boldsymbol{\Theta}, \boldsymbol{\Phi}) = (M_{\boldsymbol{X},\boldsymbol{\Theta}}(\boldsymbol{\Theta}, \boldsymbol{\Phi})|M_{\boldsymbol{\Phi}}(\boldsymbol{\Theta}, \boldsymbol{\Phi})). \tag{2.44}$$

Using these sub-matrices in equation 2.42, and assuming that the values of $\dot{\boldsymbol{\Phi}}(t)$ are prescribed, the position and orientation of a self-propelled swimmer can be obtained from the deformations of its tails by solving the following differential system:

$$\begin{pmatrix} \dot{\boldsymbol{X}} \\ \dot{\boldsymbol{\Theta}} \end{pmatrix} = M_{\boldsymbol{X},\boldsymbol{\Theta}}^{-1}(\boldsymbol{\Theta}, \boldsymbol{\Phi}) M_{\boldsymbol{\Phi}}(\boldsymbol{\Theta}, \boldsymbol{\Phi})\dot{\boldsymbol{\Phi}}. \tag{2.45}$$

2.3.4.2 Magnetic swimmer

Denoting by $\boldsymbol{M}$ the magnetization vector of the head and considering an external homogeneous actuating field $\boldsymbol{B}(t)$, the following torque is applied to the swimmer:

$$\boldsymbol{T^{mag}} = \boldsymbol{M} \times \boldsymbol{B}(t). \tag{2.46}$$

The elasticity of the tail is discretized by considering a restoring elastic moment $\boldsymbol{T_i^{el}}$ at each joint O_i that tends to align each pair $(i, i+1)$ of adjacent links with each other:

$$\boldsymbol{T_i^{el}} = k_{el}\boldsymbol{e_x^i} \times \boldsymbol{e_x^{i-1}}. \tag{2.47}$$

In the case of the swimmer actuated by a magnetic field, the flexible tail is passive, which entails that the $2N$ shape variables are unknowns. Hence, in addition to the force and torque balance on the swimmer, the internal contributions of the tail are taken into account by adding, for $i = (1, \cdots, N)$, the balance of torque on each subsystem consisting of the chain formed by the links i to N projected onto a perpendicular plane to e_x^i, which leads to $2N$ non-trivial equations.
Let us denote, by Π_i for $i = (1, \cdots, N)$ the projection onto the plane generated by the second and third column of $(R_{head}\tilde{R}_i)^T$.

The dynamics of the magnetic swimmer are described by the following system of $2N+6$ equations :

$$\begin{cases} \boldsymbol{F_{head}^h} + \sum_{i=1}^{N} \boldsymbol{F_i^h} = 0\,, \\ \boldsymbol{T_{head}^h} + \sum_{i=1}^{N} \boldsymbol{T_{i,H}^h} = -\boldsymbol{T^{mag}}\,, \\ \sum_{i=1}^{N} \Pi_i(\boldsymbol{T_{i,1}^h}) = \Pi_i(-\boldsymbol{T_1^{el}})\,, \\ \vdots \\ \Pi_N(\boldsymbol{T_{N,N}^h}) = \Pi_N(-\boldsymbol{T_n^{el}})\,, \end{cases} \tag{2.48}$$

Using the expressions of the hydrodynamic forces and torques in the previous section (equations 2.21,2.35,2.39, and 2.40), the left-hand side of the previous dynamic system is written as a linear function of the state derivatives :

$$\begin{pmatrix} \boldsymbol{F_{head}^h} + \sum_{i=1}^{N} \boldsymbol{F_i^h}\,, \\ \boldsymbol{T_{head}^h} + \sum_{i=1}^{N} \boldsymbol{T_{i,H}^h}\,, \\ \sum_{i=1}^{N} \Pi_i(\boldsymbol{T_{i,1}^h})\,, \\ \vdots \\ \Pi_N(\boldsymbol{T_{N,N}^h})\,, \end{pmatrix} = M_2^h(\boldsymbol{\Theta}, \boldsymbol{\Phi}) \begin{pmatrix} \dot{\boldsymbol{X}} \\ \dot{\boldsymbol{\Theta}} \\ \dot{\boldsymbol{\Phi}} \end{pmatrix}, \tag{2.49}$$

where $M_2^h \in \mathbb{R}^{2N+6 \times 2N+6}$ is defined by blocks as :

$$M_2^h = \begin{pmatrix} M^{\boldsymbol{X}} \in \mathbb{R}^{3 \times 2N+6} \\ M^{\boldsymbol{\Theta}} \in \mathbb{R}^{3 \times 2N+6} \\ M^1 \in \mathbb{R}^{2 \times 2N+6} \\ \vdots \\ M^N \in \mathbb{R}^{2 \times 2N+6} \end{pmatrix}, \tag{2.50}$$

where

$$\begin{cases} M^{\boldsymbol{X}} = -\left(R_{head} D_H R_{head}^T \; 0_3 \; O_{3,2\times N}\right) + \sum_{i=1}^{N} B^i \\ M^{\boldsymbol{\Theta}} = -k_R \left(0_3 \; L_{head} \; O_{3,3\times N}\right) \\ \qquad - \sum_{i=1}^{N} [R_{head}(r\boldsymbol{e_x} + \sum_{k=1}^{i-1} l\tilde{R}_k \boldsymbol{e_x})]^{\times} B^i \\ \qquad - \sum_{i=1}^{N} [R_{head}\tilde{R}_i]^{\times} C^i \\ M^1 = -R_1^* \sum_{i=1}^{N} (\sum_{k=1}^{i-1} [l R_{head}\tilde{R}_k \boldsymbol{e_x}]^{\times} B^i) \\ \qquad - R_1^* \sum_{i=1}^{N} [R_{head}\tilde{R}_i]^{\times} C^i \\ \qquad \vdots \\ M^N = -R_N^* \sum_{k=1}^{N-1} ([l R_{head}\tilde{R}_k \boldsymbol{e_x}]^{\times} B^N) \\ \qquad - R_N^* [R_{head}\tilde{R}_N]^{\times} C^N \,, \end{cases} \tag{2.51}$$

where R_i^* is the 2×3 matrix consisting of the second and third line of $(R_{head}\tilde{R}_i)^T$.

Thus, the dynamics of the flexible low Reynolds swimmer actuated by an external magnetic field are described by the following dynamic system :

$$M_2^h(\boldsymbol{\Theta}, \boldsymbol{\Phi}) \begin{pmatrix} \dot{\boldsymbol{X}} \\ \dot{\boldsymbol{\Theta}} \\ \dot{\boldsymbol{\Phi}} \end{pmatrix} = E(\boldsymbol{X}, \boldsymbol{\Theta}, \boldsymbol{\Phi}, \boldsymbol{B}(t)) \,, \tag{2.52}$$

where E is the right hand side of the system 2.48 :

$$E = \begin{pmatrix} 0_3 \\ -\boldsymbol{M} \times \boldsymbol{B}(t) \\ R_i^*(-k_{el}\boldsymbol{e_x^i} \times \boldsymbol{e_x^{i-1}}) \\ \vdots \\ R_i^*(-k_{el}\boldsymbol{e_x^N} \times \boldsymbol{e_x^{N-1}}) \end{pmatrix} \tag{2.53}$$

2.3.5 Summary of The Modelisation

- The swimmer is described by $2N+6$ position variables, 6 position variables, and $2N$ shape variables.
- The position variables are $\boldsymbol{X}$, the cartesian coordinates of the head of swimmer, and $\boldsymbol{\Theta} = (\theta_i^x, \theta_y^i, \theta_z^i)$, its orientation.
- The shape variables are : $\boldsymbol{\Phi} = (\phi_y^1, \phi_z^1, \cdots, \phi_y^N, \phi_z^N)$
- In the absence of external forces and torques, the dynamics of the swimmer are a linear control system with the position and orientation variables as state variables and the shape derivatives $\dot{\boldsymbol{\Phi}}$ acting as a control :

$$\begin{pmatrix} \dot{\boldsymbol{X}} \\ \dot{\boldsymbol{\Theta}} \end{pmatrix} = M_{\boldsymbol{X},\boldsymbol{\Theta}}^{-1}(\boldsymbol{\Theta}, \boldsymbol{\Phi}) M_{\boldsymbol{\Phi}}(\boldsymbol{\Theta}, \boldsymbol{\Phi}) \dot{\boldsymbol{\Phi}}, \tag{2.54}$$

  where $M_{\boldsymbol{X},\boldsymbol{\Theta}}$ and $M_{\boldsymbol{\Phi}}$ are computed according to equations (2.41) and (2.43).
- For the magnetically actuated swimmer, the dynamics are of the form :

$$M_2^h(\boldsymbol{\Theta}, \boldsymbol{\Phi}) \begin{pmatrix} \dot{\boldsymbol{X}} \\ \dot{\boldsymbol{\Theta}} \\ \dot{\boldsymbol{\Phi}} \end{pmatrix} = E(\boldsymbol{X}, \boldsymbol{\Theta}, \boldsymbol{\Phi}, \boldsymbol{B}(t)), \tag{2.55}$$

  Where $M_2^h(\boldsymbol{\Theta}, \boldsymbol{\Phi})$ is a $(2N+6) \times (2N+6)$ matrix encoding the hydrodynamic effects on the swimmer. This equation can be rewritten as an affine control system with the components of the actuating magnetic field acting as controls :

$$\begin{pmatrix} \dot{\boldsymbol{X}} \\ \dot{\boldsymbol{\Theta}} \\ \dot{\boldsymbol{\Phi}} \end{pmatrix} = \boldsymbol{F_0}(\boldsymbol{\Theta}, \boldsymbol{\Phi}) + \begin{pmatrix} \boldsymbol{B_x}(t) & \boldsymbol{B_y}(t) & \boldsymbol{B_z}(t) \end{pmatrix} \begin{pmatrix} \boldsymbol{F_1}(\boldsymbol{\Theta}, \boldsymbol{\Phi}) \\ \boldsymbol{F_2}(\boldsymbol{\Theta}, \boldsymbol{\Phi}) \\ \boldsymbol{F_3}(\boldsymbol{\Theta}, \boldsymbol{\Phi}) \end{pmatrix}, \tag{2.56}$$

  where the vector fields $F_0, \cdots, F_3$ are functions of the columns of $(M^h)^{-1}$ and of the magnetic and elastic constants that can be explicitly derived from equations (2.50),(2.51),(2.64) and (2.53).

2.3.6 Implementation

The model is implemented in MATLAB using the stiff solver ode15s [Shampine & Reichelt 1997] for the resolution of the differential system (2.64). This solver is a variable-step, variable-order (VSVO) solver based on the numerical differentiation formulas (NDFs) of orders 1 to 5. There is a large difference in computation time between the "default" MATLAB solver ode45, which takes and ode15s even for a small number of links which implies that the dynamic model is stiff. For a number of

links $N < 30$, the computation time for the numerical integration of the model takes less than a minute on a laptop with an i5 processor. There are some numerical issues with the model when the deformations of the tail are too large (around $\pi/2$), which is likely due to the singularities of the chosen parameterization of the rotation matrices. When the amplitude of the deformations is around $\pi/2$, we observe a (numerical) loss of rank of the matrix M^h, which causes the numerical inversion of the matrix to return a NaN value, which causes the numerical integration to fail sometimes (often the solver is able to recover from this error and converge anyways). This ill-conditioning of the matrix for large deformations implies that, in hindsight, another method for the parameterization of the shape of the swimmer should have been used, for example quaternions. Nevertheless, in our application, the deformations of the tail induced by the magnetic field are small enough for the numerical integration to be stable.

2.4 Qualitative Validation of the hydrodynamics

In this section, we qualitatively validate the dynamic model by showing that it can be used to accurately reproduce sperm cells trajectories, so as to benchmark the hydrodynamics of our model and the discretization of the tail. In this light, we compare our simulation results to those of [Jikeli *et al.* 2015].
We consider a sperm cell swimming freely in the 3D space, and we assume that there are no external forces and torques and that the sperm cell self-propels by controlling the curvature and torsion of its flagellum. We consider that the flagellum of the sperm cell undergoes a deformation in the form of a travelling bending wave with a constant torsion. Considering the flagellum as a time-varying parametric curve, this deformation is described by its curvature $\kappa(s,t) = K_0 + B\cos(\omega t - \lambda s)$ where $s \in [0\ L]$ is the arclength and a constant torsion $\tau \geq 0$.
The goal here is to compute the value of the relative angles ϕ_y^i, ϕ_z^i and their time derivative at each joint O_i corresponding to the prescribed curvature and torsion. In our discrete tail model, the curvature of the tail of the micro-swimmer is approximated by a piecewise-constant function, as it can be only evaluated the curvature of the swimmer at the joints O_i, hence, a high number of links is needed to be able to accurately approximate the prescribed curvatures. In the simulations, we take $N = 40$. We consider at each point of the tail parametrised by its arclength s a Frenet frame $(\boldsymbol{T}(s), \boldsymbol{N}(s), \boldsymbol{B}(s))$ and denote in particular by $(\boldsymbol{T_i}, \boldsymbol{N_i}, \boldsymbol{B_i})$ the Serret-Frenet frame at the joints O_i. To compute the shape of the swimmer, We consider that the head of the swimmer is at the origin of the reference frame (i.e. $R_{head} = I_3$). $(\boldsymbol{T_i}, \boldsymbol{N_i}, \boldsymbol{B_i})$ are computed as follows :

$$\begin{cases} \boldsymbol{T_i} &= \boldsymbol{e_x^i} = \boldsymbol{R_i e_x}\,, \\ \boldsymbol{N_i} &= \dfrac{\frac{d\boldsymbol{T_i}}{ds}}{||\frac{d\boldsymbol{T_i}}{ds}||}\,, \\ \boldsymbol{B_i} &= \boldsymbol{T_i} \times \boldsymbol{B_i}. \end{cases} \tag{2.57}$$

where

$$R_i = R_y(\phi_y^i)R_z(\phi_z^i), \tag{2.58}$$

and

$$\begin{aligned} R_y(\phi_y^i) &= \begin{pmatrix} \cos(\phi_y^i) & 0 & \sin(\phi_y^i) \\ 0 & 1 & 0 \\ -\sin(\phi_y^i) & 0 & cos(\phi_y^i) \end{pmatrix}, \\ R_z(\phi_z^i) &= \begin{pmatrix} \cos(\phi_z^i) & -\sin(\phi_z^i) & 0 \\ \sin(\phi_z^i) & cos(\phi_z^i) & \\ 0 & 0 & 1 \end{pmatrix}. \end{aligned} \tag{2.59}$$

The Frenet formulas read as follow :

$$\begin{cases} \dfrac{d\boldsymbol{T_i}}{ds} &= \kappa \boldsymbol{N_i}, \\ \dfrac{d\boldsymbol{N_i}}{ds} &= -\kappa \boldsymbol{T_i} + \tau \boldsymbol{B_i}, \\ \dfrac{d\boldsymbol{B_i}}{ds} &= -\tau \boldsymbol{N_i}. \end{cases} \tag{2.60}$$

From the two previous equations, we derive the differential algebraic equation relating the curvature and torsion of the tail to the first and second derivatives of relative angles with respect to the arclength :

$$\begin{cases} \kappa^2 = \cos(\phi_z^i)^2 (\dfrac{d\phi_y^i}{ds})^2 + (\dfrac{d\phi_z^i}{ds})^2, \\ \tau = \dfrac{\cos(\phi_z^i)(\frac{d\phi_y^i}{ds}\frac{d^2\phi_z^i}{ds^2} - \frac{d\phi_z^i}{ds}\frac{d^2\phi_y^i}{ds^2}) + \sin(\phi_z^i)(\frac{d\phi_y^i}{ds})^2 \frac{d\phi_z^i}{ds}}{\kappa^2} + \sin(\phi_z^i)\dfrac{d\phi_y^i}{ds}. \end{cases} \tag{2.61}$$

We solve the previous equation using the MATLAB implicit differential equation solver ode15i to compute the values of ϕ_y^i and ϕ_z^i and their derivatives for $i \in 1 \cdots N$ for the shape variables corresponding to the prescribed curvatures and torsion.

The trajectories of the head of the swimmer are then simulated by solving the differential equation 2.45.

Figure 2.2 shows the three types of sperm cell trajectories obtained from the solution : For an asymmetric ($K_0 > 0$) and non twisted ($\tau = 0$) waveform, the trajectory of the micro-swimmer is circular and planar (**a**). For twisted waveforms ($\tau > 0$) the non-planar flagellar beating patterns results in trajectories in the 3D space: a symmetric and twisted beat produces a trajectory in the shape of a twisted ribbon (**b**), an asymmetric and twisted beat produces a helical trajectory (**c**). These trajectories are in good agreement with the results presented in Fig 2 of [Jikeli *et al.* 2015].

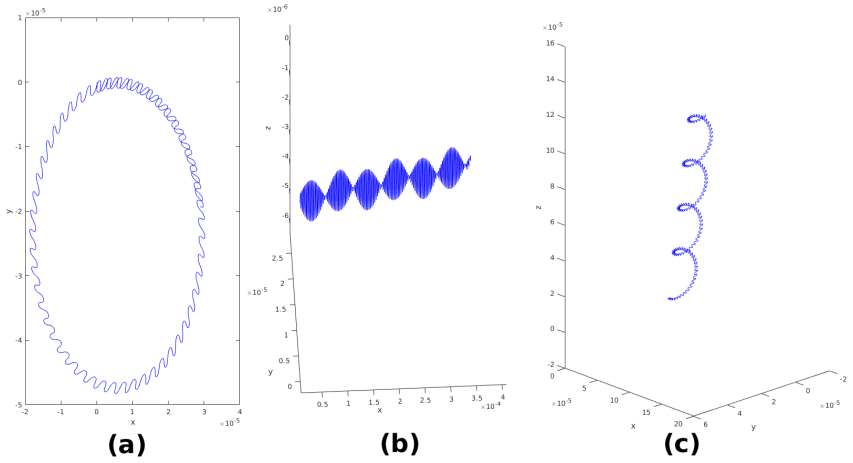

Figure 2.2: Simulated trajectories of the head of our model sperm cell using the parameters and prototypical waveforms of [Jikeli *et al.* 2015], using $N = 40$ links for the tail. (**a**) is the planar circular path generated by the asymmetrical bending wave without torsion (b) the twisted ribbon generated by an asymmetrical bending wave with flagellar torsion, and (c) the helical path generated by a symmetrical bending wave with flagellar torsion.

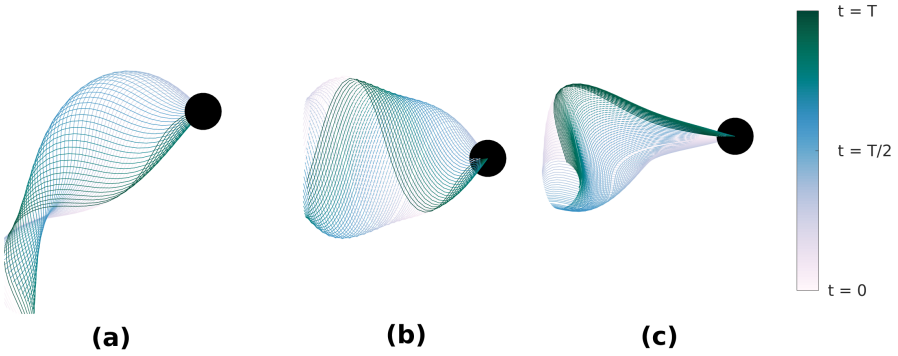

Figure 2.3: (**a**) : planar and asymmetric beating pattern corresponding to the circular trajectory. (**b**): symmetric and twisted beating pattern corresponding to the twisted ribbon trajectory. (**c**) : asymmetric and twisted beating pattern corresponding to the helical trajectory

2.5 Validation of the magnetic micro-swimmer model and parameter fitting

The main goal of this model is to be able to predict the displacement of experimental flexible swimmer under a prescribed magnetic actuation pattern. This section shows

that by fitting the RFT and elastic coefficients of the model in order to match the propulsion characteristics of a given swimmer, mainly its velocity-frequency response curve under sinusoidal actuation, we are able to predict it's horizontal trajectory.

Assuming that the swimming direction is along the x axis, we consider that the actuating magnetic field that takes the following form in the reference frame:

$$\boldsymbol{B}(t) = \begin{pmatrix} B_x & B_y \cos(2\pi f t) & 0 \end{pmatrix}^T , \tag{2.62}$$

.

Typically, flexible micro-swimmers actuated by a magnetic fields of this form have a characteristic velocity-frequency curve where the horizontal swimming speed increases with the actuating frequency until reaching a maximum and slowly decreasing. Example of these velocity-frequency curves can be found in numerous studies such as [Espinosa-Garcia *et al.* 2013, Khalil *et al.* 2014, Yu *et al.* 2006].
The choice for using the velocity-frequency response curve to fit the parameters of the model, as opposed to, say, fitting trajectories is that it is a relatively simple way to guarantee that the elasto-hydrodynamics of the simulated swimmer are close to the experimental one given that the optimal swimming frequency is characterized by the sperm number of the swimmer, which in turn encodes the relative importance of the elastic forces compared to the viscous drag.

The value of dimensions and magnetization of the model swimmers were taken as the same as for the experimental swimmer. Hence, the parameters that need to be identified are the resistive coefficients $(k_{\parallel}, k_{\perp}, k_{H,\parallel}, k_{H,\perp}, k_R)$ and the elasticity coefficient k_{el}. The fitting consists in minimizing the least-squares errors between the experimental and simulated velocity-frequency response curve. Using these parameters as optimization variables without scaling leads to a ill-conditioned optimization problem due to the difference in magnitude between the RFT coefficients and the elasticity constant. Hence, the model is normalized in time, using a time scale equal to $\frac{1}{2\pi f}$, where f is the frequency of the actuating magnetic field, and a length scale equal to L, the length of the tail of the swimmer.

Thus, the state derivatives of the adimensional system are $(\dot{\tilde{\boldsymbol{X}}},\ \dot{\tilde{\boldsymbol{\Theta}}},\ \dot{\tilde{\boldsymbol{\Phi}}})$ defined as :

$$\begin{pmatrix} \dot{\tilde{\boldsymbol{X}}} \\ \dot{\tilde{\boldsymbol{\Theta}}} \\ \dot{\tilde{\boldsymbol{\Phi}}} \end{pmatrix} = \begin{pmatrix} \frac{1}{2\pi f L}\dot{\boldsymbol{X}} \\ \frac{1}{2\pi f}\dot{\boldsymbol{\Theta}} \\ \frac{1}{2\pi f}\dot{\boldsymbol{\Phi}} \end{pmatrix} \tag{2.63}$$

This leads to an adimensionalized model that takes the form :

$$S_p^4 \tilde{M}_2^h \begin{pmatrix} \dot{\tilde{\boldsymbol{X}}} \\ \dot{\tilde{\boldsymbol{\Theta}}} \\ \dot{\tilde{\boldsymbol{\Phi}}} \end{pmatrix} = \tilde{E}(\tilde{\boldsymbol{X}}, \boldsymbol{\Theta}, \boldsymbol{\Phi}) , \tag{2.64}$$

where S_p is the sperm number of the swimmer:

$$S_p = (\frac{L^3 2\pi f k_\perp}{k_{el}})^{1/4}, \tag{2.65}$$

$\tilde{E} = \frac{1}{k_{el}} E$, and the scaled hydrodynamic matrix $\tilde{M_2^h}$ is equal to :

$$\tilde{M_2^h} = \frac{1}{L^3 2\pi f k_\perp} M_2^h. \tag{2.66}$$

Using this formulation, the adimensional parameters that need to be identified are : $(S_p^*, \frac{M}{k_{el}}, \frac{k_\parallel}{k_\perp}, \frac{k_{H,\parallel}}{k_\perp}, \frac{k_{H,\perp}}{k_\perp}, \frac{k_R}{k_\perp})$

Where S_p^* is the sperm number of the swimmer at the optimal frequency for the experimental curve. The parameter fitting was made using a least-squares method implemented in MATLAB, using the built-in solver fmincon for the minimization of the error between the simulated velocity-frequency response curve (using the adimensionalized model) and the experimental curve.

We present the fitting of our model for three different flexible low Reynolds swimmers : the one used in [Oulmas *et al.* 2017] where the same experimental setup was used, using the published velocity-frequency response curve, and two experimental flexible swimmers of different geometries and magnetization strength, where the velocity-frequency response curves were measured experimentally during this thesis. More information on the swimmers and the experimental setup can be found in chapter 4. Figure 2.4 shows the velocity-frequency response curve resulting from the parameter fitting for the swimmer of [Oulmas *et al.* 2017]. Figure 4.4, shows the results for two ISIR flexible swimmers , and a comparison between the observed and simulated horizontal displacements of the swimmer at the optimal frequency. For the three swimmers, the actuating magnetic field used when measuring the velocity-frequency response curves was of the form :

$$\boldsymbol{B}(t) = \begin{pmatrix} B_x & B_y \cos(2\pi f t) & 0 \end{pmatrix}^T, \tag{2.67}$$

, where $B_x = 2.5mT$ and $B_y = 10mT$. The numerical values used for the magnetic field intensities are the same values used in [Oulmas *et al.* 2017] and were chosen in order to have a maximum swimming speed under a sinusoidal field while staying under the limitations of the experimental magnetic generation setup.

For all three swimmers, there is a good agreement between the simulated and observed swimming speed, in particular, we obtain the same value for maximal swimming speed and the corresponding frequency as the ones experimentally measured.

Three links were used for the approximation of the tail. This choice is motivated by the observation that using a finer discretization (more than 3) of the tail only marginally improves the fitting error while adding to the computational cost of the model, as it is shown in figure 2.6, which shows the final least-squares cost (relative l^2-norm) between the experimental velocity-frequency response curve and the simulated velocity-frequency response curve after fitting using an increasing

number of links for the model. As seen in the figure, the model fails to accurately match the experimental velocity-frequency curve with $N = 1$ and $N = 2$ link and results in a small error for $N \geq 3$.

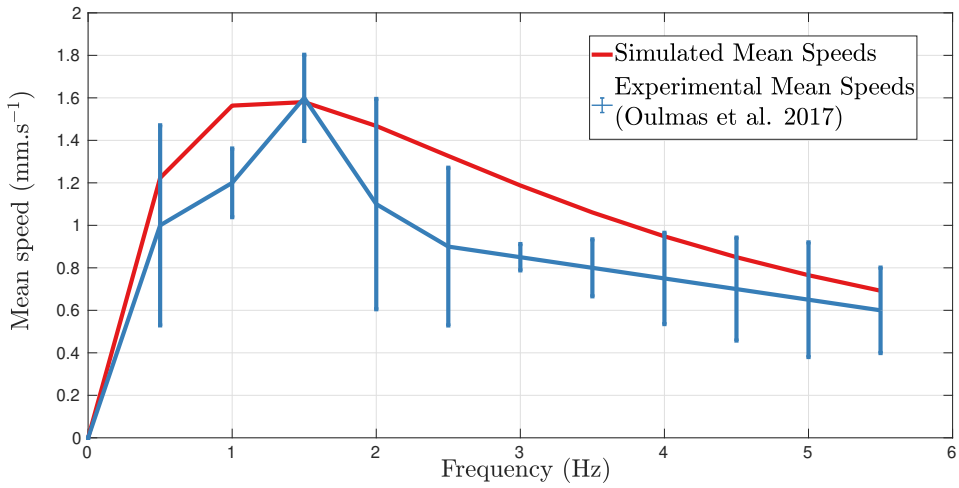

Figure 2.4: Simulated swimming speeds in function of the actuating field frequency compared with the swimming speeds experimentally observed with the swimmer of [Oulmas *et al.* 2017], with the actuating frequency $f \in (0, \cdots, 5.5)$. In particular, both the simulated and experimental swimmers attain the same peak propulsion speed of $1.6mm.s^{-1}$ at a frequency of 1.5 Hz.

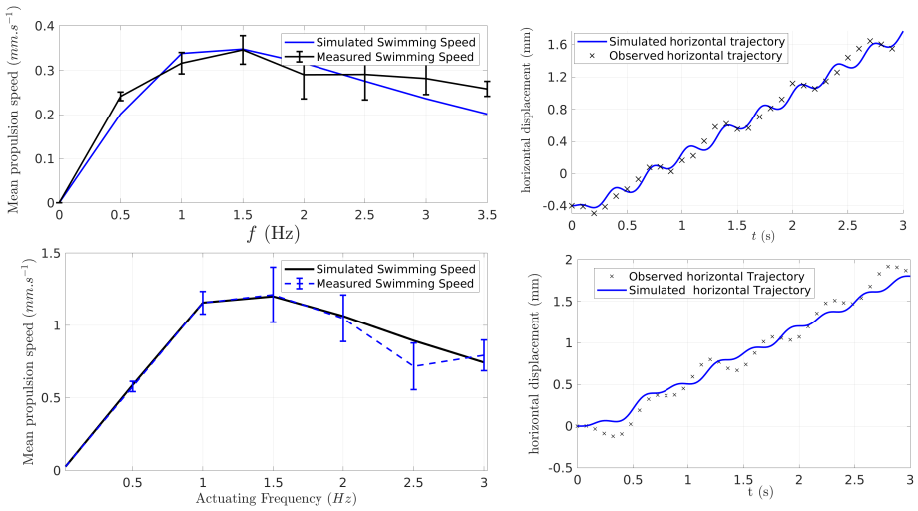

Figure 2.5: Results of the parameter fitting (Right) and comparison between the simulated and observed horizontal trajectories for two ISIR low Reynolds Magnetic swimmer.

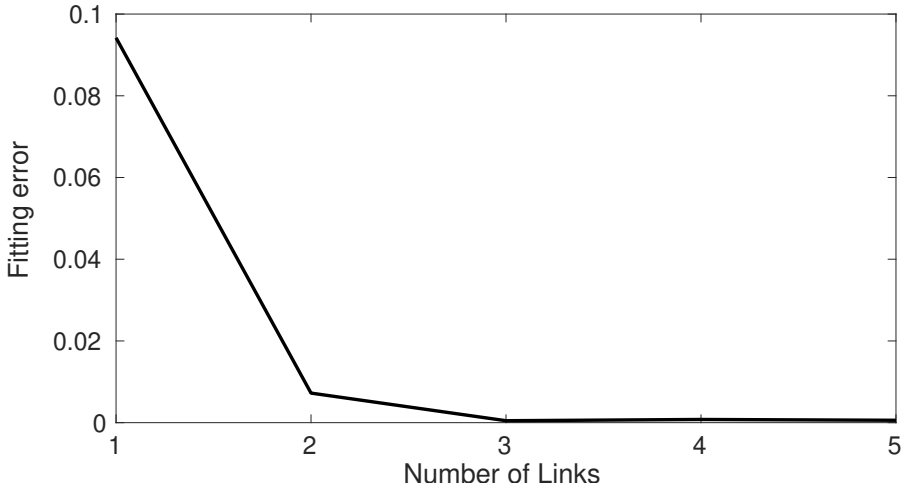

Figure 2.6: Fitting error in function of the number of links of the model.

2.6 Conclusion

We have developed an accurate and computationally inexpensive dynamic model that describes the movement of a flagellar micro-swimmer in 3D and demonstrated that it can be used to predict of the displacements of experimental magnetic low-Reynolds swimmers. Although our main focus in this chapter was the modeling of magnetic micro-swimmers, the model can also be used as a basis for the study of the locomotion of biological flagellated micro-swimmers. The Resistive Force Theory based approximation of the hydrodynamics and the discrete shape approximation used for the geometry of the tail of the swimmer leads to an ODE model that circumvents the numerical drawbacks of continuum mechanics-based models. Moreover, with this formulation, the dynamics of the swimmer can be seen as an ODE control system that is affine in the components of the actuating magnetic field, which makes it suitable to be used as a dynamic constraint for an optimal control problem. The next chapter will be devoted to the optimization of the actuation of the magnetic swimmer using the fitted dynamic model.

CHAPTER 3

Magnetic Field Optimization

Contents

3.1 Introduction

The goal of this chapter is to show that the dynamical model developed in the previous chapter can be used for the optimal control of flexible magnetic low-Reynolds swimmers, and to compute magnetic controls that maximize the horizontal swimming speed of the swimmer.
The study of flexible magnetic micro-swimmers was pioneered by the experimental work of [Dreyfus *et al.* 2005], where the first artificial micrometer-long magnetic swimmer was constructed. In this work, the swimmer was made of a tail consisting of a flexible chain of magnetized beads connected by DNA links which are attached to a red blood cell and actuated by an oscillating magnetic field. This initial work

motivated a series of experimental and theoretical studies on a class of flexible magnetic micro-robots that propel using planar deformations of their shape induced by an oscillating magnetic field [Khalil *et al.* 2014, Jang *et al.* 2015, Gao *et al.* 2010b]. The actuation method that is prevalent for this type of swimmers consists in applying the superposition of a static orientating magnetic field parallel to the desired swimming direction and a perpendicular sinusoidal field that induces a planar symmetric beating of the tail, allowing a displacement along the swimming direction ([Abbott *et al.* 2009]).
The goal of this numerical study is to design actuation schemes that are more efficient than the commonly used sinusoidal actuation. Using optimal control, we maximize locomotion efficiency under constraints on the control that reflect the constraints physically imposed on the magnetic field. We may keep or not the constraint of a fixed component of the magnetic field along the desired displacement direction (static orientating magnetic field), which yields different profiles for the optimal time-varying magnetic field in each case. Both solutions lead (except if planar movement is imposed in the maximization) to non-planar magnetic fields and 3D optimal trajectories. As expected, this optimization process leads to actuating magnetic fields that are more efficient than the currently used sinusoidal one.
As said in section 1.4 of the introduction, most of the optimal control studies on micro-swimmers in the literature were restricted to the self-propelled case, and the optimization studies of magnetically driven micro-swimmers were mostly done under the assumption of a sinusoidal or circular magnetic actuation. Thus, the approach of this work differs from these previous optimization studies of magnetic micro-swimmers as it does not rely on an a priori prescribed magnetic actuation but is based on the resolution of an optimal control problem using the model developed in the previous chapter as a dynamical constraint, which means that the method used in this thesis can be used to provide swimmer-specific optimal actuation for any flexible magnetic swimmer after fitting the dynamical model.
Due to the simplification of the low-Reynolds hydrodynamics and the discrete approximation of the shape of the tail, the dynamics of the swimmer are in ODE form. Hence, the problem of finding the magnetic field that maximizes the horizontal displacement of the swimmer is a finite-dimensional optimal control problem.

Let us recall the expression of the dynamics of the magnetic swimmer from the previous chapter (equation (2.64)) :

$$M^h(\boldsymbol{\Theta}, \boldsymbol{\Phi}) \begin{pmatrix} \dot{\boldsymbol{X}} \\ \dot{\boldsymbol{\Theta}} \\ \dot{\boldsymbol{\Phi}} \end{pmatrix} = \boldsymbol{E}(\boldsymbol{X}, \boldsymbol{\Theta}, \boldsymbol{\Phi}, \boldsymbol{B}(t)) \,, \tag{3.1}$$

where $M^h(\boldsymbol{\Theta}, \boldsymbol{\Phi})$ is a $2N + 6 \times 2N + 6$ matrix. The left-hand side of this equation represents the hydrodynamic effects on the swimmer and the right-hand side $\boldsymbol{E}(\boldsymbol{X}, \boldsymbol{\Theta}, \boldsymbol{\Phi}, \boldsymbol{B}(t))$ is the magnetic and elastic contributions on the swimmer. The previous equation can be rewritten as a control system where the dynamics of the

swimmer are affine with respect to the components of the actuating magnetic field viewed as a control:

$$\begin{pmatrix} \dot{\boldsymbol{X}} \\ \dot{\boldsymbol{\Theta}} \\ \dot{\boldsymbol{\Phi}} \end{pmatrix} = \boldsymbol{F_0}(\boldsymbol{\Theta}, \boldsymbol{\Phi}) + \begin{pmatrix} \boldsymbol{B_x}(t) & \boldsymbol{B_y}(t) & \boldsymbol{B_z}(t) \end{pmatrix} \begin{pmatrix} \boldsymbol{F_1}(\boldsymbol{\Theta}, \boldsymbol{\Phi}) \\ \boldsymbol{F_2}(\boldsymbol{\Theta}, \boldsymbol{\Phi}) \\ \boldsymbol{F_3}(\boldsymbol{\Theta}, \boldsymbol{\Phi}) \end{pmatrix}, \tag{3.2}$$

where the vector fields $F_0, \cdots, F_3$ are functions of the columns of $(M^h)^{-1}$ and of the magnetic and elastic constants. Finding the magnetic field that maximizes the horizontal propulsion of the swimmer over a time interval $[0, tf]$ amounts to solving the following optimal control problem:

$$\begin{cases} \max \ x(t_f)\,, \\ \dot{\boldsymbol{Z}}(t) = f(\boldsymbol{Z(t)}, \boldsymbol{B(t)})\,, \\ \boldsymbol{Z}(0) = 0\,, \\ \boldsymbol{B(t)} \in C_u\,, \\ g(\boldsymbol{Z(tf)}) = 0\,, \end{cases} \tag{3.3}$$

where $\boldsymbol{Z} = \left(\boldsymbol{X}, \boldsymbol{\Theta}, \boldsymbol{\Phi}\right)^T$, $f(\boldsymbol{Z}(t), \boldsymbol{B}(t))$ is the right-hand side of equation (3.2), C_u is the set of constraints on the control, and $g(\boldsymbol{Z}(tf)) = 0$ is the terminal constraints of the state variables. Both constraints will be specified in the latter sections.

This chapter is organized as follow: The first section contains a general presentation of finite-dimensional optimal control problems followed by a review of the numerical methods used in the literature to solving such problems.Following that, we formulate the optimal control problems for the magnetic swimmer. Lastly, we present the numerical optimization results.

3.2 Optimal control of finite dimensional systems

In this section, we present the general formulation for a finite-dimensional optimal control problem and the Pontryagin maximum principle, which gives a first-order local optimality condition. Then we review the common numerical methods used to solve such problems. The first part of this review is based on the reference [Schättler & Ledzewicz 2012]. The numerical part is based on the two review papers [Betts 1998] and [Rao 2009].

3.2.1 General formulation of an optimal control problem

Formally, a control system is defined as a 4-tuple $\Sigma = (M, U, f, \mathcal{U})$ consisting of a state space M, a control set U, the dynamical constraints f, and a class $\mathcal{U}$ of admissible controls. The following assumptions on M,U,f and $\mathcal{U}$ are taken:

1. M is an open and connected subset of $\mathbb{R}^n$.

2. U is a subset of $\mathbb{R}^n$

3. The dynamics $\dot{\boldsymbol{x}} = f(t, \boldsymbol{x}, \boldsymbol{u})$ is defined by a family of time-varying vector fields f parameterized by the control values $u \in U$:

$$\begin{aligned} f : \mathbb{R} \times M \times U \rightarrow & \quad \mathbb{R}^n \\ (t, \boldsymbol{x}, \boldsymbol{u}) \rightarrow & \quad f(t, \boldsymbol{x}, \boldsymbol{u}). \end{aligned} \tag{3.4}$$

4. The class $\mathcal{U}$ of admissible controls is piecewise continuous functions u defined on a compact interval $I \subset \mathbb{R}$ with values in the control set U.

Under these conditions, given a piecewise continuous control $u \in \mathcal{U}$ defined over an open interval J, it follows from local existence and uniqueness results for ordinary differential equations that for any initial condition $x(t_0) = x_0$ for $t_0 \in J$, there exists a unique solution x to the initial value problem :

$$\dot{\boldsymbol{x}} = f(t, \boldsymbol{x}, \boldsymbol{u}(t)) \quad , x(t_0) = x_0 \,, \tag{3.5}$$

defined over some maximal interval $I = (\tau_-, \tau_+) \subset J)$ that contains t_0. The solution $\boldsymbol{x}$ to this initial value problem over I is called the trajectory corresponding to the control $\boldsymbol{u}$, and the pair $(\boldsymbol{x}, \boldsymbol{u})$ is called an admissible controlled trajectory over the interval I.

An optimal control problem consists in finding the admissible controlled trajectory $(\boldsymbol{x}, \boldsymbol{u})$ that minimizes a functional cost $\mathcal{J}$. In the following formulation of an optimal control problem, we also consider a set of boundary constraints N of the form :

$$N = \{(t_0, x(t_0), t_f, x(t_f)) \in \mathbb{R} \times M \times \mathbb{R} \times M : c(t_0, x(t_0), t_f, x(t_f)) = 0\} \,, \tag{3.6}$$

where

$$\begin{aligned} c : \; & \mathbb{R} \times M \times \mathbb{R} \times M \rightarrow \mathbb{R}^p \\ & (t_0, x(t_0), t_f, x(t_f)) \rightarrow (c_1(t_0, x(t_0), t_f, x(t_f)), \cdots, c_p(t_0, x(t_0), t_f, x(t_f))) \,, \end{aligned} \tag{3.7}$$

where $p < 2(n+1)$ and c is a continuously differentiable mapping and the gradients of $(c_1(t_0, x(t_0), t_f, x(t_f)), \cdots, c_p(t_0, x(t_0), t_f, x(t_f)))$ are linearly independent on N.

Under these assumptions, the optimal control problem is written as follows:

$$\begin{cases} \min \mathcal{J} = g(t_f, x(t_f)) + \displaystyle\int_{t_0}^{t_f} f^0(t, x(t), u(t)) dt \,, \\ \dot{\boldsymbol{x}} = f(t, \boldsymbol{x}(t), \boldsymbol{u}(t)) \,, \\ u \in \mathcal{U} \,, \\ t \in [t_0, t_f] \,, \\ x(t_0) = x_0 \,, \\ c(t_0, x(t_0), t_f, x(t_f)) = 0 \,, \end{cases} \tag{3.8}$$

The initial and terminal times t_0, t_f can be fixed or free. The cost function $\mathcal{J}$ is given in the so-called Bolza form as the sum of the integral of a langrangian f^0, which is the running cost of the problem, and a penalty term g, which is the terminal cost of the problem.
The lagrangian

$$\begin{aligned} f^0 : \mathbb{R} \times M \times U &\to \mathbb{R} \\ (t, \boldsymbol{x}, \boldsymbol{u}) &\to f(t, \boldsymbol{x}, \boldsymbol{u}). \end{aligned} \tag{3.9}$$

is continuous in $t, \boldsymbol{x}, \boldsymbol{u}$ and differentiable in x for fixed $(t, u) \in \mathbb{R} \times U$, and the derivative $\frac{\partial f^0}{\partial x}(t, x, u)$ is continuous as a function of all variables.
The terminal cost g is given by a continuously differentiable function,

$$\begin{aligned} g : \mathbb{R} \times M &\to \mathbb{R} \\ (t, \boldsymbol{x}) &\to g(t, \boldsymbol{x}). \end{aligned} \tag{3.10}$$

3.2.2 Pontryagin's Maximum Principle

Pontryagin's maximum principle gives the fundamental necessary conditions for a controlled trajectory (x, u) to be optimal.

The pseudo-hamiltonian function H of the optimal control problem (3.9) is defined as :

$$\begin{aligned} H : \mathbb{R} \times \mathbb{R} \times (\mathbb{R}^n)^* \times \mathbb{R}^n \times \mathbb{R}^m &\to \mathbb{R} \\ H(t, p^0, p, x, u) &= pf(t, x, u) + p^0 f^0 \end{aligned} \tag{3.11}$$

Theorem 1 (Pontryagin's maximum principle) *Let (x_*, u_*) be a controlled trajectory defined over the interval $[t_0, t_f]$ with the control u_* piecewise continuous. If $(x_*, u*)$ is optimal, then there exist a constant $p^0 \leq 0$, an adjoint vector (also called costate vector) $p : [t_0, t_f] \to (\mathbb{R}^n)^*$, and $\lambda \in (\mathbb{R}^p)^*$ such as the following conditions are satisfied :*

1. *Nontriviality of the multipliers : $(p^0, p(t)) \neq 0$ for all $t \in [t_0, t_f]$.*

2. *Adjoint equation : the adjoint variable p is a solution to the time-varying linear differential equation:*

$$\dot{p}(t) = -\frac{\partial H}{\partial x}(t, p^0, p, x, u), \tag{3.12}$$

   where H is the pseudo-hamiltonian associated to the optimal control problem 3.9.

3. *Maximum condition: everywhere in $[t_0, t_f]$ we have :*

$$H(t, p^0, p(t), x_*(t), u_*(t)) = max_{v \in U} H(t, p^0, p(t), x_*(t), v). \tag{3.13}$$

4. *Transversality conditions on the adjoint vector*

$$\begin{aligned} p(t_0) &= -(\lambda \frac{\partial c}{\partial x_0} + p^0 \frac{\partial g}{\partial x_0}), \\ p(t_f) &= (\lambda \frac{\partial c}{\partial x_f} + p^0 \frac{\partial g}{\partial x_f}). \end{aligned} \tag{3.14}$$

5. *Transversality conditions on the pseudo-hamiltonian: If the initial time t_0 is free, there exists an absolutely continuous function $M : [t_0,\ tf] \to \mathbb{R}$ such as*

$$M(t) = H(t, p^0, p(t_0), x_*(t_0), u_*(t_0)), \tag{3.15}$$

   and

$$M(t_0) = (\lambda \frac{\partial c}{\partial t_0} + p^0 \frac{\partial g}{\partial t_0}). \tag{3.16}$$

   Similarly, if the final time t_f is free, there exists an absolutely continuous function $M : [t_0,\ tf] \to \mathbb{R}$ such as

$$M(t) = H(t, p^0, p(t_0), x_*(t_0), u_*(t_0)), \tag{3.17}$$

   and

$$M(t_f) = -(\lambda \frac{\partial c}{\partial t_f} + p^0 \frac{\partial g}{\partial t_f}), \tag{3.18}$$

The controlled trajectories (x_*, u_*) for which there exists multiplier p^0 and p such as the conditions of the maximum principle are satisfied are called *extremals*,

and the tuple (x_*, u_*, p^0, p) is called *extremal lifts*. The extremal lift is *normal* is $p^0 < 0$ and abnormal if $p^0 > 0$. In the normal case, the value of p^0 can be fixed to -1 without loss of generality.

From Pontryagin's maximum principle, the coupled system consisting of the dynamics and the adjoint equation can be written as a Hamiltonian system :

$$\begin{cases} \dot{x}_*(t) = \dfrac{\partial H}{\partial p}(t, p^0, p, x_*, u_*), \\ \dot{p}(t) = -\dfrac{\partial H}{\partial x}(t, p^0, p, x_*, u_*). \end{cases} \tag{3.19}$$

Thus, an extremal lift of an optimal control problem is the solution of a two-point boundary value problem consisting in solving this Hamiltonian system along with the boundary conditions $c(t_0, x_*(t_0), t_f, x_*(t_f)) = 0$ and with the transversality conditions. In summary, solving an optimal control problem requires, in theory, to find all solutions to a boundary value problem on state and the adjoint vector, which is coupled with a maximization condition, and then compare the costs of each extremal. This is very difficult in general for all but the simplest problems.
In what follows, we will review the numerical methods commonly used to solve optimal control problems, or at least to compute extremals of an optimal control problem.

3.2.3 A review on the numerical methods used for the resolution of optimal control problems

Numerical methods for solving optimal control problems are divided into two major classes: indirect methods and direct methods. Indirect methods rely on the numerical resolution of the boundary-value problem resulting from the first-order optimality conditions in order to determine extremals of the problem. Then, the extremal with the lowest cost is chosen from each of the the locally optimizing solutions. On the other hand, direct methods consist in discretizing the optimal control problem into a finite-dimensional nonlinear optimization problem, also called a nonlinear program (NLP) [Kraft 1985], then solving it using well known optimization techniques such as interior-point methods or sequential quadratic programming methods.

3.2.3.1 Indirect Methods

The most basic indirect method is the *shooting method* [Keller 1976]. Starting with an initial guess of the unknown initial boundary conditions at t_0, the Hamiltonian system (3.19) is integrated and the terminal conditions obtained from the numerical integration are compared to the known terminal conditions (the boundary conditions of the problem and the transversality conditions). If the integrated terminal conditions differ from the known terminal conditions by more than a specified tolerance ε, the unknown initial conditions are adjusted and the process is iterated upon until the difference between the integrated terminal conditions and the required terminal conditions is less than ε.

Shooting methods presents significant numerical difficulties due to ill-conditioning of the Hamiltonian dynamics, which leads to the amplification of the errors made in the unknown boundary conditions as the dynamics are integrated over time. This is particularly true when the optimal control is hyper-sensitive, i.e. when the time interval of interest is long in comparison with the time-scales of the Hamiltonian system in a neighborhood of the optimal solution. In order to overcome the drawbacks of simple shooting methods, the *multiple-shooting* method was developed. The multiple shooting method consists in dividing the time interval $[t_0, t_f]$ into $M+1$ sub intervals and then applying the single shooting method over each sub-interval $[t_i, t_{i+1}]$ in order to determine the unknown initial values of the state and adjoint vectors at each end, while enforcing their continuity at the boundary of each sub-interval. Thus, multiple-shooting methods are more numerically stable because the integration is performed over smaller time intervals. Multiple shooting methods are also used in the case where the optimal control is non-smooth, for example where the control is a concatenation of bang arcs and/or singular arcs. In that case, it is worth noting that it is necessary to know the structure of the optimal control in advance in order to apply the multiple-shooting method.
The biggest drawback of indirect simple shooting and multiple shooting methods is their sensitivity to the initial guess of the unknown values of the state and costate. Hence, in most practical cases, it is important to provide an initial estimate that is close enough to the unknown state and co-state values in order to ensure the convergence of the shooting method to the solution of the boundary value problems, for example, by using the approximate values obtained by the resolution of an optimal control problem using a direct method to initialize the shooting [Bonnard & Cots 2014] (direct methods are usually less sensitive to initial guesses than indirect methods), or by using continuation methods [Caillau *et al.* 2012]. The basic idea of continuation methods, also called homotopy methods, is to iteratively solve a sequence of perturbed versions of the original problem that are more numerically tractable (for example by regularizing the control), using the solution of one problem as the initial guess for the following one. Supposing that the original problem requires finding the zero of a shooting function $\boldsymbol{a}$:

$$\boldsymbol{a}(\boldsymbol{x}) = 0\,, \tag{3.20}$$

Continuation methods embed this problem into a family of related problems that depends on a parameter $0 \leq \tau \leq 1$:

$$\tilde{\boldsymbol{a}}(\boldsymbol{x}, \tau) = 0. \tag{3.21}$$

The family of problems $\tilde{\boldsymbol{a}}(\boldsymbol{x}, \tau)$ is chosen such as $\tilde{\boldsymbol{a}}(\boldsymbol{x}, 1)$ is easily solvable and $\tilde{\boldsymbol{a}}(\boldsymbol{x}, 0)$ is equivalent to the original problem, and it is also generally assumed that the solution $\boldsymbol{x}(\tau)$ varies smoothly in function of τ.
Indirect shooting methods have been implemented in the software Hampath [Caillau *et al.* 2010], which also implements homotopy methods.
Another class of algorithms that can be used in order to solve the boundary value

problem is indirect collocation methods, where the state and adjoints are parametrized using piecewise polynomials. The collocation procedure leads to a set of nonlinear equations where the coefficients of the piecewise polynomial are the unknown. The MATLAB-based solver bvp4c [Shampine *et al.* 2000] implements a collocation method for the resolution of boundary value problems and has been used for the resolution of optimal control problems [Wang 2009].
Another drawback of indirect methods is the necessity to have the expressions of the necessary conditions, which implies having the analytical formulations of the derivatives of the dynamics f and of the boundary conditions c. This is obviously a cumbersome task for large, complicated problems. Recently, the approach taken in order to compute these derivatives is based on the use of automatic differentiation tools, such as Tapenade [Hascoet & Pascual 2013] or by using the symbolic package CasADi [Andersson *et al.* 2012]. Still, even with these tools, there is a limitation of the scope of problems that can be solved with indirect method, as there are many cases where the dynamics of the studied system are not explicit enough to be differentiated automatically.

3.2.3.2 Direct Methods

Direct methods rely on the discretization of the state and/or the control of the original optimal control problem. In either case, the optimal control problem is transcribed into a finite dimensional nonlinear programming problem (NLP).

The main advantage of direct methods over indirect method is that they can be applied without explicitly deriving the necessary conditions, and that they do not require a prior knowledge of the structure of the control. One of the simplest direct method for solving optimal control problems is the *direct shooting method*, where the control is parameterized using a specific functional form, for example in the form:

$$u(t) = \Sigma_{i=1}^{m} a_i \psi_i(t), \tag{3.22}$$

where ψ_i, $(i = 1, \cdots, m)$, are known functions and a_i, $(i = 1, \cdots, m)$ are unknown parameters. The direct shooting method consists then in optimizing the function :

$$\begin{aligned} &\mathbb{R}^m \to \mathbb{R} \\ &\boldsymbol{a} = (a_1, \cdots, a_m)^T \to \mathcal{J}_{\boldsymbol{a}}\,, \end{aligned} \tag{3.23}$$

where $\mathcal{J}_{\boldsymbol{a}}$ is the value of the cost function of the optimal control problem evaluated by taking $\boldsymbol{a}$ as a parameter for the control and numerically integrating the dynamics of the system. *Direct multiple shooting methods* are an improvement of this method, where, similarly to the indirect multiple shooting methods, the time interval is divided into several sub-intervals in order to reduce the sensitivity to the initial guess of the unknown parameters by integrating over smaller time intervals. The initial values of the state at the beginning of each sub-interval are taken as unknowns in addition to the control's parameterization. *Direct collocation methods*, as opposed to direct shooting methods, rely on the approximation of both the state and control using piecewise continuous polynomials. The dynamic and state constraints

are imposed only on intermediate points, called collocation points. There are two main types of collocation, local collocation, where the time interval is divided into a sequence of sub-intervals and the state and controls are approximated on each sub-interval by a polynomial of fixed degree, and global collocation, where the state and controls are approximated by global polynomial over the whole time interval. The resolution of an optimal control problem using a direct collocation method requires solving a very large but sparse nonlinear programming problem. Because of the sparsity of the resulting NLP, many of the derivatives of the constraint Jacobian are zero, and thus it is possible to solve such problems efficiently using optimization solvers based on an interior-point algorithm (such as IPOPT [Wächter & Biegler 2006]), or a sequential quadratic programming (SQP) algorithm (such as Worhp [Büskens & Wassel 2013]).

It is worth noting that, informally, the Karush–Kuhn–Tucker (KKT) conditions for the NLP program (first order necessary conditions for optimality) resulting from a direct collocation method can be seen as a "discrete" version of the maximum principle. In some specific cases, it has been shown that the KKT multipliers of the NLP converges to the costate vector of the original optimal control problem [Ross 2005], and that this property can be used to prove the convergence of the direct solutions to an extremal [Ross & Fahroo 2001]. Efficient direct solvers are the open source solvers Bocop [Bonnans *et al.* 2011] and ICLOCS [Falugi *et al.* 2010] and the commercial solver Gpops [Rao *et al.* 2010].

3.2.3.3 Other methods

Most applications use variations of indirect or direct methods for the resolution of optimal control problem. However, there are a few other methods worth citing. For example, there is a class of global methods based on the resolution of the Hamilton-Jacobi-Bellman (HJB) equations [Bellman 1957], which are PDE's that describe the optimal control functions $u_*(x,t)$ as well as the optimal value of the objective for all possible initial conditions. Although these equations are of theoretical importance as one can derive necessary and sufficient optimality conditions from the HJB equations, it is not generally numerically tractable to solve them for all but the simplest optimal control problems. Another class of methods for the resolution of optimal control problem are those based on metaheuristics such as genetic algorithms [Michalewicz *et al.* 1990]. Interest in these methods is motivated by the fact that they can be applied without a detailed understanding of the system being optimized, and using a genetic algorithm can be a solution in the case the function to be optimized is not completely known or given in "black box" form. However, because of the fact that they do not exploit gradient information during the optimization process, they are not computationally competitive with direct and indirect methods.

3.2.4 Numerical method chosen for the resolution of the magnetic field optimization problem

Let us go back to the problem of interest in this chapter, i.e. finding the magnetic field that maximizes the horizontal displacement of the magnetic swimmer, which amounts to solving a finite dimensional optimal control problem with the model developed in the previous chapter as a dynamic constraint. The main drawback of this modelisation is the fact that the dynamics of the swimmer requires the inversion of the hydrodynamic matrix ($M^h(\mathbf{\Theta}, \mathbf{\Phi})$ in equation (3.1)), which makes the dynamics of the swimmer not explicit enough for an analytical study of the problem using Pontryagin's maximum principle or for a resolution based on indirect methods. This is due to the fact that the analytical computation of the state dynamics of the model requires the symbolic inversion of $M^h(\mathbf{\Theta}, \mathbf{\Phi})$ which is computationally prohibitive even for the 1-linked case, where $M^h(\mathbf{\Theta}, \mathbf{\Phi}) \in \mathbb{R}^{(8\times 8)}$. The numerical inversion of the dynamic system is not a good workaround as most indirect solvers require an expression for the hamiltonian system that can be handled by an automatic differentiation routine, which means that a built-in or library routine or an implementation of an algorithm for the system inversion cannot be used. The latter part is due to the fact that implementing a linear system resolution algorithm requires the use of conditional statements (for the pivoting) and loops that depend on the variables which leads to code that cannot be automatically differentiated. For these reasons, we chose to use a direct method for the resolution of the optimal control problems, using the open-source direct optimal control solver ICLOCS ([Falugi *et al.* 2010]), which has the advantage of giving the possibility to estimate the derivatives of the dynamics, cost and constraint functions numerically. The optimal control problems are solved with ICLOCS using a Hermite-Simpson collocation method. The resulting NLP is solved by the interior-point solver IPOPT ([Wächter & Biegler 2006]). It is worth noting that during the optimization, the hessian of the NLP has been approximated using the limited-memory version of the BFGS quasi-Newton updates provided by IPOPT, which speeds up convergence in our case despite needing more iterations to terminate.

3.3 Magnetic Field Optimization

3.4 Optimal control problems formulation

In this chapter, we numerically solve two classes of optimal control problems. The first class of optimal control problems study consist in maximizing the horizontal displacement of the swimmer over a fixed time frame. The solutions of these problems gives a physical limit of the swimming speed that can be achieved with a magnetic field, however, they lead to solutions in 3D that are not periodic and in which there is a small drift of the swimmer from the horizontal path. Therefore, we solve a second class of optimal control problem that is more suitable for experiments with additional periodicity constraints on the shape and orientation of the swimmer. The

aim of this latter formulation is to obtain an optimal actuation pattern that can be indefinitely repeated over time in order to drive the swimmer in experiments.
Four different types of constraints on the actuating magnetic field are considered : firstly, the feasible controls are assumed to be the superposition of static orientating field along the prescribed swimming direction and an orthogonal magnetic field, which leads to a single-input optimal control problem. Secondly, the control is considered to be a two-dimensional magnetic field where both components are time-varying. Lastly, two three-dimensional magnetic fields that leads to out-of-plane optimal trajectories are considered : one with a static orientating component and two orthogonal actuating fields, and one where all three components are free to be optimized.
The aim here is to present different types of optimal actuation patterns that can be adapted to a particular experimental setups. For example, the planar solutions can be used in experimental setups where the degrees of freedom of the magnetic field are limited such as a setup consisting of only two Helmholtz coils. Additionally, orientating fields are important in non-ideal experimental conditions, for instance, when the swimmer is not neutrally buoyant, or in the presence of thermic noise, as they can be used to keep the swimmer from drifting and to compensate its weight.

3.4.1 Swimming speed optimization during a fixed time frame.

Firstly, we focus on finding the actuating magnetic field $B = \begin{pmatrix} B_x(t) \\ B_y(t) \\ B_z(t) \end{pmatrix}$ that maximizes the horizontal displacement of the swimmer at a fixed time t_f. Denoting by $\boldsymbol{Z(t)}$ the state vector $\begin{pmatrix} \boldsymbol{X}(t) \\ \boldsymbol{\Theta}(t) \\ \boldsymbol{\Phi}(t) \end{pmatrix}$ and rewriting equation (3.1) as $\dot{\boldsymbol{Z}}(\boldsymbol{t}) = f(\boldsymbol{Z(t)}, \boldsymbol{B(t)})$, this optimal control problem is written as :

$$\begin{cases} \max x(t_f) \\ \dot{\boldsymbol{Z}}(\boldsymbol{t}) = f(\boldsymbol{Z(t)}, \boldsymbol{B(t)}) \\ \boldsymbol{Z}(0) = 0 \\ \boldsymbol{B(t)} \in C_i \end{cases}, \tag{3.24}$$

where C is the set of constraints on the magnetic field and tf is the final time. We investigate four optimal control problems depending on the types of constraints on the actuating magnetic field, taking in each case the same bounds on the magnetic field intensities.

1. In the first optimal control problem (OCP-1), we consider the admissible controls as the superposition of a static orientating field along the x axis and a time-varying field along the y axis :

$$C_1 = \{\boldsymbol{B}(t),\ B_x(t) = B_x, |B_y| \leq B_0, B_z(t) = 0\}$$

2. In the second optimal control problem (OCP-2), both the x and y components of the magnetic field are time-varying.

$$C_2 = \{\boldsymbol{B}(t),\ B_z(t) = 0, ||(B_x(t), B_y(t))|| \leq B_0\}$$

3. In the third problem (OCP-3), we consider the admissible controls to be the superposition of a static orientating field along the x axis and a time-varying actuating field in the $y - z$ plane.

$$C_3 = \{\boldsymbol{B}(t),\ B_x = B_x\ ||(B_z(t), B_y(t))|| \leq B_0\}$$

4. In the last optimal control problem (OCP-4), we consider the general case where all components of the magnetic field are time-varying.

$$C_4 = \{\boldsymbol{B}(t),\ ||(B_x(t), B_z(t), B_y(t))|| \leq 10mT\}$$

3.4.2 Swimming speed optimization under the constraint of a periodic deformations

We also address the previous optimal control problems with additional periodicity constraints on the shape of the tail of the swimmer, its orientation, and its position in the y and z axes. The aim here is to obtain a magnetic field pattern that can be indefinitely repeated over time in order to induce a net horizontal displacement of the swimmer, which makes this formulation more suited for experimental settings.

This optimal control problem is formulated by adding periodicity constraints on the orientation and shape variables of the swimmer $\boldsymbol{\Theta}$ and $\boldsymbol{\Phi}$ and on the position of the swimmer on the y and z axis. Thus, the period swimming optimal control problems $(POCP - i)$ are written as :

$$\begin{cases} \max x(T) \\ \dot{\boldsymbol{Z}}(\boldsymbol{t}) = f(\boldsymbol{Z}(\boldsymbol{t}), \boldsymbol{B}(\boldsymbol{t})), \\ \boldsymbol{Z}(0) = 0, \\ \boldsymbol{B}(\boldsymbol{t}) \in C_i, \\ (y(T), z(T)) = (0, 0), \\ \boldsymbol{\Theta}(T) = O, \\ \boldsymbol{\Phi}(T) = O. \end{cases} \tag{3.25}$$

.

We keep the same set of constraints on the magnetic field amplitudes C_i as the previous section.

3.5 Numerical Resolution Method

3.6 Numerical Results

In this section, the results of the numerical solutions of the optimal control problems are presented. The bounds on the magnetic field are fixed as : $B_x = 2.5mT$ and

$B_0 = 10mT$, same as the values for the magnetic field that were used for the fitting of the model in the previous chapter in order to have a "fair" comparison with the sinusoidal field.

For the first class of optimal control problems, the final time is fixed at $tf = 3$. For the optimal control problems with a periodicity constraint, the final time is chosen is chosen to be the same as the observed optimal period for a sinusoidal actuation ($1.5Hz$ frequency).

3.6.1 First Class of Optimal Control Problems

Fig. 3.1 shows the displacement of the swimmer under each optimal solution, and under the sinusoidal field at the optimal frequency (1.5 Hz). From this, we can see that non-planar solutions largely out-performs planar solutions, and that the solutions where all components are free to be optimized are significantly more efficient than the solutions where the x-component is fixed. This also indicates that, in order to maximize swimming speed, two common experimental practices must be avoided : Firstly, the common sinusoidal actuation method is sub-optimal and is largely out-performed by the solutions. Secondly, the use of a static orientating field in the swimming direction limits the speed of the swimmer, and that allowing the x-component of the magnetic field to be varying leads to a more efficient actuation pattern. In the second case, steering the swimmer along a new direction can be achieved by rotating the actuating magnetic field. However, in non-ideal experimental conditions, for instance, when the swimmer is not neutrally buoyant, or in the presence of thermic noise, using a static field to keep the swimmer on track and/or to compensate the weight of the swimmer may be more robust.

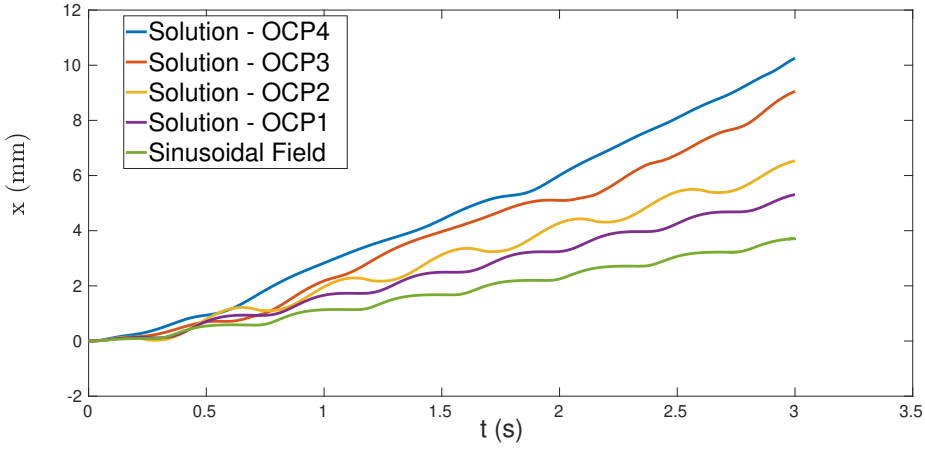

Figure 3.1: Comparison of x-displacements associated with the solutions of OCP1-4 and with the sinusoidal actuation

3.6.1.1 Planar Solutions

For OCP-1 and OCP-2, the dimension of the dynamic system reduces to N+3 because of the fact that the constraints on the controls leads to a planar trajectory in the $x-y$ plane. The numerical solution for OCP-1 takes the form of a sequence of Bang arcs, as seen in Fig. (3.2, $(\boldsymbol{a})$) whereas the solution of OCP2 is continuous ($(\boldsymbol{b}), (\boldsymbol{c})$). In both cases, the optimal actuation patterns lead to a trajectory where swimmer oscillates around the x axis while moving in the x-direction (see Fig. 3.3). The shape of both optimal trajectories is similar to the trajectory of the swimmer under the sinusoidal field. Interestingly enough, the optimal magnetic fields are periodic in both cases, and induce a periodic deformation of the swimmer, as seen in Fig. 3.4. Both solutions out-perform the reference sinusoidal actuation in terms of horizontal speed. In practice, the solution of OCP-1 shows that having an orthogonal actuating field (in addition to the static orientating field) in the form of a square signal is more efficient than an actuating sinusoidal field. The solution of the second planar problem (OCP-2) shows that orientating fields are not necessary for straight swimming and that actuating a flagellar magnetic swimmer with two time-varying components leads to a substantial increase in swimming speed.

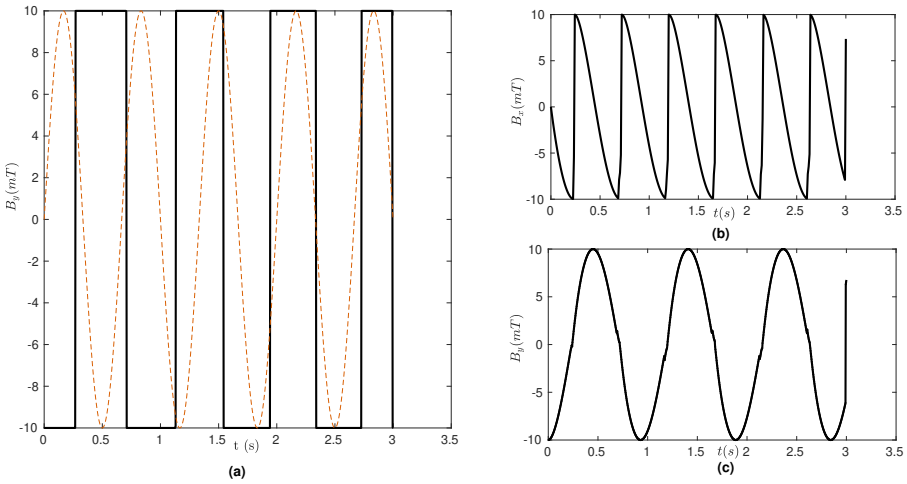

Figure 3.2: Solution of the planar optimal control problems. $(\boldsymbol{a})$: y-component of the solution of OCP-1 compared with the sinusoidal field at optimal frequency $(1.5Hz)$. $(\boldsymbol{b})$: x-component of the solution of OCP-2. $(\boldsymbol{c})$: y-component of the solution of OCP-3.

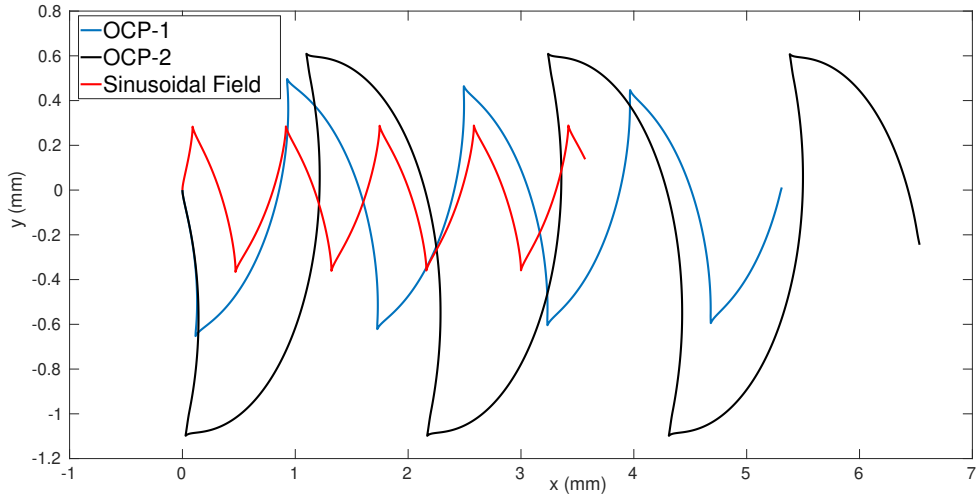

Figure 3.3: Optimal planar trajectories associated with OCP-1 and OCP-2 compared with the trajectory of the swimmer actuated by the sinusoidal field.

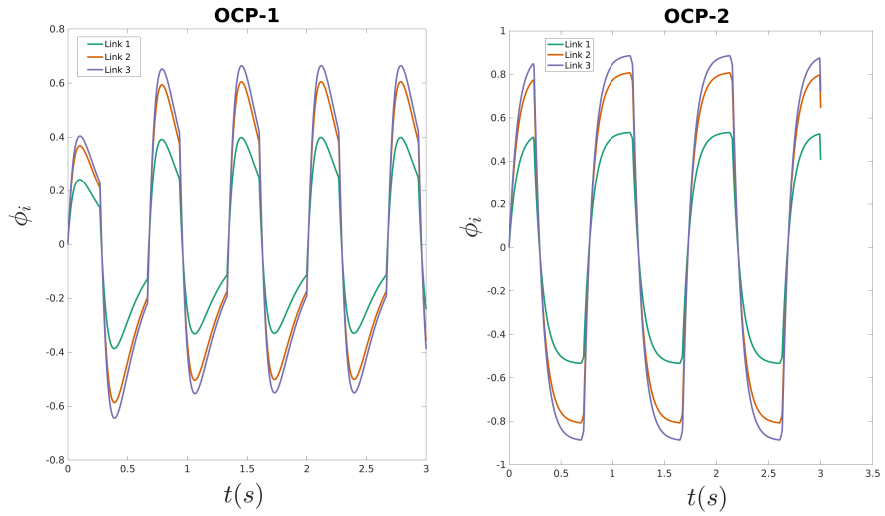

Figure 3.4: Shape angles of the swimmer for the solutions of both planar problems OCP-1 and OCP-2.

3.6.1.2 Non-planar solutions

The non-planar optimal magnetic fields solutions of OCP3 and OCP4 leads to trajectories, shown in Fig. 3.6, where the swimmer revolves around the horizontal axis in an helical trajectory. As seen in Fig. 3.1, the non-planar actuation patterns largely out-performs the planar ones, which shows the necessity of allowing flagellar

swimmers to go out-of-plane in order to swim at a maximal propulsion speed. Similarly to the planar case, the optimal solution is periodic apart from transient states near the initial and final times (see Fig. 3.5) and induce a periodic 3D deformation of the tail of the swimmers, as shown in the phase planes of Fig. 3.7. Although being the best performing magnetic fields overall, the solutions of OCP-3 and OCP-4 have the drawback to lead to trajectories with a non-zero net displacement on the y and z, axis, i.e. the helical trajectory of the swimmer generated by these fields drifts from the horizontal direction, which is inconvenient for experimental purposes. This problem can be overcome by using stronger orientating fields (although at a loss of speed) in the case of OCP3,by adding path constraints in the optimal control problem, or by using periodicity constraints as it is done in the next section.

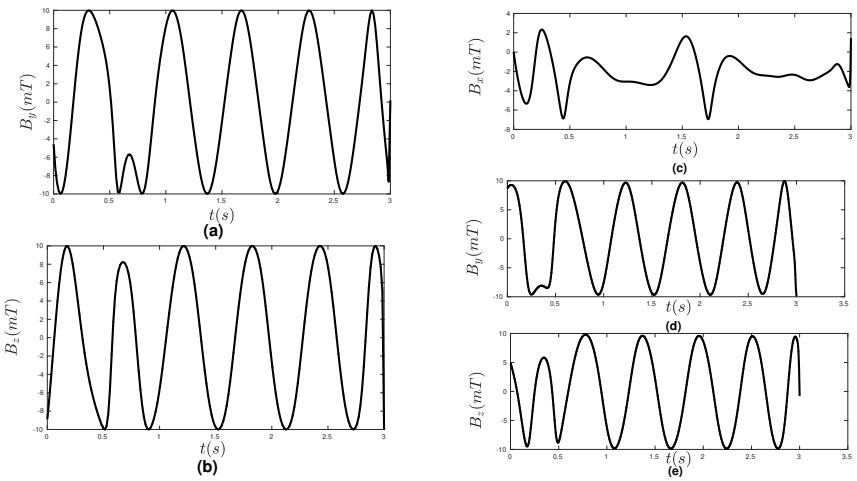

Figure 3.5: Solution of the non-planar optimal control problems. $(\boldsymbol{a})$: y-component of the solution of OCP-3. $(\boldsymbol{b})$: z-component of the solution of OCP-2. $(\boldsymbol{c})$: x-component of the solution of OCP-4. $(\boldsymbol{d})$: y-component of the solution of OCP-4. $(\boldsymbol{e})$: z-component of the solution of OCP-4.

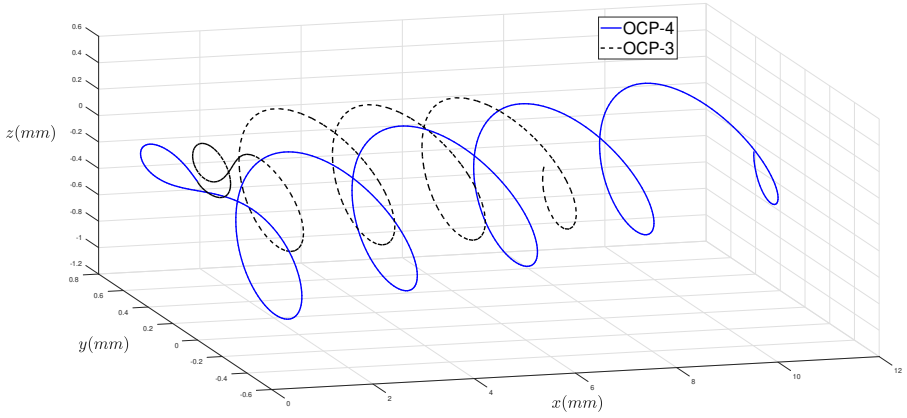

Figure 3.6: Trajectories of the swimmer associated with the solutions of OCP-3 and OCP-4.

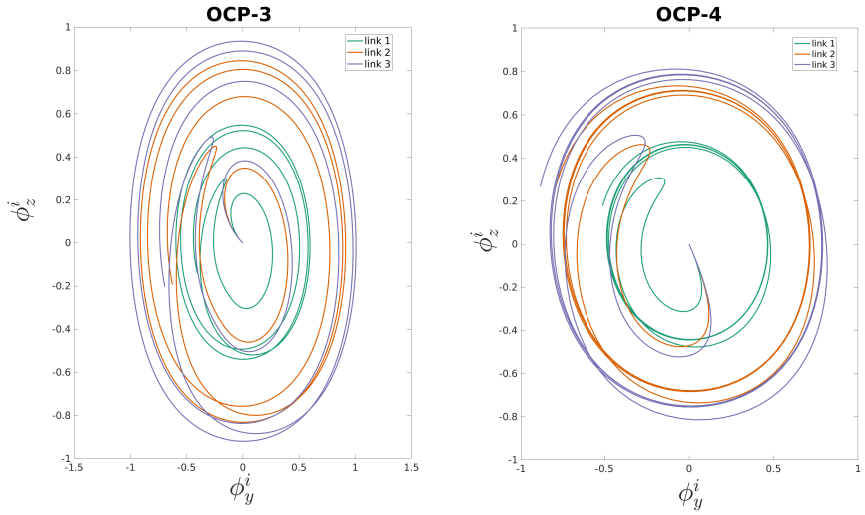

Figure 3.7: Shape variables of the swimmer when actuated by the non-planar optimal magnetic fields (OCP3 and OCP4) (after the initial transient state). Phase portrait of the relative angles in the $(\phi_y^i - \phi_z^i)$ for each link i of the tail.

These results shows the importance of non-planar actuation for maximizing the swimming speed, as the non-planar optimal magnetic fields out-perform the planar optimal actuations. However, the non periodic 3D solutions have the drawback that they lead to trajectories that drift away from the horizontal axis over time. The 2D optimal fields can still be useful in experimental settings where the degrees of freedom of the swimmer are limited or when limited to a planar actuating field (for

example, two orthogonal Helmholtz coils). The effectiveness of non-planar actuation has been corroborated in the literature by studies where non-planar helical waves have been shown to induce a faster propulsion speed for flagellar swimmers. For example, in [Khalil *et al.* 2018], the sperm-like microrobot's swimming speed increases between 1.2 and 2 times (depending on the viscosity of the fluid) when switching between a planar swimming induced by sinusoidal actuation and helical swimming induced by a conical magnetic field. This characteristic is also shown in [Chwang & Wu 1971] for self propelled swimmers. However, our work differs from these approaches as it does not rely on an a priori prescribed actuation pattern or shape deformation but optimizes the 3D driving magnetic field of the swimmer which allows the generation of swimmer-specific optimal actuation.

3.6.2 Periodicity of the solutions

Another difference between the planar and non-planar solutions is the periodicity of the optimal fields solutions of OCP-1 and OCP-2, which naturally leads to a periodic deformation of the tail of the swimmer, as seen in 3.4. Solving the planar optimal control problems for a longer final times results in solutions that have the same period, hence, it is possible to isolate a magnetic field pattern to actuate the swimmer experimentally. However, this is not possible in the case of the 3D optimal fields, as there are transient states at the beginning of the actuation before a periodic regime. The existence of these transient states in the non planar optimal fields suggest that the initial straight configuration of the swimmer is not optimal and also that strategies based on the stroke optimization of a flexible micro-swimmer in 3D are sub-optimal, which contrasts with the studies of the problem in 2D.

3.6.3 Optimization under a periodic constraints

The numerical solutions of the optimal control problems with a periodicity constraint are presented in this section. Here, the displacement of the swimmer is maximized with an additional periodicity constraint on the shape, orientation, and position on the y and z axis. This latter condition ensures that the swimmer doesn't drift from the horizontal axis when applying the periodic solutions repetitively over time.In addition to keeping the trajectory of the swimmer around the x-axis, the solutions of the optimal control problem with periodicity constraints, the solutions of the optimal control problem with periodicity constraints are particularly suited for experimental purposes, given that they provide simple 3D magnetic field pattern that can be repeated over time in order to drive the micro-swimmer.

Figure 3.8 shows the simulated horizontal displacement actuated by the repetition of the magnetic field patterns obtained through the resolution of the periodic optimal control problems for 3 seconds of straight swimming. The main difference with the solution of the problems without periodic constraints is the absence of

a significant gap between the non-planar and planar solutions, as the solution of $POCP-2$ results in a performance similar to $POCP-3$.

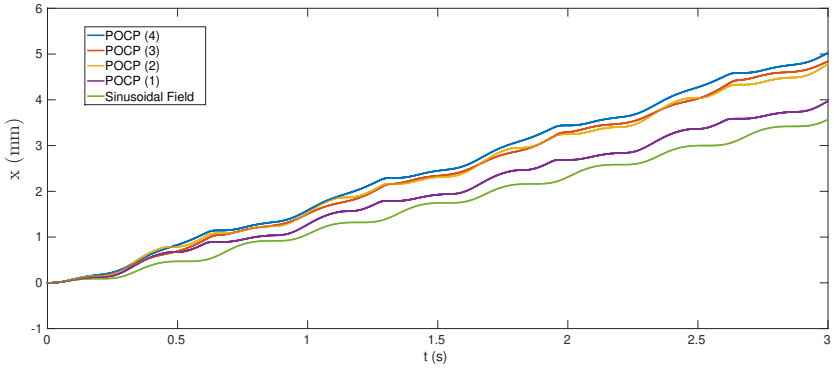

Figure 3.8: Comparison of x-displacements associated with the solutions of POCP1-4 and with the sinusoidal actuation

The planar periodic solutions (Figure 3.9) display similar control structures and trajectory shapes (Figure 3.10) than the non-periodic solutions.

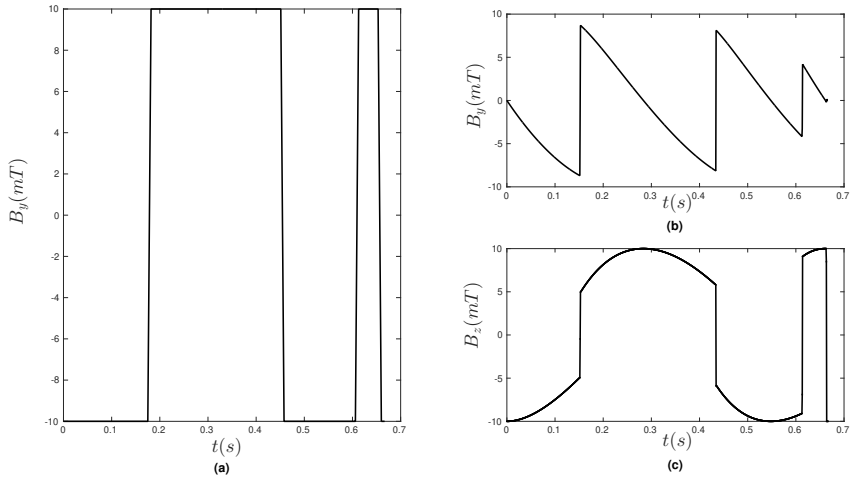

Figure 3.9: Solution of the planar periodic optimal control problems. $(\boldsymbol{a})$: y-component of the solution of POCP-1 compared with the sinusoidal field at optimal frequency $(1.5Hz)$. $(\boldsymbol{b})$: x-component of the solution of POCP-2. $(\boldsymbol{c})$: y-component of the solution of POCP-3.

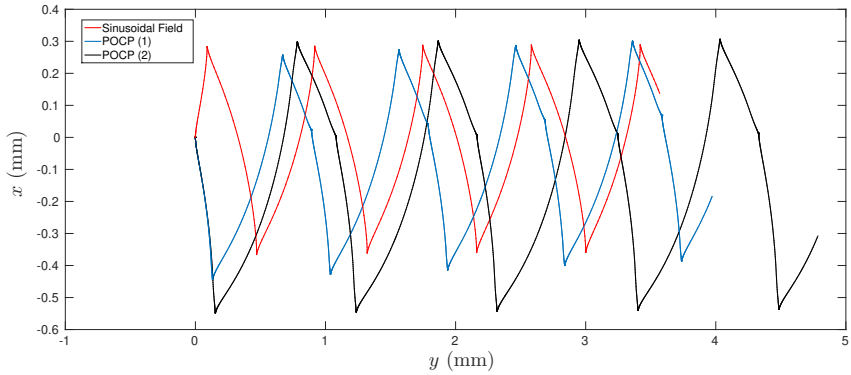

Figure 3.10: Optimal planar trajectories associated with POCP-1 and POCP-2 compared with the trajectory of the swimmer actuated by the sinusoidal field.

Figure 3.11 shows the optimal 3D magnetic field patterns (solutions POCP-3 and POCP-4). Repeating these magnetic field patterns over time make the swimmer revolve around the x-axis, drawing a "figure-eight" pattern in the $y-z$ plane (see Figure 3.12).

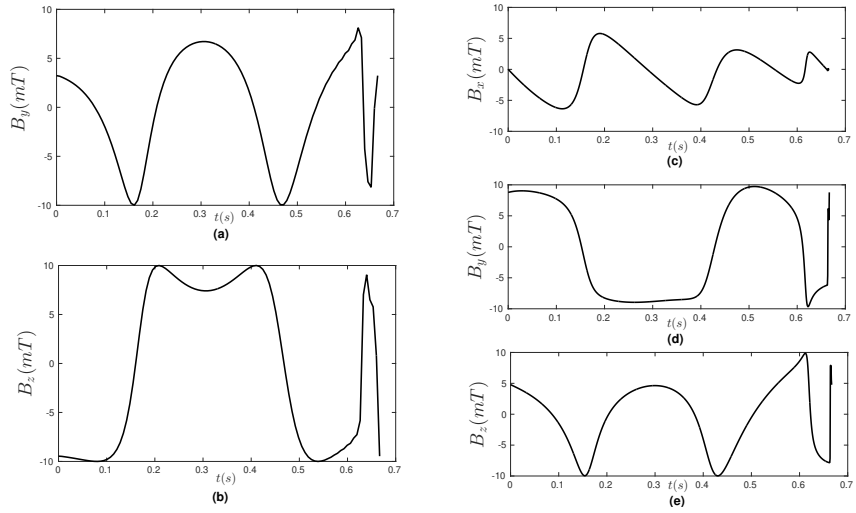

Figure 3.11: Solution of the non-planar periodic optimal control problems. $(\boldsymbol{a})$: y-component of the solution of POCP-3. $(\boldsymbol{b})$: z-component of the solution of POCP-2. $(\boldsymbol{c})$: x-component of the solution of POCP-4. $(\boldsymbol{d})$: y-component of the solution of POCP-4. $(\boldsymbol{e})$: z-component of the solution of POCP-4.

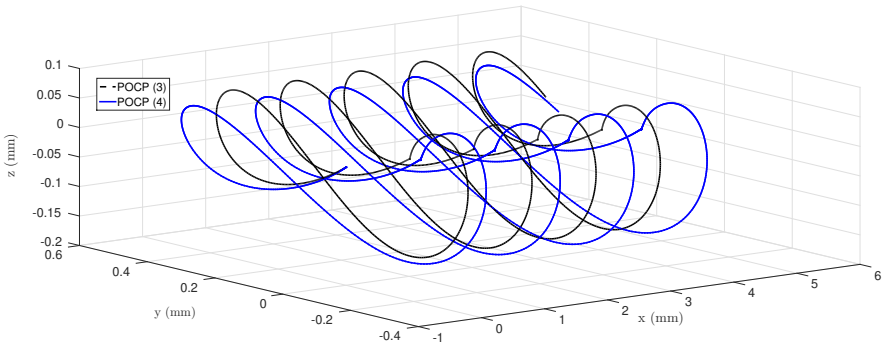

Figure 3.12: Trajectories of the swimmer associated with the solutions of POCP-3 and POCP-4.

3.6.3.1 Approximation of the periodic solutions

The solutions of the optimal control problems with a periodicity constraint are approximated by their trucated Fourier series in order to compare between the trajectories of the swimmer under the optimal actuation and under approximations of the numerical solution. The goal here is to see the number of Fourier modes that characterizes the solutions of the optimal control problems (POCP-1..4).

Denoting by X_* the simulated (discrete) trajectory from the optimal solutions and by X_j $j \in \mathbb{N}$ the simulated trajectory of the swimmer when actuated by the j first Fourier modes of the solution, the relative trajectory error is defined as :

$$E_T = \frac{||X_* - X_j||_F}{||X_*||_F}, \tag{3.26}$$

where $||.||_F$ is the Frobenius norm.

Figure 3.13 shows a rapid decrease in the relative trajectory error as the number of coefficients of the Fourier series of the solution of the periodic optimal control problems $POCP - i$ increases. From this, we can see that the trajectory of the swimmer using the approximation of the optimal controls by their first 5 Fourier coefficients is close to the optimal trajectory. This entails that one could devise an computationally cheap optimization process where only these modes are computed, for example by adapting the method used in ([Tam & Hosoi 2007]) for the Purcell swimmer.

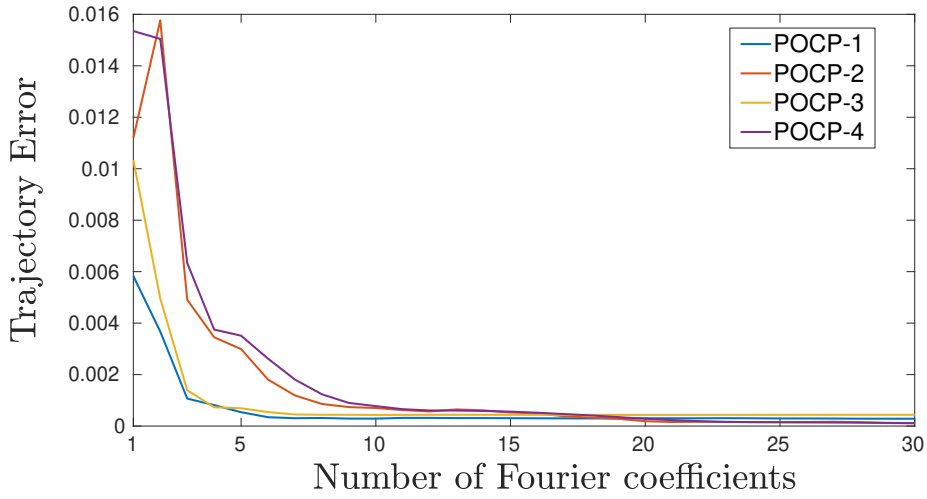

Figure 3.13: Error between the trajectory under the optimal solution of POCP-i for $i \in 1 \cdots 4$ and the trajectories when the swimmer is actuated by a truncated Fourier series of the solution.

3.6.4 Influence of the number of links on the solutions

An analysis of the influence of the number of links of the model on the optimal trajectories and magnetic fields is made in order to compare the solution of the optimal control problem for a varying degree of shape discretization. This is done by solving the optimal control problems OCP$1-4$ for an increasing number of links (from the simplest case of a single-linked swimmer to $N = 7$). In order to compare between the solutions, we use the mean absolute error (MAE) between the solutions of the optimal control problems with N links for the tail and the solution with $N+1$ links. The choice of using the MAE has been made in order to compute a distance between the curves that is less sensible to small differences that are due to the time discretization of the direct solver. In particular, for the planar solutions where the magnetic field is discontinuous, there is a slight difference between the switching times of the solutions which can lead to an artificially high error when using the l_2-norm for example.
The mean absolute trajectory error E_{tr} is defined as :

$$E_{tr} = \frac{\sum_{i=1}^{m} |\boldsymbol{X_i^N} - \boldsymbol{X_i^{N-1}}|}{m}, \tag{3.27}$$

where m is the number of timesteps of the numerical solution, and $\boldsymbol{X_i^N}$, $i = (1 \cdots N)$ is the i^{th} component of the optimal trajectory using N links for the tail. Similarly, the solution error E_{sol} is defined as :

$$E_{sol} = \frac{\sum_{i=1}^{m} |\boldsymbol{B_i^N} - \boldsymbol{B_i^{N-1}}|}{m}, \tag{3.28}$$

where $\boldsymbol{B_i^N}$, $i = (1 \cdots N)$ is the i^{th} component of the optimal solution using N links for the tail.
Figure 3.14 shows the change of the optimal magnetic field shape as N increases. From this, we can see that for OCP-1,OCP-2, and OCP-3, the solutions depend weakly on the number of links, as the small error $\approx 0.05mT$ can be attributed to the time discretization during the resolution. For OCP-4, the solutions strongly depend on the number of links for $N < 3$ before converging to a magnetic field that does not change when N increases. In particular, the planar solutions (OCP 1 - 2) do not depend on the number of links of the tail. This entails that the simplest case of a 1-linked swimmer model (which leads to a dynamic system of dimension 4 in the planar case) can be used for the optimal control design of magnetic micro-swimmers, which opens the door to the possibility of the online resolution of the optimal control problems in 2D and the design of Model Predictive Control frameworks based on this model. The optimization is less computationally cheap when optimizing for the non-planar magnetic fields, where the optimal fields only "converge" starting from $N = 3$, which leads to a dimension 12 dynamic system. These results show that the displacements of a flexible low-Reynolds magnetic swimmer can be captured and optimized using a very coarse discretization of the tail.

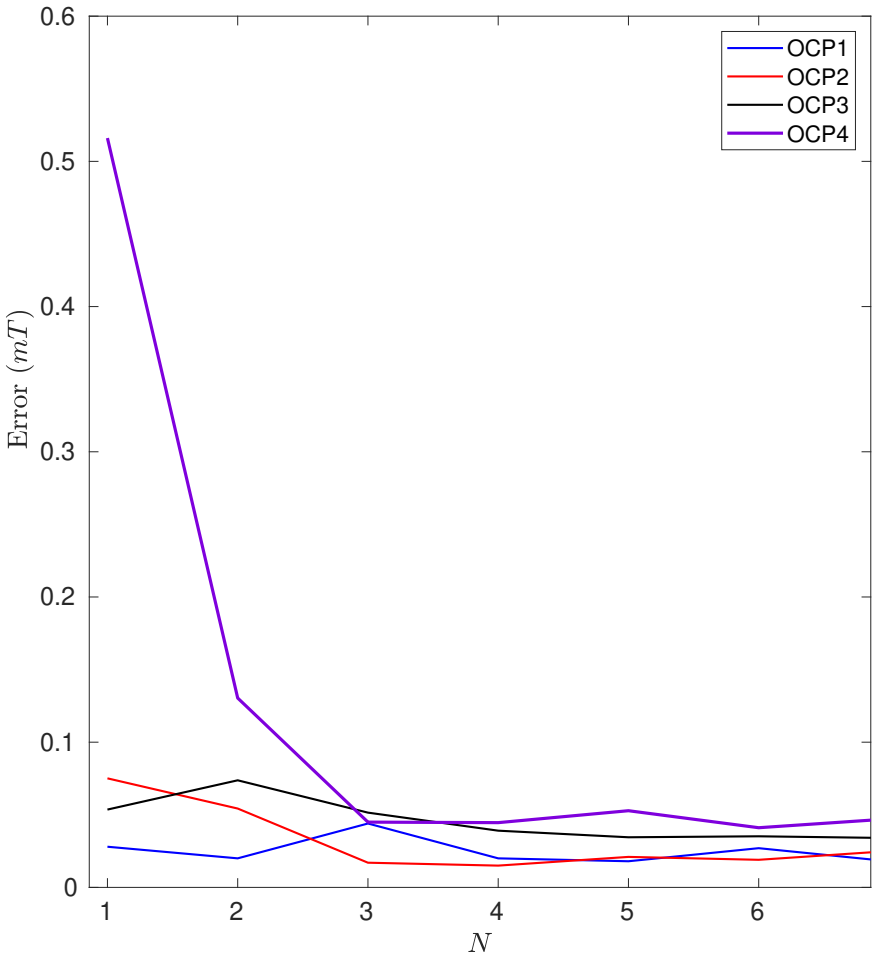

Figure 3.14: Errors between the optimal solutions for an increasing number of links of the tail of the swimmer.

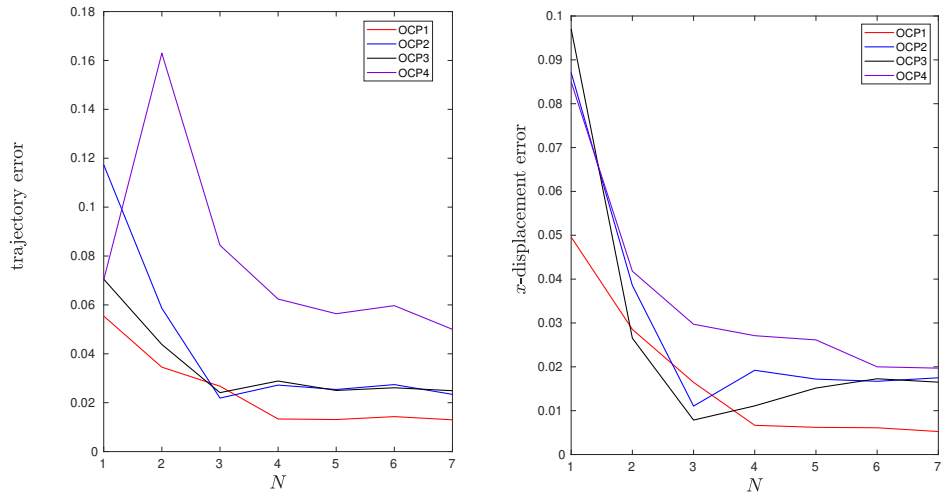

Figure 3.15: Errors between the optimal trajectories for an increasing number of links of the tail of the swimmer.

3.7 Conclusion

In this chapter, the simplified, Resistive Force Theory-based 3D dynamical model for flagellar micro-swimmers was used to investigate different planar and non-planar optimal actuation strategies for magnetic micro-swimmers that out-perform the commonly used sinusoidal actuation. In particular, the non-planar actuation strategies lead to a novel 3D trajectory and are significantly more efficient than the planar ones. Another result stemming from the numerical simulations is the investigation of optimal actuation strategies that do not rely on a static orientating magnetic field, as allowing all the components of the magnetic field to be optimized leads to an increase in swimming speed. The solutions of the optimal control problem with periodicity constraints provide simple magnetic field patterns that can be repeated over time to drive flexible magnetic-swimmers, with a propulsion speed significantly greater than the commonly used sinusoidal actuation. The focus of the next chapter will be the implementation of the optimal magnetic fields on the experimental validation of the model and these solutions. Although the main focus of this section was to optimize the speed of the flexible robot for swimming along a straight line, these swimming strategies are easily implementable for open loop or closed loop path following (see [Oulmas *et al.* 2017] for an example) by applying the static component of the magnetic field in the direction tangent to the curve, and the actuating components in the normal and binormal directions.

Chapter 4

Experimental Results

Contents

4.1 Introduction

In the previous chapters, we developed a simplified dynamical model of a flexible magnetic low Reynolds number swimmer and computed optimal magnetic actuation patterns that maximize the swimmer's propulsion speed. The main goal of this chapter is to show that the model developed in Chapter 2 can be used to design optimal controls that are usable in experiment, and that it can accurately predict the horizontal displacement of an experimental low-Reynolds swimmer.

The recent advances in the last decades moved the field of micro-robotics from proof-of concept studies of the locomotion of micro-robots [Dreyfus *et al.* 2005], to the fabrication of micro-swimmers that are functionalized to achieve specific tasks for various potential biomedical and environmental applications such as cargo delivery [Zhang *et al.* 2012], sensing [Zarei & Zarei 2018], and removal operations [Guix *et al.* 2013]. The efficient motion control and planning of these devices is of utmost importance in order to achieve these tasks. However, model-based control of flexible magnetic micro-swimmers using computational fluid dynamics (CFD) models is a computationally prohibitive task due to the complex fluid-structure interaction coupled with the magnetic effect. Thus, we aim to show that a simplified, RFT-based model, is sufficient for the control design of experimental flexible magnetic micro-swimmers. Moreover, due to its simplicity and its ODE form, the dynamic model developed during this thesis is modular enough to be adapted for the optimization of the actuation of the swimmer for specific tasks such as cargo delivery, as well as for different designs of flexible swimmers such as the multi-link nanowires of [Jang *et al.* 2015].

The manufacturing and localization of microscopic flexible swimmers is a complex task due to their scale. The fabrication of these devices requires the use of advanced and expensive 3D printing methods [Stanton *et al.* 2015]. Localization methods for micro-scale swimmers are equally costly, requiring high-precision optical devices in order to track the swimmers. Hence, since the fluid motion around a micro-scale swimmer is only characterized by the dimensionless Reynolds number, it is more cost-effective to use scaled-up, centimeter-scale flexible swimmers that are put in a highly viscous liquid in order to emulate the same conditions as the micro-scale. This is the approach used in the following experiments, where a centimeter-scale flexible swimmer is used and immersed in pure glycerol in order to have a Reynolds number of around 10^{-2}, which is in the same range as a micrometer-scale swimmer immersed in water at a comparable speed with respect to body length.

The proposed method used to generate optimal controls for the experimental swimmer using the modelisation and optimization tools presented in the previous chapters can be summarized as :

1. Characterization of the experimental swimmer by measuring its velocity-frequency response curve.
2. Parameter fitting of the model to match the observed velocity-frequency response curve.
3. Numerical resolution of the periodic optimal control problem choosing the same frequency as the observed optimal frequency for sinusoidal actuation.
4. Approximation of the optimal actuation pattern by a truncated Fourier series and implementation in the experimental setup.

The chapter is organized as follow : First, the experimental setup is described. This is followed by an overview of the fitting of the model to the experimental data, the optimal control computation, and the implementation of the optimal control in the experimental setup. The experimental results are then presented and discussed.

4.2 Experimental setup

The experimental setup used in this thesis was designed by Tiantian Xu during her PhD thesis [Xu 2014]. This work focused on the design, fabrication and characterization of centimeter-scale helical swimmers swimming in a viscous fluid (in order to emulate conditions at the micro-scale), as well as realize a visual servo control of the orientation of the swimmers in the 3D space, and a path following on the horizontal plane. In a subsequent thesis [Oulmas 2018], the fabrication of centimeter-scale flexible swimmers, which were used in the present work, was realized as well as a generalization of the path following algorithm to 3D curves. The swimmer, which can be seen in figure 4.1, consists of a magnetic disk (Neodyminum-Iron-Boron permanent magnet) with $0.3mm$ in height and $0.77mm$ in diameter attached to a

silicone tail with $7mm$ in length and $1mm$ in diameter. The swimmer's tail was made using RTV silicone (Room-Temperature-Vulcanizing silicone), which is composed of a base and a catalyzer which solidify at room temperature when mixed together. The tail was shaped using a 3D printed mold and painted black in order for the swimmer to contrast with the surrounding liquid, which is backlit, so as to facilitate the motion tracking. The swimmer is immersed in pure glycerol to ensure low-Reynolds number conditions ($\approx 10^{-2}$),

Figure 4.1: Flexible magnetic swimmer used in the experiments

The actuating magnetic field is generated by a system of three orthogonally arranged Helmholtz coil pairs, depicted in figure 4.2. As said in section 1.3.1 of the introduction, this is arguably the most popular magnetic generation method for magnetic micro-swimmers, and it allows the generation of a homogeneous magnetic field at the center of the coils with three degrees of freedom. Details about the fabrication and calibration of the magnetic field generation system can be found in [Xu 2014]. Each pair of coils is driven by a servoamplifier (Maxon Motor) which outputs a constant current that depends only on the input voltage outputted by an I/O card (Sensoray 626) controlled by a computer running the real-time operating system RTLinux.

As seen in figure 4.2, two cameras provide a side view and a top view of swimmer. The movements of the swimmer are tracked in real-time using the Visual Servoing Platform (ViSP) library, [Marchand *et al.* 2005], which is a C++ API for visual tracking and visual servoing. The tracking method used is the so-called 'Blob detection method' [Kaspers 2011], which relies on detecting the swimmer using the contrast between its dark colour and the light, backlit surroundings. From this, the orientation and the position of the barycentre of the swimmer on both the side and top planes are obtained using the image moments provided by ViSP, which are then used to reconstruct the orientation and position of the swimmer in 3D (see [Xu 2014] for the calculations). Figure 4.3 shows the image of the swimmer provided by the side camera and the tracking of the overall shape of the swimmer (in green), its barycenter (red cross), and its estimated orientation (blue arrow).

The visual tracking method allowed the open and closed loop control of the orientation of the swimmer, and the path following of a planar curve, which were implemented by Tian Tian Xu in [Xu 2014]. The path following algorithm was then generalized to 3D curves in [Oulmas *et al.* 2017]. The aim of the algorithm is to minimize the distance and orientation errors between the swimmer and the reference path by computing the required steering angular velocities, making it reach to the

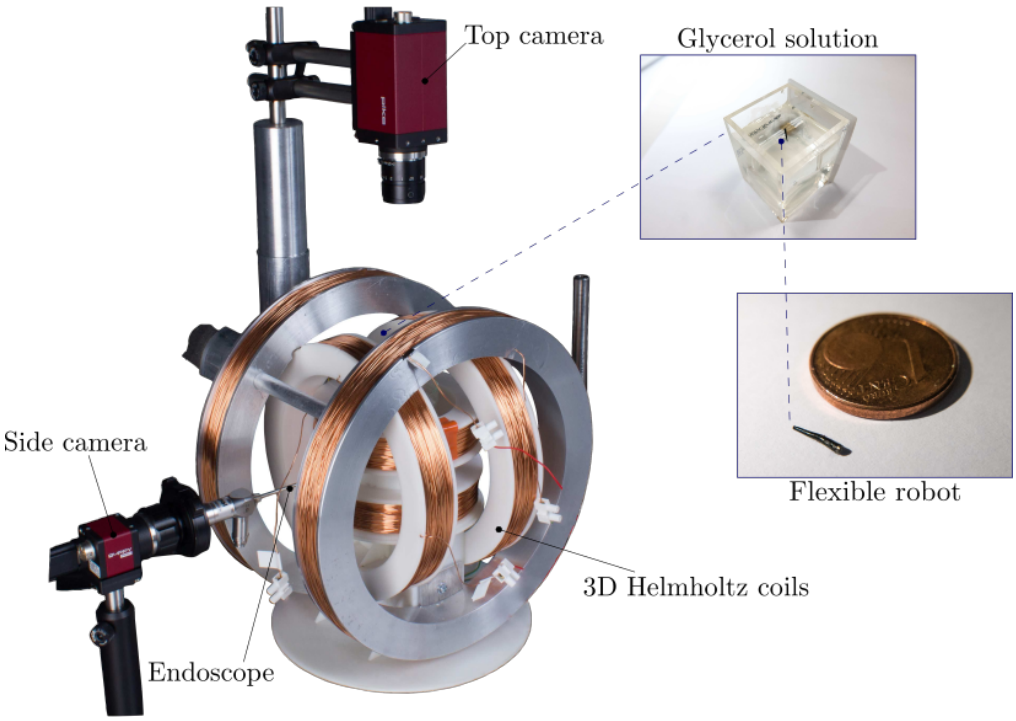

Figure 4.2: Experimental setup ([Oulmas *et al.* 2017]). The three orthogonal Helmholtz coils generate a homogeneous magnetic field in the center, where the swimmer has been placed and immersed in pure glycerol. The swimmer is tracked using two perpendicular cameras.

path then going along it by following the path's tangential vector. The closed loop control algorithm computes at each iteration the required steering angular velocity for the minimization of the orientation and distance errors between the swimmer and the curve by applying a state-feedback control after linearizing the kinematic of the swimmer into a multi-input generalization of the "chained-form" introduced in [Samson 1995] which is used to model the kinematics of nonholonomic mechanical systems.

4.3 Parameter fitting

The first step for the optimal control design method is the fitting of the RFT coefficients and the elasticity coefficient of the model in order to match the displacements of the experimental swimmer (see section 2.5 in chapter 2). As said in 2.5, the parameters are determined by a non-linear fitting method in order match the velocity-frequency response curve of the experimental swimmer. Matching this curve with the model guaranties that the elasto-hydrodynamics of the simulated swimmer are close to the experimental one given that the optimal swimming frequency is char-

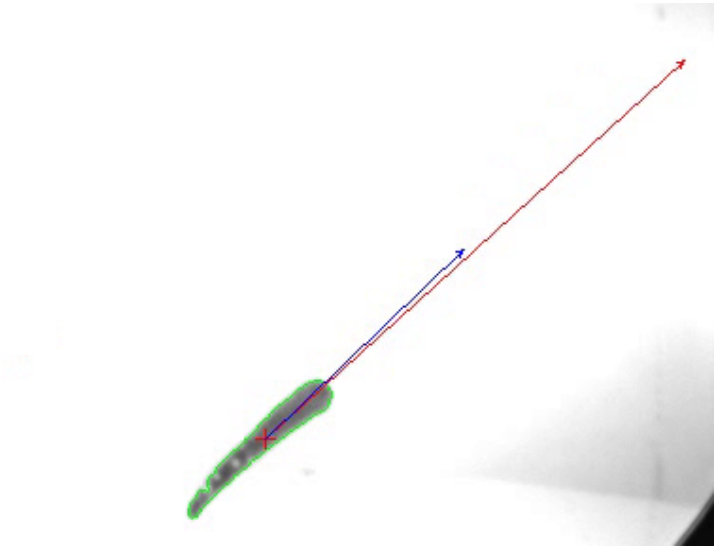

Figure 4.3: Real-time tracking of the position of the barycenter of the swimmer (red cross) and it's orientation (blue arrow)

acterized by the sperm number of the swimmer, which in turn encodes the relative importance of the elastic forces compared to the viscous drag. We consistently use a fixed frame (x, y, z) where the x-axis is the desired swimming direction (given as an input in ViSP) , the z-axis is vertical and the y-axis is along the axis of the side camera. Due to the fact that the experimental swimmer is not completely neutrally buoyant, a static magnetic field at an angle of approximately $15° - 20°$ elevation with respect to the swimming direction is applied to compensate the gravity.

The experimental velocity-frequency response curve of the swimmer is measured with an actuating field of the form :

$$\boldsymbol{B}(t) = \begin{pmatrix} B_x & B_y \cos(2\pi f t) & 0 \end{pmatrix}^T , \tag{4.1}$$

where the frequency range is $f = (0 \cdots 3Hz)$, and $B_x = 2.5mT$ and $B_y = 10mT$. The measured frequency-response curve of the swimmer has the typical shape for magnetically driven flexible swimmers at low Reynolds number [Espinosa-Garcia *et al.* 2013, Khalil *et al.* 2014, Yu *et al.* 2006], as it increases with the actuating frequency until an optimum point ($f = 1.5Hz$) then slowly decreases. Figure 4.4 shows the agreement between the experimental ($N = 6$ trials) and simulated frequency responses after fitting. The mean relative error (∞-norm) between the simulated horizontal displacement using the fitted model and the observed horizontal displacement of the swimmer (for $N = 6$ trials) when actuated by the sinusoidal field at optimal frequency ($1.5Hz$) is $0.18(\pm 0.015)$. Figure 4.5 shows the experimental and simulated horizontal displacements of the swimmer for one trial.

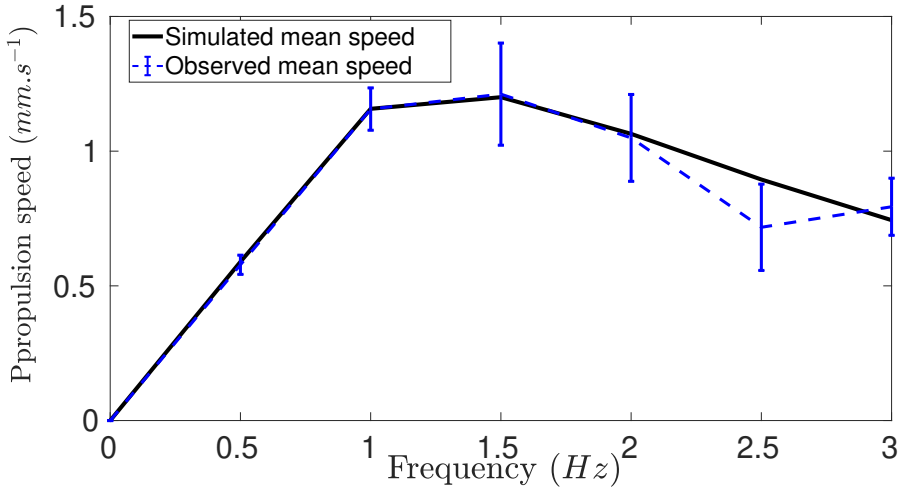

Figure 4.4: Experimental (N = 6) and simulated horizontal swimming velocities for the frequency range $f = (0 \cdots 3Hz)$.

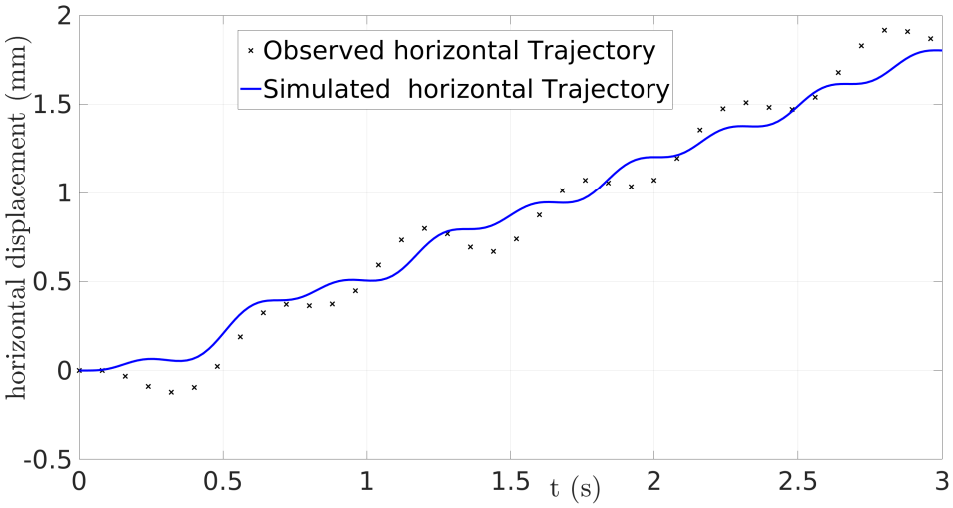

Figure 4.5: Experimental and simulated horizontal displacement of the swimmer at the optimal actuating frequency $(1.5Hz)$

4.4 Optimal Control computation

After fitting the dynamic model to the experimental swimmer, the optimal control for the swimmer is computed. We choose to solve the POCP-3 optimal control problem, (see section 3.3 in chapter 3)), which consists of maximizing the mean horizontal propulsion speed of the swimmer under the constraint of a periodic deformation :

$$\begin{cases} \max \quad x(T)\,, \\ \dot{\boldsymbol{Z}}(\boldsymbol{t}) = f(\boldsymbol{Z}(\boldsymbol{t}), \boldsymbol{B}(\boldsymbol{t}))\,, \\ \boldsymbol{Z}(0) = 0\,, \\ \boldsymbol{Z}(T) = 0\,, \\ B_x(t) = B_x\,, \\ ||(B_y(t), B_z(t))|| \leq B_0\,, \\ B_z(t) = 0\,, \end{cases} \tag{4.2}$$

where the bounds on the orientating field and the time-varying fields are taken to be the same as the sinusoidal field used in the experiments ($B_x = 2.5mT$ and $||(B_y(t), B_z(t))|| < 10mT$). The deformation period is chosen to be the same as the observed optimal period for a sinusoidal actuation ($T = \frac{1}{1.5}s$) and it is imposed that the swimmer returns in its initial orientation and position on the y and z-axis at the end of the period.

Although the optimal control formulation where all the components of the magnetic fields are free to be optimized (POCP-4 in Chapter 3) has a better performance in simulations, it fails to drive the swimmer in a straight trajectory because of the non-perfect experimental conditions (non-buoyancy of the swimmer) and because of the low sampling frequency (10 Hz) of the magnetic generation system, which applies to the swimmer a discrete approximation of the prescribed magnetic field. The planar solutions presented in the previous chapter (POCP-1 and 2) , where one of the components of the magnetic field present discontinuities have the same drawback given that the switching times could not be captured during the sampling of the magnetic field.

Figure 4.6 shows the result of the numerical optimization, where we can see the y $(\boldsymbol{a})$ and z $(\boldsymbol{b})$ components of the optimal magnetic field. This results in a simple magnetic field shape, shown in $(\boldsymbol{c})$, where the actuating strategy over one deformation period is a partial rotation (about two thirds of a circle) of the magnetic field followed by a full rotation in the opposite direction. Repeating this pattern over time makes the swimmer revolve around the x axis, drawing a "figure-8" in the $y - z$ plane. Figure 4.7 shows the simulated optimal trajectory of the swimmer compared to the trajectory under the sinusoidal field. The simulated fields perform better (mean propulsion speed of $1.45\,10^{-3}\,\mathrm{ms}^{-1}$) than the sinusoidal actuation (mean propulsion speed of $1.2\,10^{-3}\,\mathrm{ms}^{-1}$).

The numerical solution of the optimal control problem (Figure 4.6) is approximated by its truncated Fourier expansion (first 10 modes) and then implemented in the ViSP interface. It is worth noting that in simulation, the first 5 coefficients of the series characterizes the optimal magnetic fields and the trajectory (see figure 3.13 in 3), which means that there is no significant loss of speed or drifting from the horizontal swimming direction when using this approximation of the optimal field.

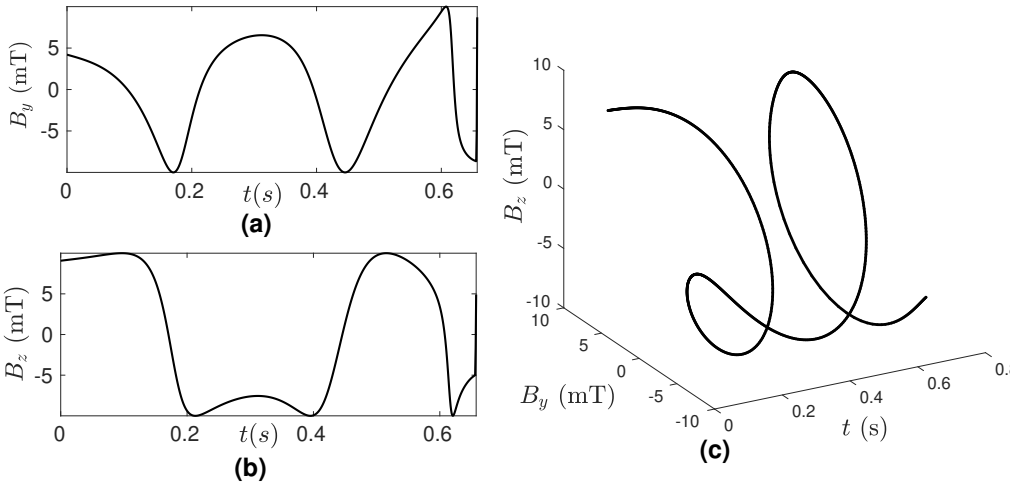

Figure 4.6: Actuating magnetic field that maximizes the horizontal speed of the swimmer. **(*a*)** and **(*b*)** are respectively the y and z components of the magnetic field. **(*c*)** : Shape of the actuating *optimal* magnetic field deriving from the optimization process during one period.

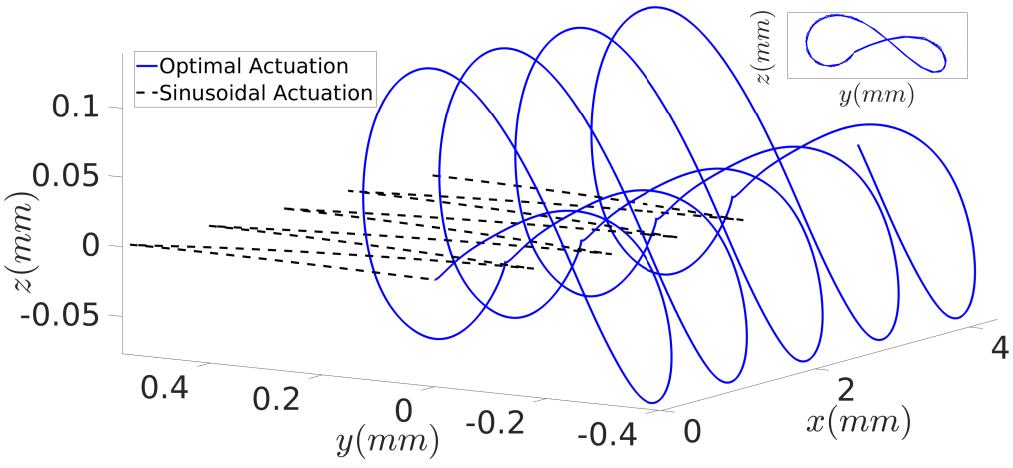

Figure 4.7: Simulated trajectory of the head of the swimmer under both the optimal and sinusoidal field for 3 seconds of straight swimming under both actuation patterns. In the corner, the trajectory in the $y-z$ plane is depicted.

4.5 Experimental Results

After the implementation, the swimming performances of both the optimal field and the sinusoidal field were compared, keeping the same experimental conditions for each run (fixed gravity compensation angle, same viscosity and temperature ...).

As predicted by the simulations, the optimal field out-performs the sinusoidal field in terms of horizontal propulsion speed, as shown in Figure 4.8. From this figure, we see that the dynamic model accurately predicts the horizontal displacements of the swimmer under both magnetic fields. It is less accurate in predicting the value of the amplitudes of the oscillations of the swimmer along the y and z axis as can be seen from comparing figures 4.9 and 4.7. However, the shapes of the predicted and experimental trajectories match qualitatively.
Figure 4.9 shows the 3D trajectory of the experimental swimmer during 3 seconds of horizontal swimming. This observed trajectory qualitatively matches the 'figure-eight' simulated trajectory seen 4.7, however the dynamical model fails to accurately predict the y and z-displacements of the swimmer. Figure 4.10 shows the deformation pattern undergone by the experimental swimmer in the two perpendicular planes. The swimmer's displacements are characterized by the deformations of its tail, as a consequence of the forces and torques balances in equation 2.41. The experimental deformation patterns of the tail under both magnetic fields are shown in Figure 4.10, which illustrates how the swimmer breaks the time-reversible symmetry of the Stokes flow to propel in both cases. In particular, the deformation pattern under the optimal field shows a torsion of the tail of the swimmer in addition to a beating pattern. This torsion of the tail causes the swimmer to go out-of-plane. This same effect of the torsion on the trajectory has been shown in the case of flagellated cells that self propel along a 3D chiral path when the torsion of the flagellum is coupled with an oscillating waveform [Jikeli *et al.* 2015].
Under optimal actuation, the swimmer reaches a mean horizontal propulsion speed of $1.54 \pm 0.3\,10^{-3}\,\mathrm{ms}^{-1}$ ($N = 6$). The mean relative error (∞-norm) between the simulated and observed x-displacement is $0.16(\pm 0.02)$. We refer the reader to this video for a side-by-side comparison of the displacements of the swimmer actuated by the optimal and sinusoidal field. Figures 4.11 and 4.12 shows snapshots of the video from the side and top cameras, comparing the trajectory of the swimmer under both actuations.

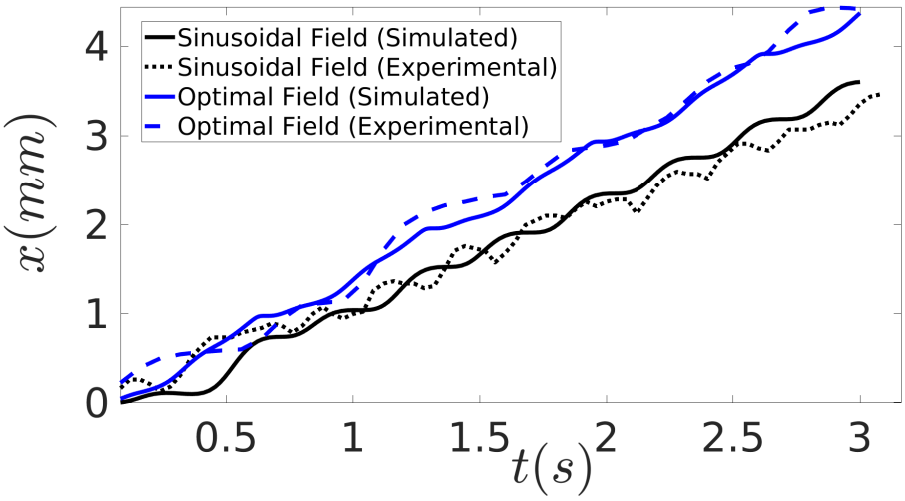

Figure 4.8: Simulated and experimental horizontal displacements of the swimmer actuated by the optimal magnetic field and the sinusoidal magnetic field for 3 seconds of straight swimming under both actuation patterns.

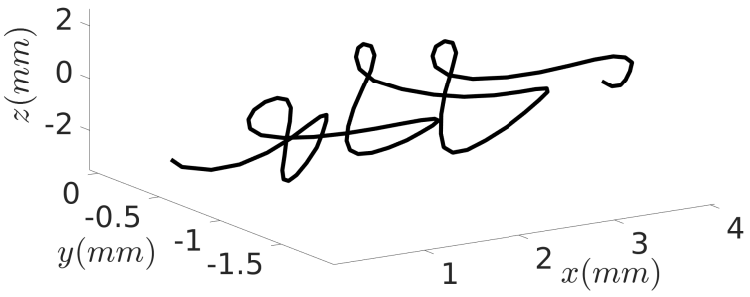

Figure 4.9: Trajectory of the experimental swimmer actuated by the optimal magnetic field given in Figure 4.6 during three periods of the magnetic field.

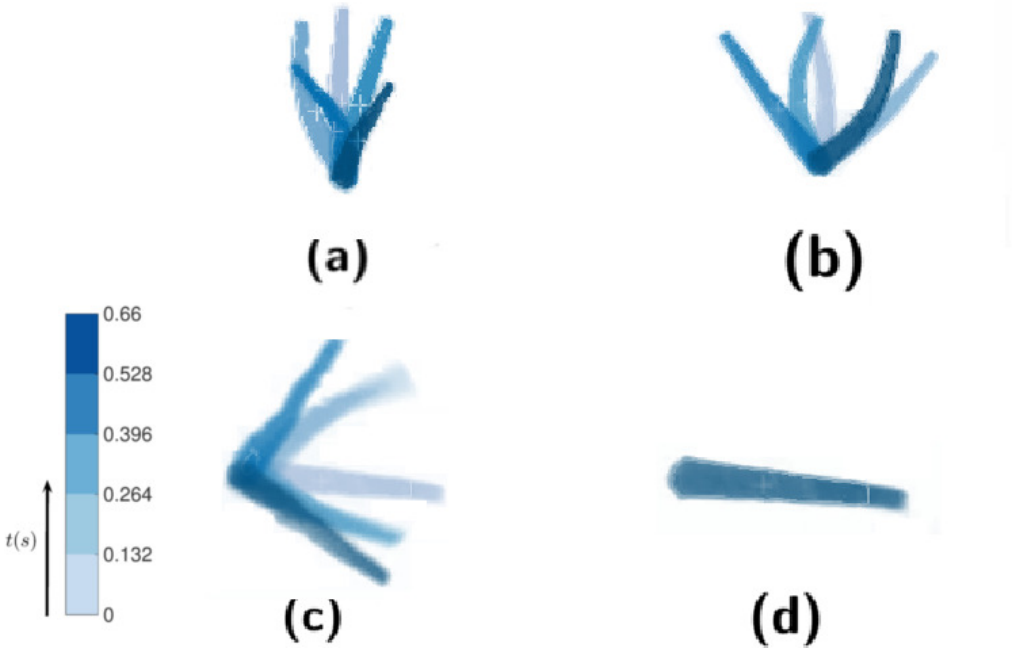

Figure 4.10: Deformation pattern of the experimental swimmer actuated by the optimal magnetic field and the sinusoidal magnetic field over one period in two planes. ((a) : Optimal field, top view, (b) : Sinusoidal field, top view, (c): Optimal field, side view, (d) : Sinusoidal field, side view.). The snapshots of the experimental swimmer are taken at equal time steps over a period of the actuating fields. We observe (as expected) no deformation in the side plane for the sinusoidal field.

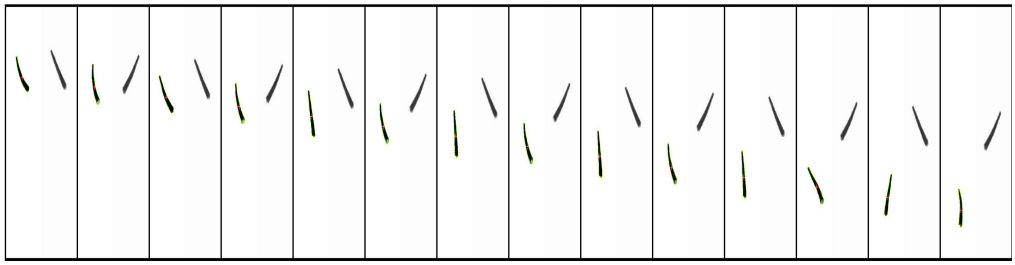

Figure 4.11: Comparison between the displacements of the swimmer actuated by the optimal field and by the sinusoidal field at the optimal frequency. Snapshots taken from the top camera at a 0.8 seconds interval.

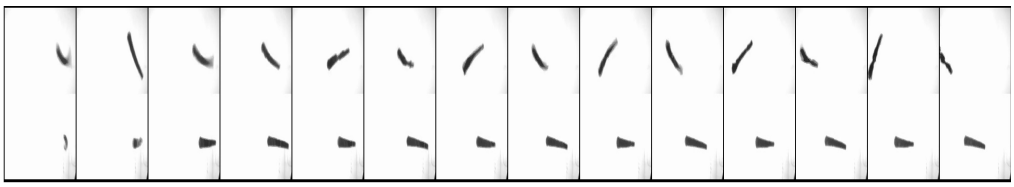

Figure 4.12: Comparison between the displacements of the swimmer actuated by the optimal field and by the sinusoidal field at the optimal frequency. Snapshots taken from the side camera at a 0.8 seconds interval.

To illustrate this new actuation method for eventual applications, the optimal field was also implemented in the path following algorithm of [Oulmas *et al.* 2017] and compared to the sinusoidal actuation. This has been made by applying at each iteration of the path-following algorithm the static component of the magnetic field in the direction tangent to the curve to be followed, and the time-varying components in the normal and binormal directions. This can be interpreted as a greedy optimization method for the maximization of the speed at which the swimmer follows the curve given that the forward propulsion of the swimmer along the direction prescribed by the closed-loop algorithm is optimized at each step.
Using the optimal actuation pattern instead of a sinusoidal field in the path following algorithms improves the speed of the swimmer, without impairing the trajectory and angular errors between the swimmer and the prescribed path, as seen in figure 4.13,which shows snapshots of the path following of an incline sinusoidal curve, comparing between both actuation patterns, and figure 4.14, which shows the trajectory of the swimmer during the path following when using the optimal actuation.

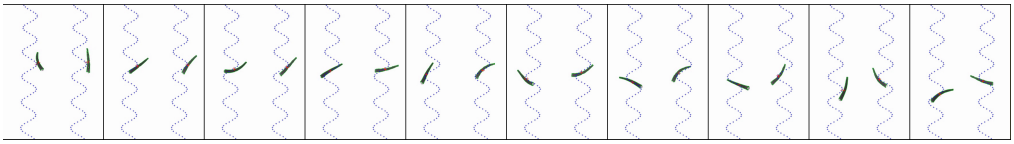

Figure 4.13: Comparison between the path following of an incline sinusoid for the swimmer actuated by the optimal field and by the sinusoidal field at the optimal frequency. Snapshots taken from the top camera at a 0.8 seconds interval.

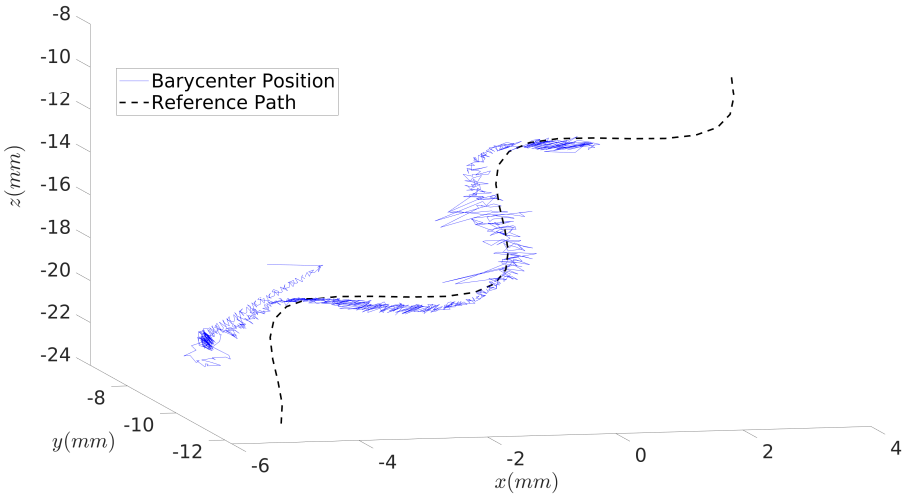

Figure 4.14: trajectory of the swimmer during the path following.

4.6 Discussion

Using the approximate RFT model developed in chapter 2 as a dynamic constraint for an optimal control problem, we computed a novel 3D actuation strategy for an experimental flexible magnetic low-Reynolds swimmer that out-performs the classical sinusoidal actuation in terms of propulsion speed. Moreover, the dynamic model accurately predicts the horizontal displacement of the swimmer under both the optimal and sinusoidal actuation patterns. However it is less accurate in predicting the amplitudes of the oscillations of the swimmer around the x and y axes. The dynamic model could be improved in order to better capture the oscillations of the experimental swimmer by including the additional constraint that the observed amplitudes match the experimental one during the parameter fitting optimization.
The optimal control design method used in this thesis has the advantage of providing swimmer-specific optimal actuation, as it is based on a dynamic model that is able to be fitted on the measured velocity-frequency response of experimental swimmers. For this reason, the model can easily be adapted to optimize the displacement of different flexible swimmers than the one used in the present work, such as the multi-link nanowires of [Jang *et al.* 2015], or the sperm-templated swimmer of [Khalil *et al.* 2014].
The experimental setup used has several limiting factors as it suffers from the usual drawbacks of open-loop control of microswimmers as external perturbations affect the path of the swimmer and hinders the reproducibility of experiments, mainly thermal effects (which changes the viscosity of the fluid between experiments), parasitic magnetic forces arising from the non-uniformity of the magnetic field, and the weight of the swimmer given its non buoyancy. This explains the relatively high errors margins for the measurements of the speed of the swimmer (for example in

the velocity-frequency response curve 4.4).
Another limiting factor is the low sampling frequency ($10Hz$) the provided by the system, which entails that the effective magnetic fields applied to the experimental swimmer are only a coarse discrete approximation of the prescribed controls. For this reason, the optimal control formulations where all the components of the magnetic fields are optimized (POCP-4) are not adapted for these conditions, despite the theoretical performance of these solutions over those using a static orientating field. The planar solutions presented in the previous chapter (POCP-1 and POCP-2), where one of the components of the magnetic field present discontinuities have the same drawback given that the switching times could not be captured during the sampling of the magnetic field.
Current research is focused on finding a solution to allow propulsion of flagellated swimmers in confined environments ([Ishimoto & Gaffney 2014, Shum & Gaffney 2015]) or in the presence of obstacles, such as the human vasculature ([Jang *et al.* 2018]). Hence, the next step of this study should be the optimization of the actuation of the swimmer in the presence of boundaries, using boundary-corrected Resistive Force Theory [Katz 1974]. The experimental setup should be adapted for this purpose by confining the swimmer in a narrow channel or near a planar boundary. This requires a substantial improvement on the tracking of the swimmer as the distances between the swimmer and the boundaries need to be accurately evaluated in real time in order to fit the model.

4.7 Conclusion

In this chapter, a joint experimental-computational approach was adopted to study the swimming performance of magnetically actuated low-Reynolds swimmer, using the modeling and optimization tools presented in the previous chapters. The goal of this study was to present and a procedure for the design of optimal actuation for experimental flagellar magnetic microswimmers based on numerical optimization using using a simple, computationally inexpensive model that predicts the horizontal displacement of the swimmer. Using this approach, we simulate magnetic fields that maximize the horizontal propulsion speed of the swimmer.
From this, we are able to propose a novel magnetic actuation pattern that allows the swimmer to swim significantly faster compared to the usual sinusoidal actuation. This actuation pattern is experimentally tested on a scaled-up, macroscopic low Reynolds number swimmer. The dynamic model used accurately predicts the horizontal displacement of the experimental swimmer under both the optimal and sinusoidal actuation.
Although the dynamic model used is limited in its accuracy, since it is based on an approximation of the fluid-structure interaction of the swimmer, this study showcases the usefulness of such a simplified model for the control design for the actuation of flagellar magnetic swimmers. This is further emphasized by implementing the optimal actuation in an existing path following algorithm with a stabilizing feedback

loop and observing an improvement in performance compared to the classic sinusoidal actuation.

Chapter 5

Conclusions and Perspectives

5.1 Conclusions

This thesis presents a joint computational and experimental study on the optimal control of flexible magnetic low-Reynolds swimmers. The first contribution of this thesis, described in chapter 2, was the development of a computationally inexpensive dynamic model that describes the movement of a flagellar micro-swimmer in 3D. The Resistive Force Theory based approximation of the hydrodynamics and the discrete shape approximation used for the geometry of the tail of the swimmer led to an ODE model that circumvents the numerical drawbacks of continuum mechanics-based models. Using these approximations led to a model where the dynamics of the swimmer can be seen as an ODE control system that is affine in the components of the actuating magnetic field. Moreover, we showed in chapter 4 that the model can be used to accurately predict the horizontal displacement of an experimental magnetic low-Reynolds swimmer. The model developed in chapter 2 can also be used as a basis for the study of the locomotion of biological flagellated micro-swimmers. In this light, an interesting question that was not addressed in the present work could be the comparison between the optimal deformations of the swimmer, that can be obtained when taking the shape derivatives of the swimmer as a control variable, and the deformations undergone by the swimmer under an optimal magnetic field. The simplified, Resistive Force Theory-based 3D dynamical model was then used in chapter 3 to numerically solve the optimal control problem of maximizing the horizontal displacement of the swimmer in order to investigate different planar and non-planar optimal actuation strategies for magnetic micro-swimmers. The numerical optimal solutions out-perform the commonly used sinusoidal actuation. In particular, the non-planar actuation strategies led to a novel 3D trajectory and are significantly more efficient than the planar ones. Another result stemming from the numerical simulations is the investigation of optimal actuation strategies that do not rely on a static orientating magnetic field, as allowing all the components of the magnetic field to be optimized leads to an increase in swimming speed. The solutions of the optimal control problem with periodicity constraints provide simple magnetic field patterns that can be repeated over time to drive flexible magnetic micro-swimmers, with a propulsion speed significantly greater than the commonly used sinusoidal actuation. One interesting result stemming from these numerical simulations is that the optimal controls are periodic in the planar case, and non-periodic in the 3D case. This raises the question as to whether initial configurations of the swimmer (for example, the initial shape or the initial magnetization angle of

the swimmer) could be found where the 3D optimal solutions are periodic. Answering this question could lead to new designs for flexible micro-swimmers as well as a new 3D optimal magnetic field that is usable in experiments.
Lastly, in chapter 4, the optimal non-planar actuation pattern was tested on an experimental flexible low-Reynolds magnetic swimmer using the ISIR experimental setup. The dynamic model accurately predicts the horizontal displacement of the experimental swimmer under both the optimal and sinusoidal actuation. The simulation and experimental results show that it is necessary to go out of plane in order to maximize the propulsion speed of flexible magnetic low-Reynolds swimmers. We also observed that the solutions that does not rely on an orientating magnetic field (POCP-4)) cannot achieve a straight horizontal propulsion, which is probably due to non-ideal experimental conditions (in particular, the non buoyancy of the swimmer and the low sampling frequency of the magnetic generation system). Future work on this project should include manufacturing of flexible swimmers that are more neutrally buoyant in order to test these solutions experimentally, given that they are the most performant ones in simulation.
The experimental results showcase the usefulness of such a simplified model for computationally inexpensive optimal control design for the actuation of flagellar magnetic swimmers. This is further emphasized by implementing the optimal actuation in an existing path following algorithm and observing an improvement in performance compared to the classic sinusoidal actuation.
In summary, we provided in this thesis a computational framework for the optimal control of flexible magnetic micro-swimmers and showed that it can be used to compute novel magnetic actuations that out-perform the classical actuation method used in the literature for this kind of swimmers in simulations as well as in experiments. By showing that a simplified, RFT-based dynamic model can be used to design optimal controls for magnetic micro-swimmers that are usable in experiments, the present work can be seen as a first step towards efficient model-based motion control and planning for flexible micro-swimmers.

5.2 Perspectives

The work done during this thesis opens up a variety of perspectives on the actuation of magnetic micro-swimmers. Firstly, we present some preliminary numerical results on the optimization of the displacement of a flexible magnetic micro-swimmer near a planar boundary, then we present more general perspectives.

5.2.1 Preliminary simulations on swimming near a planar wall

A crucial challenge for the potential medical applications of micro-robots is their control in the presence of boundaries or in confined environments such as the human vasculature [Ishimoto & Gaffney 2014, Shum & Gaffney 2015, Jang *et al.* 2018]. Controlling micro-swimmers in a confined environment or near a wall is a complex task due to the hydrodynamic attractive effect that boundaries have on micro-swimmers.

In this context, our dynamical model can be adapted in order to model the swimmer in the presence of boundaries, using Boundary-corrected resistive force theory, which is a correction of the RFT coefficients introduced in [Katz 1974], where expressions of the drag coefficients that depend on the distance between the swimmer and the boundaries are proposed in asymptotic regimes far from or near to an infinite no-slip boundary.
A full numerical and experimental study of this problem was not conducted. However, in this section, we present some preliminary simulations where the optimal control problem of maximizing the horizontal displacement of the swimmer in 2D near a planar boundary (assumed to be at $y = 0$) was solved using our model with the corrected drag coefficients of [Katz 1974], which take the following form when assuming that the swimmer is close to a parallel boundary:

$$\begin{cases} k_{\parallel} = \dfrac{2\pi\mu}{\log(\frac{2h}{\varepsilon})}, \\ k_{\perp} = \dfrac{4\pi\mu}{\log(\frac{2h}{\varepsilon}) - 1}, \end{cases} \tag{5.1}$$

where $k_{\parallel}$ is the parallel drag coefficient of the tail, $k_{\perp}$ is the perpendicular drag coefficient of the tail, μ is the viscosity of the fluid, h is the distance of the swimmer to the parallel boundary, and ε is the cross-sectional diameter of the tail of the swimmer. The value of μ was taken equal to the viscosity of pure glycerol : $\mu = 1.524 Pa.s$ and the value of ε is equal to the diameter of the experimental swimmer : $\varepsilon = 0.5mm$. There is no significant additional numerical complexity of the ODE system or the numerical resolution of the optimal control problem when the starting position of the swimmer is at a large enough distance from the wall, however, the direct solver fails to converge to a solution when the initial distance of the swimmer is smaller than $1.5mm$. Figure 5.1 shows the solutions of the optimal control problem (with admissible controls consisting of a fixed static orientating component in the x direction and an actuating component along the y direction) and figure 5.2 shows the associated optimal trajectories.

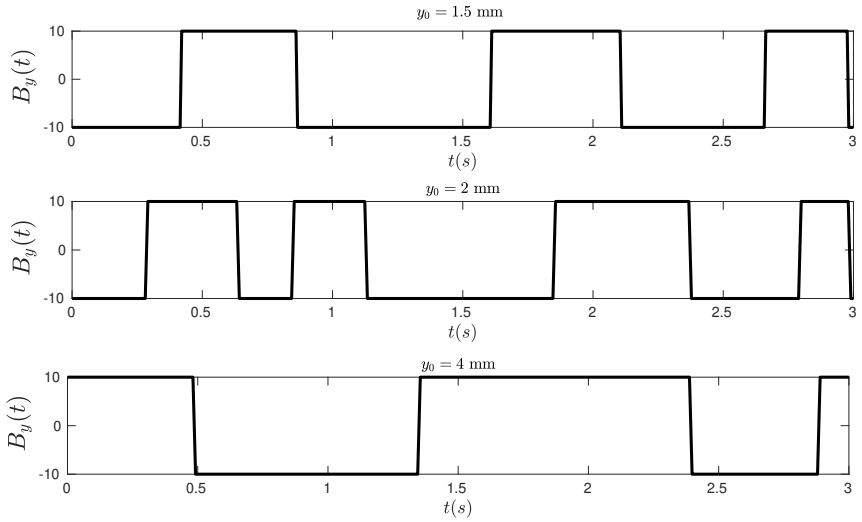

Figure 5.1: Solutions of the optimal control of a magnetic micro-swimmer near a planar boundary (at $y = 0$) for different starting distances from the boundary ($y_0 = 4mm$, $y_0 = 2mm$, and $y_0 = 1.5mm$).

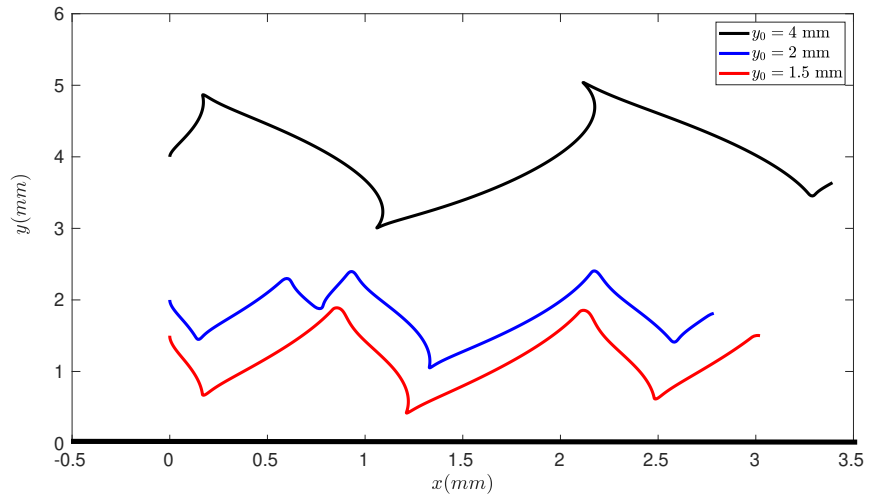

Figure 5.2: Optimal trajectories of magnetic micro-swimmer near a planar boundary (at $y = 0$) for different starting distances from the boundary ($y_0 = 4mm$, $y_0 = 2mm$, and $y_0 = 1.5mm$) .

These results are preliminary as the model was not fitted on experimental data for these simulations, and due to the fact it isn't clear whether the wall-corrected magnetic swimmer model describes reality, although recent studies, such as [Walker *et al.* 2019], found, for self-propelled filaments, that simulations using wall-corrected

Resistive Force Theory are in agreement with simulations using the more accurate, PDE-based Boundary Element Method. However, these simulation results show that it is possible to generate controls to actuate the swimmer near a planar boundary, even if further work is warranted in order to investigate the validity of the model. For this purpose, the experimental setup should be adapted in future work by confining the swimmer in a narrow channel or near a planar boundary and the visual tracking of the swimmer should be improved in order to accurately evaluate the distances between the swimmer and the boundaries in real time to provide sufficient experimental data for the fitting of the model. Studying the problem of optimizing the swimming near a boundary is an important problem due to the potential medical applications for micro-robots, hence, further investigation is warranted based on the model developed during this thesis.

5.2.2 Other Perspectives

Optimal control of flexible swimmers with different elasticities and magnetization profiles

A more controlled manufacturing process of the flexible swimmers should be implemented in order to study the influence of various design parameters on the shape and performance of the optimal actuation. In particular, the elasticity of the tail of swimming micro-robots and the viscosity of the surrounding fluid play a role in the characterization of their optimal deformation patterns and trajectories, as found in the experimental studies of [Huang *et al.* 2019, Spagnolie & Lauga 2010]. This warrants further optimization studies using our framework by constructing swimmers with tails that are of various degrees of compliance to study the effect of the elasticity of the tail on their optimal trajectories and gaits and by optimizing the swimming in different mediums. Another interesting perspective on the design of flexible magnetic swimmers is the optimization of actuation patterns for low-Reynolds swimmers with different magnetization profiles, for example, flexible low Reynolds number swimmers with asymmetric magnetic heads similar to the triangular swimmer of [Manamanchaiyaporn *et al.* 2020], where the non-uniform magnetization of the head changes the way deformations propagate along the tail of the swimmer under an actuating magnetic field.

Optimal actuation of the swimmer using non-homogeneous magnetic fields

Another potential generalization of this work in future studies is the optimal control of magnetic micro-swimmers using non-homogeneous magnetic fields. In this thesis, the focus was on actuation with homogeneous fields, given the 3D Helmholtz coil configuration of the experimental setup. It could be worth looking into optimal actuation patterns beyond this restriction to homogeneous fields, by independently controlling the current passing through each electromagnet, similar to the experimental setups of [Pawashe *et al.* 2009, Khalil *et al.* 2013]. This would significantly

expand the set of admissible controls for the magnetic swimmer, and could lead to novel optimal actuation patterns and trajectories for flexible micro-swimmers that rely on non-trivial magnetic fields instead of homogeneous fields or gradient pulling.

Model-Predictive Control

In section 3.6.4 of Chapter 3, we observed numerically that the planar optimal magnetic fields do not depend on the number of links used in the model. Based on this observation, in practice, a dynamical model of dimension 4 only can be used for the computation of the optimal planar actuation of the swimmer. Similarly, we showed that it is not necessary to go further than a coarse, three-linked approximation of the tail to obtain 3D optimal actuation patterns. This leads to a dimension 8 dynamic system. Given this ability to produce optimal solutions with a numerically cheap approximate dynamical model, an interesting perspective of this work is the development of nonlinear Model Predictive Control algorithms [Cannon 2004] based on the iterative resolution of the maximum speed optimization problem over small horizons in order to optimize the swimming of the flexible robot in real-time. This can be implemented in the ISIR system using the currently implemented visual tracking framework , provided that the sampling frequency of the system is improved as well as the tracking, and that the code for the computations of the dynamics is sufficiently optimized (for example by using optimized BLAS and LAPACK linear algebra libraries for the construction and inversion of the hydrodynamic mass matrix).

Control of multiple micro-swimmers

An important challenge in micro-robotics is the ability to control a "swarm" of multiple micro-robots at once [Chowdhury *et al.* 2015]. There are two main problems that are considered in the literature in this context. The first one is the independent control of multiple swimmers, which is usually achieved by using geometrically or magnetically different swimmers and triggering different swimming behaviours by controlling the frequency and strength of the global actuating magnetic field [Kei Cheang *et al.* 2014]. The second problem is the ability to achieve a collective behaviour of a homogeneous "swarm" of micro-swimmers, which could be an interesting generalization of this present work, as optimal controls to achieve a given formation for a swarm of micro-swimmers could be studied by using our model and adapting previous distributed optimal control studies where multi-agent trajectory optimizations problems were solved numerically such as [Foderaro *et al.* 2014].

Bibliography

[Abbott *et al.* 2009] Jake J Abbott, Kathrin E Peyer, Marco Cosentino Lagomarsino, Li Zhang, Lixin Dong, Ioannis K Kaliakatsos and Bradley J Nelson. *How should microrobots swim?* The international journal of Robotics Research, vol. 28, no. 11-12, pages 1434–1447, 2009. (Cited on pages iii, 5 and 44.)

[Ahmed *et al.* 2016] Daniel Ahmed, Thierry Baasch, Bumjin Jang, Salvador Pane, Jürg Dual and Bradley J. Nelson. *Artificial Swimmers Propelled by Acoustically Activated Flagella.* Nano Letters, 2016. (Cited on page 6.)

[Alouges *et al.* 2009] F Alouges, Antonio DeSimone and A Lefebvre. *Optimal strokes for axisymmetric microswimmers.* The European Physical Journal E, vol. 28, no. 3, pages 279–284, 2009. (Cited on page 15.)

[Alouges *et al.* 2013] F Alouges, A DeSimone, L Giraldi and M Zoppello. *Self-propulsion of slender micro-swimmers by curvature control: N-link swimmers.* International Journal of Non-Linear Mechanics, vol. 56, pages 132–141, 2013. (Cited on pages 20, 23 and 24.)

[Alvarez *et al.* 2014] Luis Alvarez, Benjamin M Friedrich, Gerhard Gompper and U Benjamin Kaupp. *The computational sperm cell.* Trends in cell biology, vol. 24, no. 3, pages 198–207, 2014. (Cited on page 21.)

[Andersson *et al.* 2012] Joel Andersson, Johan Åkesson and Moritz Diehl. *CasADi: A Symbolic Package for Automatic Differentiation andOptimal Control.* In Shaun Forth, Paul Hovland, Eric Phipps, Jean Utke and Andrea Walther, editors, Recent Advances in Algorithmic Differentiation, pages 297–307, Berlin, Heidelberg, 2012. Springer Berlin Heidelberg. (Cited on page 51.)

[Avron *et al.* 2004] JE Avron, O Gat and O Kenneth. *Optimal swimming at low Reynolds numbers.* Physical review letters, vol. 93, no. 18, page 186001, 2004. (Cited on page 15.)

[Becker *et al.* 2003] Leif E Becker, Stephan A Koehler and Howard A Stone. *On self-propulsion of micro-machines at low Reynolds number: Purcell's three-link swimmer.* Journal of fluid mechanics, vol. 490, pages 15–35, 2003. (Cited on page 15.)

[Bellman 1957] Richard Bellman. *Dynamic Programming.* Princeton UniversityPress. BellmanDynamic programming1957, page 151, 1957. (Cited on page 52.)

[Benkoski *et al.* 2010] Jason J Benkoski, Ryan M Deacon, H Bruce Land, Lance M Baird, Jennifer L Breidenich, Rengaswamy Srinivasan, Guy V Clatterbaugh,

Pei Yuin Keng and Jeffrey Pyun. *Dipolar assembly of ferromagnetic nanoparticles into magnetically driven artificial cilia.* Soft Matter, vol. 6, no. 3, pages 602–609, 2010. (Cited on page 7.)

[Betts 1998] John T Betts. *Survey of numerical methods for trajectory optimization.* Journal of guidance, control, and dynamics, vol. 21, no. 2, pages 193–207, 1998. (Cited on page 45.)

[Bonnans *et al.* 2011] JF Bonnans, V Grelard and P Martinon. *Bocop, the optimal control solver, Open source toolbox for optimal control problems.* URL http://bocop. org, 2011. (Cited on page 52.)

[Bonnard & Cots 2014] Bernard Bonnard and Olivier Cots. *Geometric numerical methods and results in the contrast imaging problem in nuclear magnetic resonance.* Mathematical Models and Methods in Applied Sciences, vol. 24, no. 01, pages 187–212, 2014. (Cited on page 50.)

[Brennen & Winet 1977] Christopher Brennen and Howard Winet. *Fluid mechanics of propulsion by cilia and flagella.* Annual Review of Fluid Mechanics, vol. 9, no. 1, pages 339–398, 1977. (Cited on page 3.)

[Brokaw 1965] CJ Brokaw. *Non-sinusoidal bending waves of sperm flagella.* Journal of Experimental Biology, vol. 43, no. 1, pages 155–169, 1965. (Cited on pages 21 and 22.)

[Büskens & Wassel 2013] Christof Büskens and Dennis Wassel. *The ESA NLP Solver WORHP.* In Giorgio Fasano and János D. Pintér, editors, Modeling and Optimization in Space Engineering, volume 73, pages 85–110. Springer New York, 2013. (Cited on page 52.)

[Caillau *et al.* 2010] Jean-Baptiste Caillau, Olivier Cots, Joseph Gergaud and Jean Matthieu Khoury. *HAMPATH: on solving optimal control problems by indirect and path following methods.* In 6th Workshop on Structural Dynamical Systems: Computational Aspects, 2010. (Cited on page 50.)

[Caillau *et al.* 2012] J-B Caillau, Olivier Cots and Joseph Gergaud. *Differential continuation for regular optimal control problems.* Optimization Methods and Software, vol. 27, no. 2, pages 177–196, 2012. (Cited on page 50.)

[Cannon 2004] Mark Cannon. *Efficient nonlinear model predictive control algorithms.* Annual Reviews in Control, vol. 28, no. 2, pages 229–237, 2004. (Cited on page 90.)

[Chattopadhyay *et al.* 2006] Suddhashil Chattopadhyay, Radu Moldovan, Chuck Yeung and X. L. Wu. *Swimming efficiency of bacterium Escherichiacoli.* Proceedings of the National Academy of Sciences, vol. 103, no. 37, pages 13712–13717, 2006. (Cited on page 23.)

[Cheang *et al.* 2017] U Kei Cheang, Hoyeon Kim, Dejan Milutinović, Jongeun Choi and Min Jun Kim. *Feedback Control of an Achiral Robotic Microswimmer*. Journal of Bionic Engineering, vol. 14, no. 2, pages 245–259, 2017. (Cited on pages iii, 9 and 10.)

[Choi *et al.* 2009] Jongho Choi, Hyunchul Choi, Kyoungrae Cha, Jong-Oh Park and Sukho Park. *Two-dimensional locomotive permanent magnet using electromagnetic actuation system with two pairs stationary coils*. In 2009 IEEE International Conference on Robotics and Biomimetics (ROBIO), pages 1166–1171. IEEE, 2009. (Cited on pages iii, 11 and 12.)

[Chowdhury *et al.* 2015] Sagar Chowdhury, Wuming Jing and David J Cappelleri. *Controlling multiple microrobots: recent progress and future challenges*. Journal of Micro-Bio Robotics, vol. 10, no. 1-4, pages 1–11, 2015. (Cited on page 90.)

[Chwang & Wu 1971] AT Chwang and Th Y Wu. *A note on the helical movement of micro-organisms*. Proceedings of the Royal Society of London. Series B. Biological Sciences, vol. 178, no. 1052, pages 327–346, 1971. (Cited on page 61.)

[Chwang & Wu 1975] Allen T Chwang and T Wu. *Hydromechanics of low-Reynolds-number flow. Part 2. Singularity method for Stokes flows*. Journal of Fluid mechanics, vol. 67, no. 4, pages 787–815, 1975. (Cited on page 5.)

[Cox 1970] RG Cox. *The motion of long slender bodies in a viscous fluid Part 1. General theory*. Journal of Fluid mechanics, vol. 44, no. 4, pages 791–810, 1970. (Cited on page 22.)

[Dai *et al.* 2016] Baohu Dai, Jizhuang Wang, Ze Xiong, Xiaojun Zhan, Wei Dai, Chien-Cheng Li, Shien-Ping Feng and Jinyao Tang. *Programmable artificial phototactic microswimmer*. Nature nanotechnology, vol. 11, no. 12, pages 1087–1092, 2016. (Cited on page 6.)

[Diller *et al.* 2013] Eric Diller, Joshua Giltinan and Metin Sitti. *Independent control of multiple magnetic microrobots in three dimensions*. The International Journal of Robotics Research, vol. 32, no. 5, pages 614–631, 2013. (Cited on page 11.)

[Dreyfus *et al.* 2005] Rémi Dreyfus, Jean Baudry, Marcus L Roper, Marc Fermigier, Howard A Stone and Jérôme Bibette. *Microscopic artificial swimmers*. Nature, vol. 437, no. 7060, pages 862–865, 2005. (Cited on pages iii, 6, 7, 8, 13, 15, 16, 24, 43 and 69.)

[Espinosa-Garcia *et al.* 2013] Julian Espinosa-Garcia, Eric Lauga and Roberto Zenit. *Fluid elasticity increases the locomotion of flexible swimmers*. Physics of Fluids, vol. 25, no. 3, page 031701, 2013. (Cited on pages 38 and 73.)

[Falugi *et al.* 2010] Paola Falugi, EC Kerrigan and EV Wyk. *Imperial college london optimal control software (iclocs).* Online: http://www. ee. ic. ac. uk/ICLOCS, 2010. (Cited on pages 52 and 53.)

[Foderaro *et al.* 2014] Greg Foderaro, Silvia Ferrari and Thomas A Wettergren. *Distributed optimal control for multi-agent trajectory optimization.* Automatica, vol. 50, no. 1, pages 149–154, 2014. (Cited on page 90.)

[Friedrich *et al.* 2010] BM Friedrich, IH Riedel-Kruse, J Howard and F Jülicher. *High-precision tracking of sperm swimming fine structure provides strong test of resistive force theory.* Journal of Experimental Biology, vol. 213, no. 8, pages 1226–1234, 2010. (Cited on pages 4, 21 and 22.)

[Frutiger *et al.* 2010] Dominic R Frutiger, Karl Vollmers, Bradley E Kratochvil and Bradley J Nelson. *Small, fast, and under control: wireless resonant magnetic micro-agents.* The International Journal of Robotics Research, vol. 29, no. 5, pages 613–636, 2010. (Cited on pages iii, 9, 10 and 11.)

[Fu *et al.* 2008] Henry C Fu, Charles W Wolgemuth and Thomas R Powers. *Beating patterns of filaments in viscoelastic fluids.* Physical Review E, vol. 78, no. 4, page 041913, 2008. (Cited on page 23.)

[Fujita & Kawai 2001] Tatsuya Fujita and Tatsuo Kawai. *Optimum shape of a flagellated microorganism.* JSME International Journal Series C Mechanical Systems, Machine Elements and Manufacturing, vol. 44, no. 4, pages 952–957, 2001. (Cited on page 15.)

[Fusco *et al.* 2014] Stefano Fusco, Mahmut Selman Sakar, Stephen Kennedy, Christian Peters, Rocco Bottani, Fabian Starsich, Angelo Mao, Georgios A Sotiriou, Salvador Pané, Sotiris E Pratsinis*et al.* *An integrated microrobotic platform for on-demand, targeted therapeutic interventions.* Advanced Materials, vol. 26, no. 6, pages 952–957, 2014. (Cited on page 6.)

[Gadêlha *et al.* 2010] H Gadêlha, EA Gaffney, DJ Smith and JC Kirkman-Brown. *Nonlinear instability in flagellar dynamics: a novel modulation mechanism in sperm migration?* Journal of the Royal Society Interface, vol. 7, no. 53, pages 1689–1697, 2010. (Cited on page 23.)

[Gadêlha 2013] Hermes Gadêlha. *On the optimal shape of magnetic swimmers.* Regular and Chaotic Dynamics, vol. 18, no. 1-2, pages 75–84, 2013. (Cited on pages 16 and 23.)

[Gao *et al.* 2010a] Wei Gao, Sirilak Sattayasamitsathit, Kalayil Manian Manesh, Daniel Weihs and Joseph Wang. *Magnetically powered flexible metal nanowire motors.* Journal of the American Chemical Society, vol. 132, no. 41, pages 14403–14405, 2010. (Cited on page 13.)

[Gao *et al.* 2010b] Wei Gao, Sirilak Sattayasamitsathit, Kalayil Manian Manesh, Daniel Weihs and Joseph Wang. *Magnetically powered flexible metal nanowire motors.* Journal of the American Chemical Society, vol. 132, no. 41, pages 14403–14405, 2010. (Cited on page 44.)

[Gazzola *et al.* 2018] M Gazzola, LH Dudte, AG McCormick and L Mahadevan. *Forward and inverse problems in the mechanics of soft filaments.* Royal Society open science, vol. 5, no. 6, page 171628, 2018. (Cited on page 23.)

[Ghosh & Fischer 2009] Ambarish Ghosh and Peer Fischer. *Controlled propulsion of artificial magnetic nanostructured propellers.* Nano letters, vol. 9, no. 6, pages 2243–2245, 2009. (Cited on pages iii, 8, 9 and 13.)

[Giuliani *et al.* 2018] Nicola Giuliani, Luca Heltai and Antonio DeSimone. *Predicting and optimizing microswimmer performance from the hydrodynamics of its components: The relevance of interactions.* Soft robotics, vol. 5, no. 4, pages 410–424, 2018. (Cited on page 23.)

[Gray & Hancock 1955] James Gray and GJ Hancock. *The propulsion of sea-urchin spermatozoa.* Journal of Experimental Biology, vol. 32, no. 4, pages 802–814, 1955. (Cited on pages 6, 16, 20, 21 and 22.)

[Guix *et al.* 2013] M Guix, J Orozco, M García, W Gao, S Sattayasamitsathit, A Merkoçi and A Escarpa. *ACS Nano, 2012, 6, 4445–4451 CrossRef CAS PubMed;(b) W. Gao, X. Feng, A. Pei, Y. Gu, J. Li and J. Wang.* Nanoscale, vol. 5, pages 4696–4700, 2013. (Cited on page 69.)

[Hancock 1953] GJ Hancock. *The self-propulsion of microscopic organisms through liquids.* Proceedings of the Royal Society of London. Series A. Mathematical and Physical Sciences, vol. 217, no. 1128, pages 96–121, 1953. (Cited on pages 5, 20 and 21.)

[Hascoet & Pascual 2013] Laurent Hascoet and Valérie Pascual. *The Tapenade automatic differentiation tool: Principles, model, and specification.* ACM Transactions on Mathematical Software (TOMS), vol. 39, no. 3, pages 1–43, 2013. (Cited on page 51.)

[Higdon 1979a] JJL Higdon. *The generation of feeding currents by flagellar motions.* Journal of Fluid Mechanics, vol. 94, no. 2, pages 305–330, 1979. (Cited on page 15.)

[Higdon 1979b] JJL Higdon. *A hydrodynamic analysis of flagellar propulsion.* Journal of Fluid Mechanics, vol. 90, no. 4, pages 685–711, 1979. (Cited on page 15.)

[Higdon 1979c] JJL Higdon. *The hydrodynamics of flagellar propulsion: helical waves.* Journal of Fluid Mechanics, vol. 94, no. 2, pages 331–351, 1979. (Cited on page 15.)

[Hu *et al.* 2006] Chao Hu, Max Q-H Meng and Mrinal Mandal. *The calibration of 3-axis magnetic sensor array system for tracking wireless capsule endoscope.* In 2006 IEEE/RSJ International Conference on Intelligent Robots and Systems, pages 162–167. IEEE, 2006. (Cited on page 12.)

[Huang *et al.* 2014] Tian-Yun Huang, Famin Qiu, Hsi-Wen Tung, Xue-Bo Chen, Bradley J Nelson and Mahmut Selman Sakar. *Generating mobile fluidic traps for selective three-dimensional transport of microobjects.* Applied Physics Letters, vol. 105, no. 11, page 114102, 2014. (Cited on page 11.)

[Huang *et al.* 2019] H-W Huang, Fazil Emre Uslu, Panayiota Katsamba, Eric Lauga, Mahmut S Sakar and Bradley J Nelson. *Adaptive locomotion of artificial microswimmers.* Science advances, vol. 5, no. 1, page eaau1532, 2019. (Cited on page 89.)

[Hwang *et al.* 2010] Gilgueng Hwang, D Sinan Haliyo and Stéphane Régnier. *Remotely Powered Propulsion of Helical Nanobelts.* In Robotics: Science and Systems, 2010. (Cited on pages iii, 8 and 9.)

[Ishimoto & Gaffney 2014] Kenta Ishimoto and Eamonn A. Gaffney. *A study of spermatozoan swimming stability near a surface.* Journal of Theoretical Biology, vol. 360, pages 187 – 199, 2014. (Cited on pages 82 and 86.)

[Jang *et al.* 2015] Bumjin Jang, Emiliya Gutman, Nicolai Stucki, Benedikt F Seitz, Pedro D Wendel-García, Taylor Newton, Juho Pokki, Olgaç Ergeneman, Salvador Pané, Yizhar Or*et al.* *Undulatory locomotion of magnetic multilink nanoswimmers.* Nano letters, vol. 15, no. 7, pages 4829–4833, 2015. (Cited on pages iii, 7, 8, 44, 69 and 81.)

[Jang *et al.* 2018] Bumjin Jang, Amanda Aho, Bradley J Nelson and Salvador Pane. *Fabrication and Locomotion of Flexible Nanoswimmers.* IEEE/RSJ International Conference on Intelligent robots and systems (IROS), IEEE, Madrid 2018. (Cited on pages 82 and 86.)

[Jeong *et al.* 2011] Semi Jeong, Hyunchul Choi, Kyoungrae Cha, Jie Li, Jong-oh Park and Sukho Park. *Enhanced locomotive and drilling microrobot using precessional and gradient magnetic field.* Sensors and Actuators A: Physical, vol. 171, no. 2, pages 429–435, 2011. (Cited on pages 11 and 14.)

[Jikeli *et al.* 2015] Jan F Jikeli, Luis Alvarez, Benjamin M Friedrich, Laurence G Wilson, René Pascal, Remy Colin, Magdalena Pichlo, Andreas Rennhack, Christoph Brenker and U Benjamin Kaupp. *Sperm navigation along helical paths in 3D chemoattractant landscapes.* Nature communications, vol. 6, page 7985, 2015. (Cited on pages iii, 20, 35, 36, 37 and 77.)

[Kaspers 2011] Anne Kaspers. Blob detection. Master's thesis, Image Sciences Institute UMC, Utrecht, 2011. (Cited on page 71.)

[Katz 1974] David F Katz. *On the propulsion of micro-organisms near solid boundaries.* Journal of Fluid Mechanics, vol. 64, no. 1, pages 33–49, 1974. (Cited on pages 82 and 87.)

[Keaveny & Shelley 2011] Eric E Keaveny and Michael J Shelley. *Applying a second-kind boundary integral equation for surface tractions in Stokes flow.* Journal of Computational Physics, vol. 230, no. 5, pages 2141–2159, 2011. (Cited on page 16.)

[Kei Cheang *et al.* 2014] U Kei Cheang, Kyoungwoo Lee, Anak Agung Julius and Min Jun Kim. *Multiple-robot drug delivery strategy through coordinated teams of microswimmers.* Applied physics letters, vol. 105, no. 8, page 083705, 2014. (Cited on page 90.)

[Keller 1976] Herbert B Keller. Numerical solution of two point boundary value problems. SIAM, 1976. (Cited on page 49.)

[Khalil *et al.* 2013] Islam SM Khalil, Marc P Pichel, Leon Abelmann and Sarthak Misra. *Closed-loop control of magnetotactic bacteria.* The International Journal of Robotics Research, vol. 32, no. 6, pages 637–649, 2013. (Cited on page 89.)

[Khalil *et al.* 2014] Islam SM Khalil, Herman C Dijkslag, Leon Abelmann and Sarthak Misra. *MagnetoSperm: A microrobot that navigates using weak magnetic fields.* Applied Physics Letters, vol. 104, no. 22, page 223701, 2014. (Cited on pages iii, 6, 7, 8, 13, 38, 44, 73 and 81.)

[Khalil *et al.* 2016] Islam SM Khalil, Ahmet Fatih Tabak, Anke Klingner and Metin Sitti. *Magnetic propulsion of robotic sperms at low-Reynolds number.* Applied Physics Letters, vol. 109, no. 3, page 033701, 2016. (Cited on pages iii, 8 and 13.)

[Khalil *et al.* 2018] Islam SM Khalil, Ahmet Fatih Tabak, Mohamed Abou Seif, Anke Klingner and Metin Sitti. *Controllable switching between planar and helical flagellar swimming of a soft robotic sperm.* PloS one, vol. 13, no. 11, page e0206456, 2018. (Cited on page 61.)

[Kim *et al.* 2016] Sangwon Kim, Seungmin Lee, Jeonghun Lee, Bradley J Nelson, Li Zhang and Hongsoo Choi. *Fabrication and Manipulation of Ciliary Microrobots with Non-reciprocal Magnetic Actuation.* Scientific reports, vol. 6, page 30713, 2016. (Cited on pages iii, 9 and 10.)

[Ko *et al.* 2012] Youngho Ko, Sungyoung Na, Youngwoo Lee, Kyoungrae Cha, Seong Young Ko, Jongoh Park and Sukho Park. *A jellyfish-like swimming mini-robot actuated by an electromagnetic actuation system.* Smart Materials and Structures, vol. 21, no. 5, page 057001, 2012. (Cited on pages iii, 9, 10 and 11.)

[Kósa *et al.* 2012] Gábor Kósa, Péter Jakab, Gábor Székely and Nobuhiko Hata. *MRI driven magnetic microswimmers.* Biomedical microdevices, vol. 14, no. 1, pages 165–178, 2012. (Cited on page 12.)

[Kraft 1985] Dieter Kraft. *On converting optimal control problems into nonlinear programming problems.* In Computational mathematical programming, pages 261–280. Springer, 1985. (Cited on page 49.)

[Kummer *et al.* 2010a] Michael P Kummer, Jake J Abbott, Bradley E Kratochvil, Ruedi Borer, Ali Sengul and Bradley J Nelson. *OctoMag: An electromagnetic system for 5-DOF wireless micromanipulation.* IEEE Transactions on Robotics, vol. 26, no. 6, pages 1006–1017, 2010. (Cited on pages iii, 11 and 12.)

[Kummer *et al.* 2010b] Michael P Kummer, Jake J Abbott, Bradley E Kratochvil, Ruedi Borer, Ali Sengul and Bradley J Nelson. *OctoMag: An electromagnetic system for 5-DOF wireless micromanipulation.* IEEE Transactions on Robotics, vol. 26, no. 6, pages 1006–1017, 2010. (Cited on page 14.)

[Lauga & Powers 2009] Eric Lauga and Thomas R Powers. *The hydrodynamics of swimming microorganisms.* Reports on Progress in Physics, vol. 72, no. 9, page 096601, 2009. (Cited on page 3.)

[Lauga 2007] Eric Lauga. *Floppy swimming: Viscous locomotion of actuated elastica.* Physical Review E, vol. 75, no. 4, page 041916, 2007. (Cited on page 23.)

[Lighthill 1975] Sir James Lighthill. Mathematical biofluiddynamics. SIAM, 1975. (Cited on pages 14 and 15.)

[Lighthill 1976] James Lighthill. *Flagellar hydrodynamics.* SIAM review, vol. 18, no. 2, pages 161–230, 1976. (Cited on page 22.)

[Lohéac & Munnier 2014] Jérôme Lohéac and Alexandre Munnier. *Controllability of 3D low Reynolds number swimmers.* ESAIM: Control, Optimisation and Calculus of Variations, vol. 20, no. 1, pages 236–268, 2014. (Cited on page 3.)

[Lowe 2003] Christopher P Lowe. *Dynamics of filaments: modelling the dynamics of driven microfilaments.* Philosophical Transactions of the Royal Society of London B: Biological Sciences, vol. 358, no. 1437, pages 1543–1550, 2003. (Cited on pages 23 and 24.)

[Mack 2001] Michael J Mack. *Minimally invasive and robotic surgery.* Jama, vol. 285, no. 5, pages 568–572, 2001. (Cited on page 6.)

[Mahoney *et al.* 2011a] Arthur W Mahoney, John C Sarrazin, Eberhard Bamberg and Jake J Abbott. *Velocity control with gravity compensation for magnetic helical microswimmers.* Advanced Robotics, vol. 25, no. 8, pages 1007–1028, 2011. (Cited on pages 8 and 13.)

[Mahoney *et al.* 2011b] Arthur W Mahoney, John C Sarrazin, Eberhard Bamberg and Jake J Abbott. *Velocity control with gravity compensation for magnetic helical microswimmers.* Advanced Robotics, vol. 25, no. 8, pages 1007–1028, 2011. (Cited on pages 11, 13 and 14.)

[Manamanchaiyaporn *et al.* 2020] Laliphat Manamanchaiyaporn, XU Tiantian*et al.* *Magnetic soft robot with the triangular head-tail morphology inspired by lateral undulation.* IEEE/ASME Transactions on Mechatronics, 2020. (Cited on page 89.)

[Marchand *et al.* 2005] Éric Marchand, Fabien Spindler and François Chaumette. *ViSP for visual servoing: a generic software platform with a wide class of robot control skills.* IEEE Robotics & Automation Magazine, vol. 12, no. 4, pages 40–52, 2005. (Cited on page 71.)

[Mathieu *et al.* 2006] J-B Mathieu, Gilles Beaudoin and Sylvain Martel. *Method of propulsion of a ferromagnetic core in the cardiovascular system through magnetic gradients generated by an MRI system.* IEEE Transactions on Biomedical Engineering, vol. 53, no. 2, pages 292–299, 2006. (Cited on pages iii, 11 and 12.)

[McCord *et al.* 2005] Rachel Patton McCord, John N Yukich and Karen K Bernd. *Analysis of force generation during flagellar assembly through optical trapping of free-swimming Chlamydomonas reinhardtii.* Cell motility and the cytoskeleton, vol. 61, no. 3, pages 137–144, 2005. (Cited on page 23.)

[Michalewicz *et al.* 1990] Z. Michalewicz, J. B. Krawczyk, M. Kazemi and C. Z. Janikow. *Genetic algorithms and optimal control problems.* In 29th IEEE Conference on Decision and Control, pages 1664–1666 vol.3, 1990. (Cited on page 52.)

[Mitchison & Mitchison 2010] TJ Mitchison and HM Mitchison. *Cell biology: how cilia beat.* Nature, vol. 463, no. 7279, page 308, 2010. (Cited on page 4.)

[Moreau *et al.* 2018] Clement Moreau, Laetitia Giraldi and Hermes Augusto Buarque Gadelha. *The asymptotic coarse-graining formulation of slender-rods, bio-filaments and flagella.* Journal of the Royal Society Interface, 2018. (Cited on pages 20, 23 and 24.)

[Muller *et al.* 2000] UK Muller, EJ Stamhuis and JJ Videler. *Hydrodynamics of unsteady fish swimming and the effects of body size: comparing the flow fields of fish larvae and adults.* Journal of Experimental Biology, vol. 203, no. 2, pages 193–206, 2000. (Cited on page 3.)

[Najafi & Golestanian 2004] Ali Najafi and Ramin Golestanian. *Simple swimmer at low Reynolds number: Three linked spheres.* Physical Review E, vol. 69, no. 6, page 062901, 2004. (Cited on page 15.)

[Oulmas *et al.* 2016] Ali Oulmas, Nicolas Andreff and Stéphane Régnier. *Closed-loop 3D path following of scaled-up helical microswimmers.* In Robotics and Automation (ICRA), 2016 IEEE International Conference on, pages 1725–1730. IEEE, 2016. (Cited on page 14.)

[Oulmas *et al.* 2017] Ali Oulmas, Nicolas Andreff and Stéphane Régnier. *3D closed-loop motion control of swimmer with flexible flagella at low Reynolds numbers.* In 2017 IEEE/RSJ International Conference on Intelligent Robots and Systems (IROS), pages 1877–1882. IEEE, 2017. (Cited on pages iv, v, 39, 40, 68, 71, 72 and 80.)

[Oulmas 2018] Ali Oulmas. *Suivi de chemin 3D de nageurs magnétiques à faible nombre de Reynolds.* PhD thesis, Université Pierre et Marie Curie-Paris VI, 2018. Thèse de doctorat dirigée par Regnier, Stephane et Andreff, Nicolas Robotique Sorbonne université 2018. (Cited on pages 17 and 70.)

[Pak *et al.* 2011] On Shun Pak, Wei Gao, Joseph Wang and Eric Lauga. *High-speed propulsion of flexible nanowire motors: Theory and experiments.* Soft Matter, vol. 7, no. 18, pages 8169–8181, 2011. (Cited on page 7.)

[Patra *et al.* 2013] Debabrata Patra, Samudra Sengupta, Wentao Duan, Hua Zhang, Ryan Pavlick and Ayusman Sen. *Intelligent, self-powered, drug delivery systems.* Nanoscale, vol. 5, no. 4, pages 1273–1283, 2013. (Cited on page 6.)

[Pawashe *et al.* 2009] Chytra Pawashe, Steven Floyd and Metin Sitti. *Modeling and experimental characterization of an untethered magnetic micro-robot.* The International Journal of Robotics Research, vol. 28, no. 8, pages 1077–1094, 2009. (Cited on page 89.)

[Pawashe *et al.* 2011] Chytra Pawashe, Steven Floyd, Eric Diller and Metin Sitti. *Two-dimensional autonomous microparticle manipulation strategies for magnetic microrobots in fluidic environments.* IEEE Transactions on Robotics, vol. 28, no. 2, pages 467–477, 2011. (Cited on page 14.)

[Pironneau & Katz 1974] O Pironneau and DF Katz. *Optimal swimming of flagellated micro-organisms.* Journal of Fluid Mechanics, vol. 66, no. 2, pages 391–415, 1974. (Cited on page 15.)

[Plouraboué *et al.* 2017] Franck Plouraboué, E Ibrahima Thiam, Blaise Delmotte and Eric Climent. *Identification of internal properties of fibres and micro-swimmers.* Proceedings of the Royal Society A: Mathematical, Physical and Engineering Sciences, vol. 473, no. 2197, page 20160517, 2017. (Cited on page 23.)

[Pouponneau *et al.* 2014] Pierre Pouponneau, Gilles Soulez, Gilles Beaudoin, Jean-Christophe Leroux and Sylvain Martel. *MR imaging of therapeutic magnetic microcarriers guided by magnetic resonance navigation for targeted*

liver chemoembolization. Cardiovascular and interventional radiology, vol. 37, no. 3, pages 784–790, 2014. (Cited on page 12.)

[Powers 2002] Thomas R Powers. *Role of body rotation in bacterial flagellar bundling.* Physical Review E, vol. 65, no. 4, page 040903, 2002. (Cited on page 4.)

[Pozrikidis & Jankowski 1997] Constantine Pozrikidis and D Jankowski. Introduction to theoretical and computational fluid dynamics, volume 675. Oxford university press New York, 1997. (Cited on pages 2 and 3.)

[Pozrikidis *et al.* 1992] Constantine Pozrikidis*et al.* Boundary integral and singularity methods for linearized viscous flow. Cambridge University Press, 1992. (Cited on pages 6 and 16.)

[Proudman & Pearson 1957] Ian Proudman and JRA Pearson. *Expansions at small Reynolds numbers for the flow past a sphere and a circular cylinder.* Journal of Fluid Mechanics, vol. 2, no. 3, pages 237–262, 1957. (Cited on page 3.)

[Purcell 1977] Edward M Purcell. *Life at low Reynolds number.* American journal of physics, vol. 45, no. 1, pages 3–11, 1977. (Cited on pages 4 and 15.)

[Qiu *et al.* 2015] Famin Qiu, Satoshi Fujita, Rami Mhanna, Li Zhang, Benjamin R Simona and Bradley J Nelson. *Magnetic helical microswimmers functionalized with lipoplexes for targeted gene delivery.* Advanced Functional Materials, vol. 25, no. 11, pages 1666–1671, 2015. (Cited on pages 6 and 13.)

[Ramia *et al.* 1993] M Ramia, DL Tullock and N Phan-Thien. *The role of hydrodynamic interaction in the locomotion of microorganisms.* Biophysical journal, vol. 65, no. 2, pages 755–778, 1993. (Cited on page 6.)

[Rao *et al.* 2010] Anil V Rao, David A Benson, Christopher Darby, Michael A Patterson, Camila Francolin, Ilyssa Sanders and Geoffrey T Huntington. *Algorithm 902: Gpops, a matlab software for solving multiple-phase optimal control problems using the gauss pseudospectral method.* ACM Transactions on Mathematical Software (TOMS), vol. 37, no. 2, pages 1–39, 2010. (Cited on page 52.)

[Rao 2009] Anil V Rao. *A survey of numerical methods for optimal control.* Advances in the Astronautical Sciences, vol. 135, no. 1, pages 497–528, 2009. (Cited on page 45.)

[Rodenborn *et al.* 2013] Bruce Rodenborn, Chih-Hung Chen, Harry L Swinney, Bin Liu and HP Zhang. *Propulsion of microorganisms by a helical flagellum.* Proceedings of the National Academy of Sciences, vol. 110, no. 5, pages E338–E347, 2013. (Cited on page 5.)

[Roper *et al.* 2008] Marcus Roper, Rémi Dreyfus, Jean Baudry, Marc Fermigier, Jérôme Bibette and Howard A Stone. *Do magnetic micro-swimmers move like eukaryotic cells?* Proceedings of the Royal Society A: Mathematical, Physical and Engineering Sciences, vol. 464, no. 2092, pages 877–904, 2008. (Cited on pages 16 and 23.)

[Rorai *et al.* 2019] C Rorai, M Zaitsev and S Karabasov. *On the limitations of some popular numerical models of flagellated microswimmers: importance of long-range forces and flagellum waveform.* Royal Society open science, vol. 6, no. 1, page 180745, 2019. (Cited on page 23.)

[Ross & Fahroo 2001] I. M. Ross and F. Fahroo. *Convergence of pseudospectral discretizations of optimal control problems.* In Proceedings of the 40th IEEE Conference on Decision and Control (Cat. No.01CH37228), volume 4, pages 3175–3177 vol.4, 2001. (Cited on page 52.)

[Ross 2005] I Michael Ross. *A historical introduction to the covector mapping principle.* In Proceedings of Astrodynamics Specialists Conference. Citeseer, 2005. (Cited on page 52.)

[Samson 1995] Claude Samson. *Control of chained systems application to path following and time-varying point-stabilization of mobile robots.* IEEE transactions on Automatic Control, vol. 40, no. 1, pages 64–77, 1995. (Cited on page 72.)

[Schamel *et al.* 2014] Debora Schamel, Andrew G Mark, John G Gibbs, Cornelia Miksch, Konstantin I Morozov, Alexander M Leshansky and Peer Fischer. *Nanopropellers and their actuation in complex viscoelastic media.* ACS nano, vol. 8, no. 9, pages 8794–8801, 2014. (Cited on page 9.)

[Schättler & Ledzewicz 2012] Heinz Schättler and Urszula Ledzewicz. Geometric optimal control: theory, methods and examples, volume 38. Springer Science & Business Media, 2012. (Cited on page 45.)

[Schuerle *et al.* 2012] Simone Schuerle, Salvador Pané, Eva Pellicer, Jordi Sort, Maria D Baró and Bradley J Nelson. *Helical and tubular lipid microstructures that are electroless-coated with CoNiReP for wireless magnetic manipulation.* Small, vol. 8, no. 10, pages 1498–1502, 2012. (Cited on page 9.)

[Schulman *et al.* 2014] Rafael D Schulman, Matilda Backholm, William S Ryu and Kari Dalnoki-Veress. *Dynamic force patterns of an undulatory microswimmer.* Physical Review E, vol. 89, no. 5, page 050701, 2014. (Cited on page 22.)

[Shampine & Reichelt 1997] Lawrence F Shampine and Mark W Reichelt. *The matlab ode suite.* SIAM journal on scientific computing, vol. 18, no. 1, pages 1–22, 1997. (Cited on page 34.)

[Shampine *et al.* 2000] Lawrence F Shampine, Jacek Kierzenka, Mark W Reichelt*et al. Solving boundary value problems for ordinary differential equations in MATLAB with bvp4c*. Tutorial notes, vol. 2000, pages 1–27, 2000. (Cited on page 51.)

[Shapere & Wilczek 1989] Alfred Shapere and Frank Wilczek. *Efficiencies of self-propulsion at low Reynolds number*. Journal of fluid mechanics, vol. 198, pages 587–599, 1989. (Cited on page 15.)

[Shum & Gaffney 2015] Henry Shum and Eamonn A. Gaffney. *Hydrodynamic analysis of flagellated bacteria swimming in corners of rectangular channels*. Phys. Rev. E, vol. 92, 2015. (Cited on pages 82 and 86.)

[Spagnolie & Lauga 2010] Saverio E Spagnolie and Eric Lauga. *The optimal elastic flagellum*. Physics of Fluids, vol. 22, no. 3, page 455, 2010. (Cited on pages 15, 23 and 89.)

[Spagnolie & Lauga 2011] Saverio E Spagnolie and Eric Lauga. *Comparative hydrodynamics of bacterial polymorphism*. Physical Review Letters, vol. 106, no. 5, page 058103, 2011. (Cited on page 23.)

[Stanton *et al.* 2015] MM Stanton, C Trichet-Paredes and Samuel Sanchez. *Applications of three-dimensional (3D) printing for microswimmers and bio-hybrid robotics*. Lab on a Chip, vol. 15, no. 7, pages 1634–1637, 2015. (Cited on page 70.)

[Tabak & Yesilyurt 2014] Ahmet Fatih Tabak and Serhat Yesilyurt. *Computationally-validated surrogate models for optimal geometric design of bio-inspired swimming robots: Helical swimmers*. Computers & Fluids, vol. 99, pages 190–198, 2014. (Cited on page 6.)

[Tam & Hosoi 2007] Daniel Tam and Annete E Hosoi. *Optimal stroke patterns for Purcell's three-link swimmer*. Physical Review Letters, vol. 98, no. 6, page 068105, 2007. (Cited on pages 15 and 64.)

[Tam 2008] Daniel See Wai Tam. *Motion at low Reynolds number*. PhD thesis, Massachusetts Institute of Technology, 2008. (Cited on page 15.)

[Tornberg & Shelley 2004] Anna-Karin Tornberg and Michael J Shelley. *Simulating the dynamics and interactions of flexible fibers in Stokes flows*. Journal of Computational Physics, vol. 196, no. 1, pages 8–40, 2004. (Cited on page 23.)

[Tottori *et al.* 2012] Soichiro Tottori, Li Zhang, Famin Qiu, Krzysztof K Krawczyk, Alfredo Franco-Obregón and Bradley J Nelson. *Magnetic helical micromachines: fabrication, controlled swimming, and cargo transport*. Advanced materials, vol. 24, no. 6, pages 811–816, 2012. (Cited on pages iii, 9 and 13.)

[Vach *et al.* 2013] Peter J Vach, Nicolas Brun, Mathieu Bennet, Luca Bertinetti, Marc Widdrat, Jens Baumgartner, Stefan Klumpp, Peter Fratzl and Damien Faivre. *Selecting for function: solution synthesis of magnetic nanopropellers.* Nano letters, vol. 13, no. 11, pages 5373–5378, 2013. (Cited on page 10.)

[Vach *et al.* 2015] Peter J Vach, Peter Fratzl, Stefan Klumpp and Damien Faivre. *Fast magnetic micropropellers with random shapes.* Nano letters, vol. 15, no. 10, pages 7064–7070, 2015. (Cited on page 10.)

[Wächter & Biegler 2006] Andreas Wächter and Lorenz T Biegler. *On the implementation of an interior-point filter line-search algorithm for large-scale nonlinear programming.* Mathematical programming, vol. 106, no. 1, pages 25–57, 2006. (Cited on pages 52 and 53.)

[Walker & Keaveny 2013] Shawn W Walker and Eric E Keaveny. *Analysis of shape optimization for magnetic microswimmers.* SIAM Journal on Control and Optimization, vol. 51, no. 4, pages 3093–3126, 2013. (Cited on page 16.)

[Walker *et al.* 2019] Benjamin J Walker, Kenta Ishimoto, Hermes Gadêlha and Eamonn A Gaffney. *Filament mechanics in a half-space via regularised Stokeslet segments.* Journal of Fluid Mechanics, vol. 879, pages 808–833, 2019. (Cited on page 88.)

[Wang 2009] Xuezhong Wang. *Solving optimal control problems with MATLAB: Indirect methods.* ISE Dept., NCSU, Raleigh, NC, vol. 27695, 2009. (Cited on page 51.)

[Wiggins *et al.* 1998] Chris H Wiggins, D Riveline, Albrecht Ott and Raymond E Goldstein. *Trapping and wiggling: elastohydrodynamics of driven microfilaments.* Biophysical journal, vol. 74, no. 2, pages 1043–1060, 1998. (Cited on page 23.)

[Xu *et al.* 2005] Xiao-Chen Xu, Chang-Hong Hu, Lei Sun, Jesse Yen and K Kirk Shung. *High-frequency high frame rate ultrasound imaging system for small animal imaging with linear arrays.* In IEEE Ultrasonics Symposium, 2005., volume 3, pages 1431–1434. IEEE, 2005. (Cited on page 13.)

[Xu 2014] Tiantian Xu. *Propulsion characteristics and visual servo control of scaled-up helical microswimmers.* PhD thesis, Université Pierre et Marie Curie-Paris VI, 2014. (Cited on pages iii, 11, 12, 14, 17, 70 and 71.)

[Ye *et al.* 2014] Zhou Ye, Stéphane Régnier and Metin Sitti. *Rotating magnetic miniature swimming robots with multiple flexible flagella.* IEEE Transactions on Robotics, vol. 30, no. 1, pages 3–13, 2014. (Cited on page 9.)

[Yesin *et al.* 2006] K Berk Yesin, Karl Vollmers and Bradley J Nelson. *Modeling and control of untethered biomicrorobots in a fluidic environment using electromagnetic fields.* The International Journal of Robotics Research, vol. 25, no. 5-6, pages 527–536, 2006. (Cited on pages 11 and 13.)

[Yu *et al.* 2006] Tony S Yu, Eric Lauga and AE Hosoi. *Experimental investigations of elastic tail propulsion at low Reynolds number*. Physics of Fluids, vol. 18, no. 9, page 091701, 2006. (Cited on pages 38 and 73.)

[Zarei & Zarei 2018] Mohammad Zarei and Mohanna Zarei. *Self-Propelled Micro/Nanomotors for Sensing and Environmental Remediation*. Small, vol. 14, no. 30, page 1800912, 2018. (Cited on page 69.)

[Zeeshan *et al.* 2014] Muhammad A Zeeshan, Roman Grisch, Eva Pellicer, Kartik M Sivaraman, Kathrin E Peyer, Jordi Sort, Berna Özkale, Mahmut S Sakar, Bradley J Nelson and Salvador Pané. *Hybrid helical magnetic microrobots obtained by 3D template-assisted electrodeposition*. Small, vol. 10, no. 7, pages 1284–1288, 2014. (Cited on page 9.)

[Zhang *et al.* 2009] Li Zhang, Jake J Abbott, Lixin Dong, Bradley E Kratochvil, Dominik Bell and Bradley J Nelson. *Artificial bacterial flagella: Fabrication and magnetic control*. Applied Physics Letters, vol. 94, no. 6, page 064107, 2009. (Cited on pages iii, 8, 9, 11 and 13.)

[Zhang *et al.* 2012] Li Zhang, Tristan Petit, Kathrin E Peyer and Bradley J Nelson. *Targeted cargo delivery using a rotating nickel nanowire*. Nanomedicine: Nanotechnology, Biology and Medicine, vol. 8, no. 7, pages 1074–1080, 2012. (Cited on page 69.)